

Dissertation
submitted to the
Combined Faculties of the Natural Sciences and Mathematics
of the Ruperto-Carola University of Heidelberg, Germany
for the degree of
Doctor of Natural Sciences

Put forward by
Simon Robert Müller
born in Ulm, Germany

Oral examination on the 4 February 2020

From Classical Xenon Fringes to Hydrogen Interferometry

Referees: Prof. Dr. Markus K. Oberthaler
Prof. Dr. Thomas Gasenzer

Abstract:

The wave description of particles is a cornerstone of quantum physics and lies in the focus of multiple modern experiments. The present work demonstrates the working principle of a Talbot-Lau interferometer with a wide range of particles, namely hydrogen, helium, argon, krypton, and xenon. Such an interferometer consists of three gratings and is herein extensively studied in respect of the most important factors which affect the quality of the interference pattern. Special focus is given to the gratings' alignment requirements and to the intra-grating interactions which occur between the particles and the material gratings. The experimental design which has been realised in the scope of this work is discussed in detail and tested with numerous characterisation measurements. These act as a preliminary stage to the working interferometer and provide various information, such as about the composition of the particle beam, the uniformity of the grating pitches, or the detection precision and data acquisition of the fringe pattern. The constructed interferometer successfully operates with particles whose de Broglie wavelengths span more than two orders of magnitude, i.e. $\lambda_{dB} \in [0.02 \text{ pm}, 2.2 \text{ pm}]$, and thus enables the observation of the transition to the classical equivalent of the Talbot-Lau interferometer, the moiré deflectometer. The shape of the interference pattern gives an insight into the intra-grating interactions, which are modelled by means of implanted charges inside the material gratings. Furthermore, a novel idea of using the Talbot-Lau interferometer as a spectrometer is demonstrated. To explore the wave nature also of ions, the work concludes with a discussion on the necessary conditions for, and the experimental implementation of a functioning Talbot-Lau interferometer with protons.

Zusammenfassung:

Der Wellencharakter von Teilchen ist ein Eckpfeiler der Quantenmechanik und steht im Mittelpunkt einer Vielzahl von zeitgenössischen Experimenten. Die vorliegende Arbeit demonstriert die Funktionsweise eines Talbot-Lau-Interferometers mit einer Vielzahl unterschiedlicher Atome und zwar mit Wasserstoff, Helium, Argon, Krypton und Xenon. Dieses Interferometer besteht aus drei Gittern und wird eingehend untersucht hinsichtlich der wichtigsten Umstände, welche die Qualität des Interferenzmusters beeinflussen. Besonderes Augenmerk liegt hierbei auf den Ausrichtungsanforderungen der Gitter und den auftretenden Wechselwirkungen zwischen den Atomen und den Gitterstäben. Der experimentelle Aufbau, der im Rahmen dieser Arbeit geleistet wurde, wird ausführlich diskutiert und mit zahlreichen Messungen charakterisiert. Diese Messungen, die einen wichtigen Schritt für das eigentliche Interferometer darstellen, liefern verschiedene Informationen, wie zum Beispiel die Zusammensetzung des Teilchenstrahls, die Einheitlichkeit der einzelnen Gitterperioden und die Auflösung der Interferenz-Streifenmuster. Das konstruierte Interferometer arbeitet erfolgreich mit Teilchen, deren de-Broglie-Wellenlängen mehr als zwei Größenordnungen umfassen, d.h. $\lambda_{dB} \in [0.02 \text{ pm}, 2.2 \text{ pm}]$, und ermöglicht so die Beobachtung des Übergangs zum klassischen Äquivalent des Talbot-Lau-Interferometers, dem Moiré-Deflektometer. Die genaue Form des Interferenzmusters gibt einen Einblick in auftretende Wechselwirkungen innerhalb der Gitter, die durch gitterinterne Ladungen erklärt werden. Darüber hinaus wird gezeigt, wie das Interferometer als Spektrometer eingesetzt werden kann. Um auch die Wellennatur von Ionen zu untersuchen, werden die Voraussetzungen und deren experimentelle Umsetzung für ein funktionierendes Talbot-Lau-Interferometer mit Protonen diskutiert.

F

Contents

1. Introduction	15
1.1. Wave-Particle Duality: A Historical Review	15
1.2. Motivation and Contents	17
2. From Talbot-Lau Interferometry to Classical Moiré Deflectometer	19
2.1. Talbot-Lau Interferometry – an Introduction	19
2.2. First Grating: The Talbot Effect – Plane Wave Illumination	22
2.3. Second Grating: Talbot-Lau Interferometry – Diffuse Illumination	27
2.4. Third Grating: Moiré Effect – Resolving the Nanoscopic Pattern	29
2.5. Talbot-Lau in Wigner Representation	31
2.5.1. Wigner Function, its Free Evolution and Passage Through a Grating .	32
2.5.2. Propagation Through the Talbot-Lau Setup	33
2.5.3. Signal of the Talbot-Lau Interferometer with Pure Transmission Gratings	34
2.6. The Classical Limit: Moiré Deflectometer	37
2.6.1. Pattern Formation with Geometrical Trajectories	37
2.6.2. Classical Phase-Space Representation	39
2.7. From Quantum Description to Classical Trajectories	40
2.8. Summary	41
3. Visibility-Affecting Factors	43
3.1. Alignment Requirements of the Three-Grating Setup	43
3.1.1. Longitudinal Position of the Gratings	44
3.1.2. Grating Pitch	44
3.1.3. Rotational Alignment	47
3.1.4. Tilt Angle	49
3.2. Vibrations of the Three-Grating Setup	51
3.2.1. Fixed Harmonic Oscillation	51
3.2.2. Independent Grating Oscillations	53
3.3. Perturbations due to External Forces Acting on the Particles	55
3.3.1. Inertial Sensitivity of the Three-Grating Setup	55
3.3.2. Critical Acceleration and the Effect of Finite Energy Distribution . . .	57
3.3.3. Different Forces Arising in the Setup	59

Contents

3.4. Realistic Gratings with Intra-Grating Interaction	60
3.4.1. Mathematical Description of Intra-Grating Interactions	60
3.4.2. Intra-Grating Interactions	62
London Dispersion Force	62
Induced Electric Dipole and Electric Field Gradient	63
Coulomb Interaction	64
3.4.3. Limit of the Eikonal Approximation and Effective Open Fraction . . .	65
3.4.4. Effect of Intra-Grating Interactions	66
3.5. Summary	69
4. Experimental Setup: Characteristics and Performance	71
4.1. Making Well-Defined Particle Beam	71
4.1.1. ECR Ion Source	73
4.1.2. Wien Filter: Spectrum of the Source	75
4.1.3. Energy Spread	77
4.1.4. Neutralisation Chamber: Well-Defined Neutral Particle Beam	78
Neutralisation with Metal Target	80
Neutralisation of Multiple Charged Ions	81
4.1.5. Pinholes to Control Beam's Divergence	81
4.2. Talbot-Lau Interferometer	82
4.2.1. Gratings	82
4.2.2. Actuators: Aligning and Scanning the Gratings	84
4.3. Magnetic and Electric Shielding	86
4.3.1. Mu-Metal to Shield the Earth's Magnetic Field	86
4.3.2. Faraday Cage to Avoid Influence of Stray Electric Fields	87
4.4. Detection System and Data Acquisition of Fringe Pattern	88
4.4.1. Microchannel Plate - Phosphor Screen - Camera	89
Microchannel Plate	89
Phosphor Screen	90
Camera	90
4.4.2. Single-Particle Detection: High Spatial Resolution	91
Algorithm to Retrieve Coordinates of Single-Particle Impact	91
Statistics and Resolution of Single-Particle Impacts	92
4.4.3. The Rayleigh Test: Efficient Way of Receiving Pattern's Period, Ori- entation, and Visibility	94
The Rayleigh Test Performance	95
4.4.4. Integrated Data Acquisition: Saving Time	97
4.4.5. Single-Particle Detection versus Integrated Picture: Accuracy versus Time	99
4.5. Characterising Single Components by Using the Setup as a Whole	100
4.5.1. Photons Originating from the Source	100

4.5.2. Systematic Study of Individual Actuator Movements and their Informative Value about the System	102
y -Scan: Proof of Nanometric Moiré Fringes	102
α -Scan: Precision of the Grating Pitch	102
z -Scan: Beam's Divergence	105
4.5.3. Stability of the Interferometer	106
4.6. Summary	107
5. From Classical Xenon Fringes to Hydrogen Interferometry	109
5.1. Necessity of Considering Quantum Behaviour	109
5.2. Talbot-Lau Interferometer as a Spectrometer	113
5.3. Strength of Intra-Grating Interactions	116
5.4. Ion Interferometer with Material Gratings	119
5.5. Summary	121
6. Conclusion and Outlook	123
Bibliography	125
A. Constants	135
B. Publications	137
C. Note of Gratitude	141

1. Introduction

The wave-particle duality of light and matter is a cornerstone of modern physics. Louis de Broglie, a French physicist of the early 20th century, was puzzled by the fact that, on the one hand, for light two contradictory theories – that of waves and that of corpuscles – seem to hold true, and, on the other hand electrons within an atom can only perform distinct motions among the infinity of classical possible motions [1]. De Broglie thus postulated in 1923 in his PhD thesis [2]: *for both matter and radiations, light in particular, it is necessary to introduce the corpuscle concept and the wave concept at the same time* [1]. The fundamental relation of his theory is the association of a characteristic wavelength λ_{dB} to particles, later called the de Broglie wavelength, and defined as:

$$\lambda_{\text{dB}} = \frac{h}{p}, \quad (1.1)$$

where p is the momentum of the particle and h the Planck constant. This proposed connection of wave behaviour with the idea of a particle – the wave-particle duality – has given rise to a great set of new experiments, whose modern incarnations entertain physicists up to this day. Yet, the concepts of particles and waves were already present long ago. Hence, to have a better understanding of the time period during which de Broglie came up with his idea, the following section gives a brief overview of the history of wave-particle duality to date. Thereafter, the content of this work is explained as a part of the lasting story of wave-particle duality.

1.1. Wave-Particle Duality: A Historical Review

The concept of atoms and particles as basic building blocks of the world around us goes back already to the philosophers of the antiquity. At this time, a corpuscular understanding of matter as well as of light can be found formulated for example by Democritus (460-370 BC) or later mentioned by Lucretius (98-55 BC) and Seneca (4 BC - 64 AD) [3]. On the other hand, the conceptual idea of the medieval English bishop Grosseteste (1168-1253) of comparing light propagation with the vibration and motion of sound was maybe one of the first attempts at a wave theory of light [4].

However, a comprehensive theoretical description of both ideas is primarily found 500 years later, with Christiaan Huygens (1629-1695) and his contemporary Isaac Newton (1643-1727).

1. Introduction

Newton adapted his material point dynamics for the behaviour of light and hence developed the corpuscular theory [5], while Huygens defended the idea of an underlying wave nature, whereby each point on the wavefront is a source of elementary spherical waves [6].

One hundred years later in 1803, this question seemed to be settled when Thomas Young (1773-1829) performed his famous double-slit experiment and hence discovered interference phenomena. Augustin-Jean Fresnel (1788-1827) interpreted interference with the help of the Huygens principle and hence disproved the corpuscular theory of light. James Clerk Maxwell (1831-1879) and Heinrich Hertz (1857-1894) further developed the wave concept of light.

At the same time, the physics of matter was pushed forward, suggesting an atomic, i.e. corpuscular theory. In this context, the law of multiple proportions discovered by the British chemist John Dalton (1766 - 1844) or the evolution of the kinetic gas theory, both of which assume an underlying corpuscular structure, stand out as prime examples of the progress achieved on this front.

Hence, at the turn of the 20th century two seemingly disjoint theories to explain matter and light were present. The corpuscular theory following Newtonian mechanics for the physics of matter on the one hand, and the concept of waves following the ideas of Huygens and Fresnel for describing optical phenomena on the other. Such two disjoint theories gave rise to the question about energy exchange between matter and radiation and hence to the question about black body radiation. Using classical assumptions led to the formulation of the Rayleigh-Jeans law which states that a black body radiator would tend to the absolute zero of temperature. This was later referred to as the ultraviolet catastrophe [7] and hence not consistent with experimental results. Max Planck avoided this problem, positing that a black body emits radiation only in integer multiples of $h\nu$, where ν is the frequency of light. Planck's idea that light is emitted in specific amounts of energy, called *quanta*, gave rise to the question about a granular structure of light. It needed only five years until Albert Einstein discovered the photoelectric effect in 1905 and hence verified the existence of such a corpuscular structure of light thereby reviving Newton's hypothesis. Nevertheless, it was still necessary to consider the wave-like behaviour of light so that Einstein was forced to state: *It seems as though we must use sometimes the one theory and sometimes the other, while at times we may use either* [8]; a statement which paraphrases what lies at the core of the wave-particle duality.

In the field of atomic physics, great progress was achieved by Ernest Rutherford who discovered that an atom consists of a positively charged nucleus surrounded by negative charged electrons. With such an understanding of the atom, Niels Bohr came up with a new theory of the atomic structure in 1913. To explain hydrogen's characteristic spectrum, Bohr postulated that electrons in an atom are fixed in orbits around the nucleus, with only a small number of stable orbits determined by the Planck constant h .

Here we have approached the historical point mentioned above, when Louis de Broglie published his PhD thesis to resolve the discrete states inside an atom and expanded the wave-particle duality for the field of matter, introducing the de Broglie wavelength in the process. It only needed three years until in 1927 that Davisson and Germer [9] prove de Broglie's hypothesis by diffracting electrons on a crystal, hence paving the way for numerous matter

wave experiments. The field of matter waves was extended by Estermann and Stern three years later to the helium atoms and the hydrogen molecule [10]. In 1936, interference of neutrons was shown by Halban and Preiswerk [11] and by Mitchell and Powers [12]. With the development of lasers and the possibility of producing grating structures on the nanometric scale, the door to large and complex molecules was opened in 1999 by Zeilinger, who showed interference with the fullerenes C_{60} and C_{70} [13, 14]. In the most recent development, Arndt has been pushing the limit towards the macroscopic world by steadily increasing the mass of the interfering objects [15–17]. In 2019 he demonstrated interference with molecules beyond 25 kDa, i.e. molecules consisting of more than 2000 atoms [18]. Furthermore, also worth mentioning are the first experiments in the field of antimatter, with positron interferometry achieved in 2019 [19].

Besides showing the wave nature for multiple particles, matter wave interferometry has been used to perform high precision measurements, for example on the electric polarisability of sodium [20], or the rotation of the Earth [21]. Furthermore, there are multiple proposals for matter wave experiments designed to show the Aharonov-Bohm effect [22–24], to look for deviations from Coulomb’s law [25], to set bounds on the continuous spontaneous localisation model [26], or to test the superposition principle looking for multipath interference [27].

With such a broad applications of matter wave interferometers, still at least one field is lacking: ion interferometry. In spite of multiple successful experiments with electrons [28, 29] an ion interferometer has not been successfully realised up to date. A single result with ions in a German PhD thesis could not be reproduced [30]. The group of Stibor from the University of Tübingen is currently trying to achieve this goal with a biprism interferometer and a single-tip source [24, 31, 32], but has not been successful thus far. Furthermore, multiple proposals exist requiring an ion interferometer [24, 25], as for example with antiprotons [33, 34].

1.2. Motivation and Contents

This work intends to take part in the history of the wave-particle duality on two sides. First it shows the transition between the wave regime to the classical case with a single setup and second gives an insight to the feasibility of an ion interferometer with material gratings.

The tool of choice is a three-grating setup, which is described as classical moiré defelectometer and its wave-mechanical counterpart, the Talbot-Lau interferometer, depending on the de Broglie wavelength of the impinging particles. With such an experiment, is readily available a tool with a wide acceptance range for different de Broglie wavelengths. Hence, we use this device to show systematically the working principle of such a Talbot-Lau interferometer and to demonstrate the transition to the classical regime by using several particle species without altering the geometry and the characteristics of the measuring device. The result obtained by such an experiment is then used to estimate limits in which the same device could be used to achieve ion interferometry.

The work is structured as follows: Chapter 2 provides the necessary theoretical basis reviewing Talbot-Lau interferometry and the moiré defelectometer, and contains a full mathematical description of the expected signal. Particular attention is paid to providing an intuitive access to the key features of such a device, as well as to discussing the limit between the

1. Introduction

classical and the wave regime. With the provided idea of an ideal setup, chapter 3 discusses perturbation factors due to imperfections in the experimental setup, such as misalignments, or due to external influences, such as electric and magnetic fields, or vibrations. Chapter 4 discusses in detail the experimental setup from the particle source all the way down to the detector. This includes measurements to characterise parts of the experiment, which is a step towards a working Talbot-Lau interferometer. The results of the three-grating setup and their discussion is presented in chapter 5. Special attention is paid showing the transition between the wave-regime to the classical description and how the atomic-interference pattern gives an insight to the feasibility of ion interferometry with the same device.

2. From Talbot-Lau Interferometry to Classical Moiré Deflectometer

The experiment presented in this work envisions to show atomic interference phenomena and their classical limit with one single setup. For this purpose the interferometer of choice is the Talbot-Lau interferometer due to its wide acceptance range of different masses and velocities, and hence for different de Broglie wavelengths. It consists of three equidistant placed gratings and is a well established tool to show interference phenomena with spatially incoherent sources. The first grating establishes coherence in the beam, the second lets the beam interfere and the third resolves the nanoscopic fringe pattern. Such an interferometer has a wide range of applications, in interference of atomic [35] or heavy molecular beams [14], of electrons [29, 36] or different light sources [37]. In the classical limit this device is traditionally called moiré deflectometer [34, 38, 39].

In the following we start with providing a general introduction to Talbot-Lau interferometry to go into a more detailed description in the subsequent parts. We give sequential derivation and discussion of the underlying phenomena for each grating separately which provides an intuitive access to the Talbot-Lau interferometer. This is followed by a fully analytical description which results in simple expressions for the visibility – the signal – of a given Talbot-Lau setup realised with different wavelengths. Subsequently the moiré deflectometer is introduced and finally presented as the short-wave limit of the Talbot-Lau interferometer. The theoretical framework described in this chapter serves as a basis for the topic studied in the next chapter, where minor aberrations from the ideal setup are discussed, but also for the full experiment, to show the transition between the quantum regime and the classical limit in one system.

2.1. Talbot-Lau Interferometry – an Introduction

The Talbot-Lau interferometer is named after the British scientist William H. F. Talbot and the German physicist Ernst Lau. In 1836 the former one observed that after a grating was illuminated with coherent light, self-images of the grating were observed at integer multiples of a certain distance [40], later called the Talbot length L_T . This effect – the Talbot effect – as part of the near-field or Fresnel regime, was analytically described 45 years later by Lord

2. From Talbot-Lau Interferometry to Classical Moiré Deflectometer

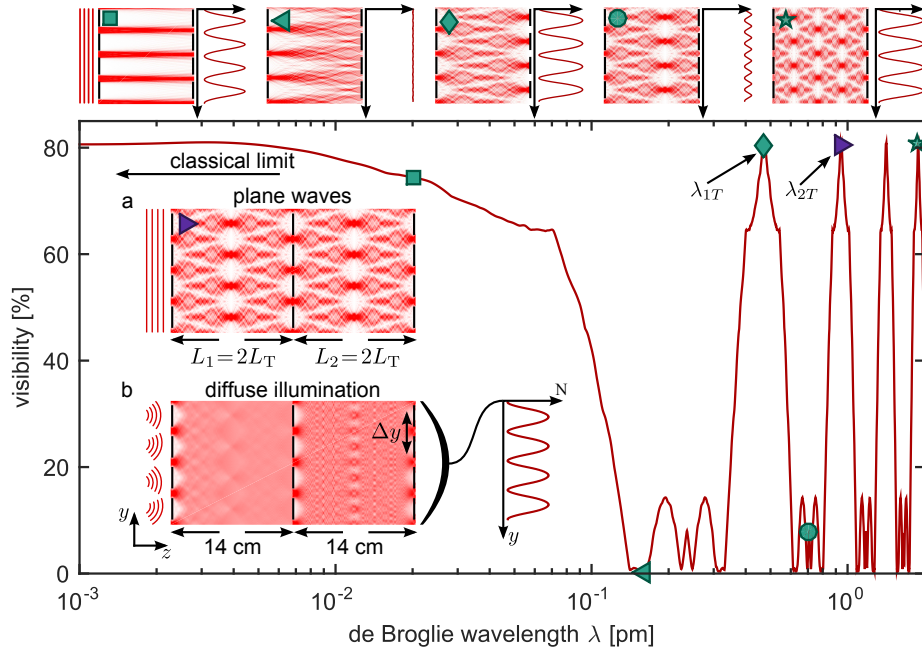


Figure 2.1.: Working principle of a three-grating Talbot-Lau interferometer illuminated with a spatially incoherent source: (a) Talbot carpet after a plane wave illumination of the first grating. At integer multiples of the Talbot length L_T a grating's self-image is observed. (b) A diffuse source smears out the Talbot carpet. The Talbot-Lau interferometer therefore requires a second grating, displaced at an integer multiple of the Talbot length. Now the first grating produces coherence in the beam for the second one, resulting in a Talbot carpet after the second grating similar to the one generated with a plane wave. The nanoscopic pattern in the plane of the third grating is resolved with a third grating, which can be either vertically scanned or tilted around the beam axis. The full graph shows the visibility evolution as a function of the de Broglie wavelength for a setup with a grating distance $L = 14$ cm and a grating pitch $d = 257$ nm, as used in this work. The visibility peaks are at the points where the wavelength corresponds to a Talbot length which is an integer fraction of the grating distance L . The visibility at this point cannot be distinguished from the classical limit $\lambda \ll \lambda_{1T}$. On top of the graph the Talbot carpets are shown for different positions in the visibility plot with the intensity profile after a scanned third grating.

Rayleigh [41], with the Talbot length L_T as

$$L_T = \frac{d^2}{\lambda} . \quad (2.1)$$

Here d is the grating period and λ the wavelength of the used particles. Later the whole pattern behind a coherently illuminated grating, the so-called Talbot carpet, was extensively studied, which revealed the fractional Talbot effect, showing images with shorter periods at rational multiples of the Talbot length [42].

Coherent illumination is crucial in order to observe the Talbot carpet. If the grating is irradiated with a diffuse source, the whole pattern is smeared out (compare figure 2.1(b)). Ernst Lau showed in 1948 that adding a second grating at an integer multiple of the Talbot length affects a Talbot carpet similarly to Talbot-carpet with a plane wave [43] (figure 2.1(b)), which is the basis for an interferometer with spatially incoherent sources.

The nanoscopic pattern generated behind the second grating is detected with a third grating. This grating can either scan the pattern while the total flux over the last vertical grating position is measured, or magnify the pattern with the help of the moiré effect.

With the same three-grating setup, a classical analogue – the moiré deflectometer – can be obtained if the wavelength λ is sufficiently small. The moiré deflectometer has been successfully used in the field of atomic optics, as it has a high sensitivity to external forces, similar to the Talbot-Lau interferometer. This instrument has been successfully employed to measure the gravitational force on argon atoms [38], or electric and magnetic fields on antiprotons [44] as well as on different hydrogen ions [45, 46].

One can estimate the limit between the wave regime and the classical regime from the grating equation,

$$d \sin(\theta_n) = n\lambda . \quad (2.2)$$

The classical limit is realised if the first-order diffraction angle is so small that the diffracted beam is displaced by much less than one grating period on the following grating, positioned distance L beyond the first grating:

$$L \frac{\lambda}{d} = L \sin(\theta_1) \approx L\theta_1 \ll d . \quad (2.3)$$

Therefore, the setup can be described in classical terms for the limit

$$L \ll \frac{d^2}{\lambda} = L_T , \quad (2.4)$$

which is, interestingly, identical to the Talbot length.

The fringe pattern in the classical limit of the Talbot-Lau interferometer cannot be distinguished from the pattern in the wave regime if the grating separation is set to a multiple integer of the Talbot length. A significant deviation from this pattern is observed if the distance does not match the Talbot length. An appropriate measure for the fringe pattern is

2. From Talbot-Lau Interferometry to Classical Moiré Deflectometer

the visibility ν , which is visually related to the contrast and is defined as

$$\nu = \frac{I_{\max} - I_{\min}}{I_{\max} + I_{\min}}, \quad (2.5)$$

with I_{\max} and I_{\min} the maximal and minimal intensity of the pattern. For practical reasons in the experiment it is much easier to keep the grating distances L fixed while the de Broglie wavelength for the beam is tuned. Therefore equation (2.1) can be rewritten as

$$\lambda_{nT} = \frac{d^2}{L}n, \quad (2.6)$$

where λ_{nT} is the de Broglie wavelength for which the grating distance fits n -times the Talbot length. The classical limit is accordingly given by

$$\lambda \ll \frac{d^2}{L}. \quad (2.7)$$

Figure 2.1 gives the visibility over the wavelength for a fixed grating distance of $L = 14$ cm and a grating period of $d = 257$ nm, as used in this work. Following equation (2.6) the same visibility is expected for the wavelengths $\lambda_{nT} = n \cdot 0.47$ pm, since in the classical limit $\lambda \ll 0.47$ pm. This artefact is clearly visible in the graph, as for the λ_{nT} a peak in the visibility appears. If the wavelength does not match the Talbot length of the given setup, the visibility is drastically reduced. The small pictures on top of figure 2.1 show the underlying Talbot carpets for various de Broglie wavelengths in the graph. Here it is made clear how the Talbot carpet has to fit the grating distance in order for a high contrast signal to appear. The given fringe pattern after the Talbot carpet gives the intensity after the last grating if it is scanned vertically. From this fringe the visibility is evaluated.

Having provided a general overview to Talbot-Lau interferometry and its classical limit the moiré deflectometer, a more detailed description of the underlying theory will be presented in the subsequent parts. For this purpose we discuss the physics and the underlying phenomena behind each grating separately to provide an intuitive access to the Talbot-Lau interferometer.

2.2. First Grating: The Talbot Effect – Plane Wave Illumination

The following systematic derivation of the Talbot effect is based on the angular spectrum method, also known as the plane-wave decomposition. It is one of the basic analytic tools in this work to compute intensity fields such as the Talbot carpets shown in figure 2.1. Furthermore, it gives an intuitive understanding of the key features of the Talbot effect. The hereby presented derivation follows previous work done in this field [34, 47, 48].

The angular spectrum method is used to propagate wavefields from an initial source plane, in this work the plane of the first grating ($z = 0$), to a destination plane ($z > 0$). It is frequently used in the field of optics [49–51] as well as for calculating the propagation of acoustic fields [52]. The method follows four major steps, which are discussed in detail subsequently:

- 1) Defining the wavefield at the initial plane $z = 0$ in its complex components.

2.2. First Grating: The Talbot Effect – Plane Wave Illumination

- 2) Decomposing the wavefield into its plane wave components, the so called angular spectrum, with a Fourier Transform.
- 3) Propagating each plane wave component in the Fourier domain to the destination plane. This quantifies the phase shift that each plane wave builds up to the destination plane.
- 4) Reconstructing the wavefield in the plane of destination with the inverse Fourier transform.

1) Defining the Wavefield: For the purposes of this work, we restrict our analysis to two dimensions, as depicted in figure 2.2(a) with the beam axes along the z - and y -axis which are parallel to the grating vector. The gratings are assumed to be infinitely thin pure-transmission gratings and hence can be expressed as

$$g(y, d, \eta) = \begin{cases} 1 & \text{if } \text{mod}(y, d) < \eta d \\ 0 & \text{otherwise} \end{cases} . \quad (2.8)$$

Here the grating transmission function g is 1 if a particle can pass through the grating, and 0 if it cannot. The parameters d and η denote the grating period and the open fraction, respectively. The open fraction is defined as the ratio of the slit width b over the period, i.e. $\eta = b/d$. Such an infinitely long grating can be expressed by means of a Fourier series with the grating vector $k_d = 2\pi/d$ as:

$$g(y, d, \eta) = \sum_{n=-\infty}^{\infty} c_n e^{ink_d y} = \sum_{n=-\infty}^{\infty} c_n e^{ik_n y} , \quad (2.9)$$

where we have used $k_n = nk_d$. For a given rectangularly shaped grating function with an initial phase $\phi = 2\pi\Delta y/d$ the Fourier coefficients are

$$c_n = \frac{1}{d} \int_{-\frac{d}{2}}^{\frac{d}{2}} dy g(y, d, \eta) e^{-ink_d y} \quad (2.10)$$

$$= \frac{1}{d} \int_{-\frac{\eta d}{2} - \Delta y}^{\frac{\eta d}{2} + \Delta y} dy e^{-ink_d y} \quad (2.11)$$

$$= \frac{i}{2\pi n} \left(e^{-ink_d y (\frac{\eta d}{2} + \Delta y)} - e^{-ink_d y (-\frac{\eta d}{2} + \Delta y)} \right) \quad (2.12)$$

$$= \eta \text{sinc}(n\eta) e^{-ink_d y \Delta y} =: c'_n e^{-ink_d y \Delta y} . \quad (2.13)$$

The initial wavefield $u(y, z = 0^+)$ for a plane wave $u(y, z) = e^{i(k_y y + k_z z)}$ impinging on such a grating is the product of the grating function with the plane wave (0^- and 0^+ denotes for

2. From Talbot-Lau Interferometry to Classical Moiré Deflectometer

the wavefield directly before and after the grating):

$$u(y, z = 0^+) = u(y, z = 0^-) \cdot g(y) = \sum_{n=-\infty}^{\infty} c_n e^{i(k_y + k_n)y} . \quad (2.14)$$

As can be seen, the field at the grating consists of a series of plane waves with the wave vectors $k'_n = k_y + k_n$. With the dispersion relation $k'^2 = k_y^2 + k_z^2 = (2\pi/\lambda)^2$ the two components k_y and k_z are connected by

$$k_z = \pm \sqrt{\left(\frac{2\pi}{\lambda}\right)^2 - k_y^2} . \quad (2.15)$$

Furthermore and not surprisingly, the wave vectors $k'_n = k_y + k_n = k \sin(\beta) + n(2\pi/d) = k \sin(\alpha)$ contain the well-known diffraction angles of the grating equation

$$d(\sin(\theta_n) - \sin(\beta)) = n\lambda , \quad (2.16)$$

where β denotes the incident angle of the incoming plane wave.

2) Decomposing the Wavefield: With the initial wavefield defined (equation (2.14)), the second step of the angular spectrum method is to decompose the wavefield into its plane wave components by means of a Fourier transform. The Fourier transform for a given scalar field $u(y, z = 0)$, and hence for the wavefield, is

$$\tilde{u}(k_y) = \mathcal{F}_y\{u(y, z = 0)\} = \int_{n=-\infty}^{\infty} dy u(y, z = 0) e^{-ik_y y} . \quad (2.17)$$

Utilising $\int dy \exp(iky) = \delta(y)$ and the obtained initial wavefield from equation (2.14) the Fourier transform yields

$$\tilde{u}(k_y) = \sum_{n=-\infty}^{\infty} c_n \int_{n=-\infty}^{\infty} dy e^{i(k'_n y - k_y y)} \quad (2.18)$$

$$= \sum_{n=-\infty}^{\infty} c_n \delta(k'_n - k_y) . \quad (2.19)$$

3) Propagating in the Fourier Domain: The next step propagates each plane wave to the observational plane z . Over the distance between the initial plane ($z = 0$) and the destination plane z each wave accumulates a phase $e^{ik_z z}$. Using equation (2.15), the following propagator can be defined:

$$\mathcal{P}_{k_y}(z) := e^{iz\sqrt{\left(\frac{2\pi}{\lambda}\right)^2 - k_y^2}} . \quad (2.20)$$

2.2. First Grating: The Talbot Effect – Plane Wave Illumination

For the angular spectrum in the observational plane this yields

$$\tilde{u}'(k_y) = \tilde{u}(k_y) \cdot \mathcal{P}_{k_y}(z) = \sum_{n=-\infty}^{\infty} c_n \delta(k'_n - k_y) e^{iz\sqrt{\left(\frac{2\pi}{\lambda}\right)^2 - k_y^2}}. \quad (2.21)$$

4) Reconstructing the Wavefield: The last step reconstructs the wavefield from the Fourier spectra with the inverse Fourier transform

$$u(y, z) = \mathcal{F}_{k_y}^{-1}\{\tilde{u}'(k_y)\} = \frac{1}{2\pi} \int_{-\infty}^{\infty} dk_y \tilde{u}'(k_y) e^{ik_y y}. \quad (2.22)$$

This gives the final result of the wavefield at the plane z behind a grating illuminated with a plane wave:

$$u(y, z) = \frac{1}{2\pi} \sum_{n=-\infty}^{\infty} c_n \int_{-\infty}^{\infty} dk_y \delta(k'_n - k_y) e^{iz\sqrt{\left(\frac{2\pi}{\lambda}\right)^2 - k_y^2}} e^{ik_y y} \quad (2.23)$$

$$= \sum_{n=-\infty}^{\infty} c_n e^{iz\sqrt{\left(\frac{2\pi}{\lambda}\right)^2 - k_n'^2}} e^{ik_n' y}. \quad (2.24)$$

Discussing the Result: In order to better understand the Talbot effect, the obtained full description of the wavefield can be simplified with the paraxial approximation

$$\sqrt{\left(\frac{2\pi}{\lambda}\right)^2 - k_n'^2} \approx \frac{2\pi}{\lambda} - \frac{\lambda}{4\pi} k_n'^2 \pm \dots. \quad (2.25)$$

If a plane wave impinges on the grating perpendicularly, $k_y = 0$ and therefore $k'_n = k_n = nk_d = n(2\pi/d)$. The field follows as

$$u(y, z) \approx e^{iz\frac{2\pi}{\lambda}} \sum_{n=-\infty}^{\infty} c_n e^{ik_n y} e^{-i\pi\frac{n^2}{L_T} z}, \quad (2.26)$$

where the Talbot length (equation (2.1)) $L_T = d^2/\lambda$ has been inserted. Interestingly, this result is similar to the wavefield directly behind the grating (equation (2.14)), except for the additional phase factors $e^{iz\frac{2\pi}{\lambda}}$ and $e^{-i\pi\frac{n^2}{L_T} z}$. The first phase factor can be neglected, as only the intensity $I = u^*u$ is measured in the experiment. If the distance z equals an even integer of the Talbot length, the second phase factor equals 1, resulting in a pattern identical with the initial plane

$$u(y, z = 2mL_T) \approx u(y, z = 0) \quad \text{for } m \in \mathbb{N}. \quad (2.27)$$

2. From Talbot-Lau Interferometry to Classical Moiré Deflectometer

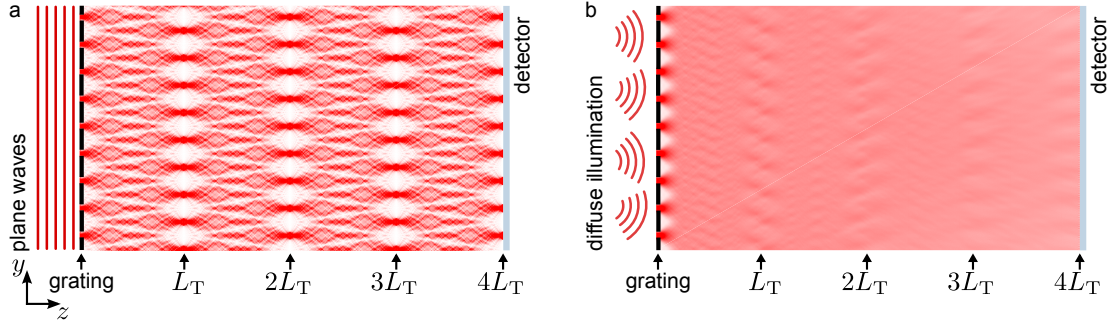


Figure 2.2.: The Talbot effect. (a) Behind a grating illuminated with a plane wave, self-images of the grating are observed. These images appear at integer multiples of the so-called Talbot length $L_T = d^2/\lambda$. A detector placed at the position of such a self-image can detect a high-visibility fringe pattern. For even multiple of the Talbot length the self-images are in phase with the illuminated grating, while for odd multiples the image is shifted by half a period. The whole pattern behind the grating is called the Talbot carpet. (b) If the grating is illuminated with a diffuse source the Talbot carpet is smeared out, making the high contrast self-images disappear.

This is the reason why the observed patterns are called self-images and hence one often finds an alternative definition of the Talbot length in literature, namely $L'_T = 2d^2/\lambda$. At distances with an odd integer multiple of the Talbot length (i.e. $z = (2m + 1)L_T$ for $m \in \mathbb{N}$) the last phase factor in equation (2.26) becomes $e^{-i\pi n}$. The resulting pattern can then be described as:

$$u(y, z = (2m + 1)L_T) \approx e^{iz\frac{2\pi}{\lambda}} \sum_{n=-\infty}^{\infty} c_n e^{ik_n y} e^{-i\pi n} \quad (2.28)$$

$$= e^{iz\frac{2\pi}{\lambda}} \sum_{n=-\infty}^{\infty} c_n e^{i(\frac{2\pi}{d}ny - \pi n)} \quad (2.29)$$

$$= e^{iz\frac{2\pi}{\lambda}} \sum_{n=-\infty}^{\infty} c_n e^{in\frac{2\pi}{d}(y-d/2)} \quad (2.30)$$

$$= u(y - d/2, z = 0) . \quad (2.31)$$

This results states that for odd integer multiples of the Talbot length the self-image of the gratings is shifted by half a period. This artefact can be clearly seen in figure 2.2(a) where self-images of the grating appear at integer multiples of the Talbot length L_T , while for odd multiples the pattern is shifted by half a period.

Extension to Diffuse Illumination: Throughout this work, all illustrated intensity fields are computed numerically following the aforementioned pathway of the angular spectrum method. Therefore the intensity $I = u^*u$ is displayed. If the first grating is illuminated diffusely, as it is the case for the Talbot-Lau interferometer, the intensity field is simulated by summation

2.3. Second Grating: Talbot-Lau Interferometry – Diffuse Illumination

of the single-intensity fields resulting from plane waves with different incident angles β :

$$I = \sum_{\beta} I_{\beta} \quad \text{with} \quad I_{\beta} = u_{\beta}^* u_{\beta} \quad \text{and} \quad \vec{k} = [\sin(\beta), \cos(\beta)]^T k. \quad (2.32)$$

As shown in figure 2.2(b) the Talbot carpet is smeared out after the illumination of the first grating with a diffuse source, making a second grating necessary, as discussed in the following.

2.3. Second Grating: Talbot-Lau Interferometry – Diffuse Illumination

As we saw in the previous section, coherent illumination is crucial to observe the Talbot effect. Ernst Lau showed in 1948 [43] why a similar effect can be observed with a diffuse wave source and a second grating. Figure 2.3 follows his exposition and shows an enlarged view of the two involved gratings with a period d and a separation L . For his argumentation, Lau assumed that the slits of the grating are small compared to the pitch so that each slit can be seen as a point source. In figure 2.3 two rays are highlighted starting at point A at the first grating and propagating towards two neighbouring slits B and D at the second grating. The black circle depicts the points of identical phase and cuts the second ray at C . Therefore, the phase difference between the two rays at the second grating is CD . A tangent to the circle at point C cuts for small angle α the distance BD in two equidistant parts, from which it follows that $BE = 2CD$. It can be seen that for a small angle α the phase difference CD equals one wavelength λ if

$$L = \frac{d^2}{2\lambda} = \frac{L_T}{2}, \quad (2.33)$$

using the relations $CD = BE/2$, $BE/d = \sin(\alpha) \approx \alpha$, $d/L = \tan(\alpha) \approx \alpha$ and the known Talbot length $L_T = d^2/\lambda$. In such a configuration, the second grating is illuminated with a plane wave which results in a Talbot carpet similar to the case with one grating and a plane wave.

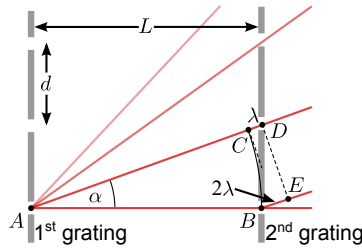


Figure 2.3.: Schematic representation of neighbouring rays as used by Ernst Lau to show how the first grating can prepare coherence in a diffuse beam for the second one [43]. The phase difference of two neighbouring rays equals one wavelength λ if the grating distance L matches half the Talbot length. The second grating therefore appears to be illuminated by a plane wave. Image adapted from [34].

2. From Talbot-Lau Interferometry to Classical Moiré Deflectometer

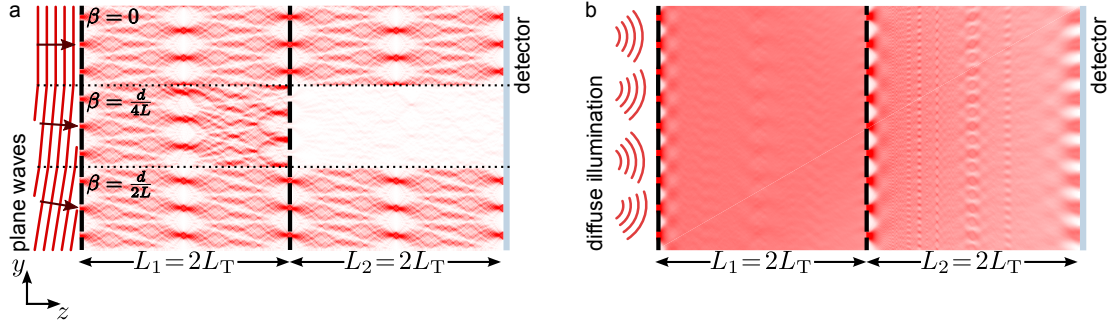


Figure 2.4.: Principle of a Talbot-Lau interferometer which requires a second grating. (a) A diffuse illumination of the first grating can be depicted as a sum of plane waves with different directions. Only those waves can pass the second grating for which the self-image of the first grating is in phase with the second one. Therefore the second grating has to be placed at a multiple integer of the Talbot length L_T . In the depicted case only waves with an incident angle $\beta = nd/L_1$ ($n \in \mathbb{Z}$) can pass the second grating. All waves passing the second grating have another self-image which is in phase at the same distance $L_2 = L_1$ behind the second grating. (b) The Talbot-Lau pattern for a diffuse illumination. Behind the first grating no diffraction pattern is observed while with a second grating the pattern observed on the detector remains. (The intensity of the pattern behind the second grating has been normalised in intensity with the open fraction of the grating. This compensates the loss due to transmission through the second grating.)

Consequently the first grating generates the spatial coherence for the second one and gives an intuitive explanation of the working principle of a near-field interferometer, such as the Talbot-Lau interferometer, with uncollimated sources.

A usual practice in many experiments [34,46,47,53] is to set the distance between the gratings to an integer multiple of the Talbot length ($L = nL_T$ with $n \in \mathbb{Z}$). For such cases we can try another intuitive reasoning, to explain why a pattern can be still observed after a second grating, despite the diffuse illumination. Following the graphic in figure 2.4, different plane waves with varying incident angle β hit the first grating. Each of them generates a unique Talbot carpet which, however, experiences a position dependent phase shift of $\Delta y \approx z\beta$, following equation (2.24). The sum of all the individual Talbot carpets with different phase results in the already-mentioned disappearance of a diffraction pattern between the first and second grating. The second grating only lets waves pass for which the self-image is in phase with the grating. This holds in general for all incident angles which are $\beta \approx nd/L_1$ with $n \in \mathbb{Z}$. Furthermore all these waves have another grating's self-image in phase at the same distance L_2 after the second grating. From this argument it becomes also clear that the open fraction of the grating plays a crucial role, as with smaller fraction the self-images can be selected more precisely. The effect of the open fraction will be discussed in detail later in the context of the classical moiré deflectometer (chapter 2.6.1 and figure 2.6).

Implementation of the Second Grating in the Angular Spectrum Method: To compute the intensity field after the second grating with the mentioned angular spectrum method one first has to calculate the intensity field in the plane of the second grating. Afterwards, in order to obtain the field directly after the grating, this field has to be multiplied with the grating function of the second grating (compare equation (2.9)). With this field one starts the angular spectrum method from the beginning to calculate the field at an arbitrary position after the second grating. Similarly as before, this has to be repeated for a diffuse illumination several times to sum up the intensity fields for all different incident angles β .

Up to now we have seen that a diffusely illuminated two-grating system with a distance L equal to a multiple integer of the Talbot length L_T generates a self-image of the gratings at the same distance L behind the second grating. This pattern, from here on called *nanoscopic fringe pattern*, has the same periodicity d as the grating. The following section examines how to detect this fringe pattern with a third grating.

2.4. Third Grating: Moiré Effect – Resolving the Nanoscopic Pattern

To detect the nanoscopic pattern one would need a position sensitive detector with a resolution considerably smaller than the pattern period itself. Such nanometre resolution is well beyond the resolution of typical high resolution detectors, which is in the micrometre range [54, 55]. Therefore, a third grating is placed at the position of the nanoscopic pattern one wants to resolve. The idea behind a third grating is to scan the pattern or magnify it using the moiré effect. Both methods (depicted in figure 2.5) enable the detection of the fringe pattern either with a particle counter or a position-sensitive detector with a resolution in the micrometre range and are frequently used for this kind of interferometer (scanning [38], moiré effect [44–46]).

In case of scanning the third grating (figure 2.5(a)), a detector is placed behind it. This will detect maximal flux if the grating and the nanoscopic fringe pattern are in phase with each other and minimum flux if the patterns exhibit a π -shift.

The moiré effect describes the appearance of a macroscopic pattern if two similar patterns overlap. The two patterns must not be identical, but rather they have to be tilted with respect to each other or have a slightly different period. For a moiré pattern formed by two sets of parallel lines with a tilt α with respect to each other and their pitch d_1 and d_2 , a general form can be found from geometrical considerations for the period $D_{\text{moiré}}$ and the orientation angle $\alpha_{\text{moiré}}$ of the emerging macroscopic moiré pattern

$$D_{\text{moiré}} = \frac{d_1 \cdot d_2}{\sqrt{d_1^2 + d_2^2 - 2d_1d_2 \cos(\alpha)}} , \quad (2.34)$$

$$\tan(\alpha_{\text{moiré}}) = \frac{d_1 \cdot \sin(\alpha)}{d_1 \cos(\alpha) - d_2} . \quad (2.35)$$

2. From Talbot-Lau Interferometry to Classical Moiré Deflectometer

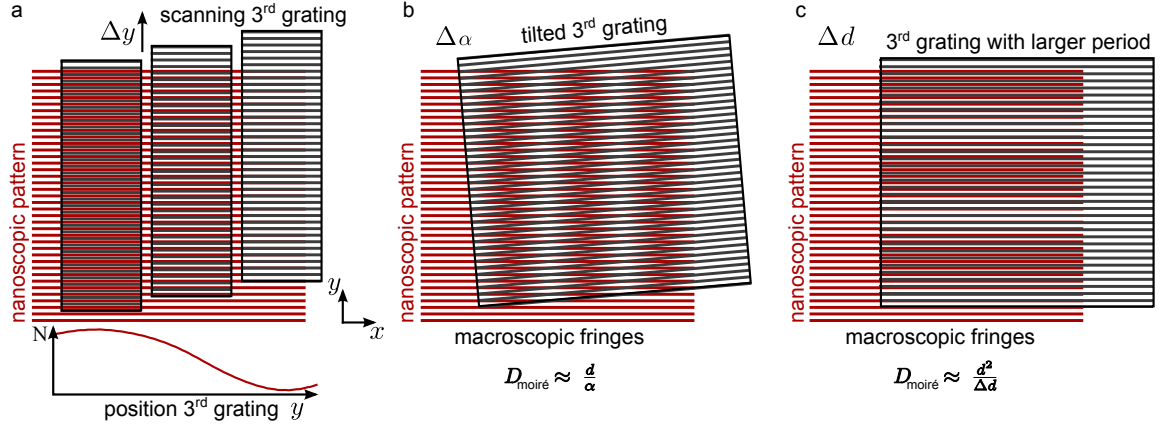


Figure 2.5.: Different ways to resolve the nanoscopic pattern with a third grating. (a) If a third grating with the same period as the pattern is scanned orthogonally to the grating structure, a particle counter behind measures maximal flux if the grating is in phase with the pattern and minimal flux if it has a phase π . (b) A tilted third grating magnifies the nanoscopic pattern by means of the moiré effect. This pattern can be detected with a spatially resolving detector. The period of the macroscopic pattern is dependent on the tilt α and equals $D_{\text{moiré}} \approx d/\alpha$. (c) The moiré effect also works for a third grating parallel to the nanoscopic pattern but with a small difference Δd in period. Macroscopic fringes parallel to the grating with a period of $D_{\text{moiré}} \approx d^2/\Delta d$ can be observed. All three measurement principles are analogue to each other. Therefore irrespective of the chosen method we refer to the obtained pattern as the *macroscopic* or *moiré* pattern.

For the Talbot-Lau interferometer the moiré effect appears between the nanoscopic fringe pattern and the third grating. In figure 2.5(b,c) two special cases of the moiré effect are depicted: In figure 2.5(b) the nanoscopic pattern and the grating have the same period ($d = d_1 = d_2$) but a small tilt with respect to each other. Prominent are the macroscopic fringes which thus emerge and which can be detected with a spatially resolving detector as they can exhibit a period in the millimetre range. The period of the moiré pattern can be simplified (for small angles α , $\cos(\alpha) \approx 1$) from equation (2.35) to

$$D_{\text{moiré}} \approx \frac{d}{\alpha} . \quad (2.36)$$

The second special case (see figure 2.5(c)), occurs when a third grating is parallel with a small variation Δd in the grating pitch. This leads to a beating parallel to the grating bars with a pitch of

$$D_{\text{moiré}} \approx \frac{d^2}{\Delta d} . \quad (2.37)$$

From symmetry considerations, it holds for the macroscopic moiré pattern that a phase shift of the last grating perpendicular to its bars directly results in the same phase shift of the macroscopic pattern.

In principle, all three detection methods are physical analogues, as the moiré effect can be interpreted as a “scan over space” either in the horizontal (rotational misalignment of each other) or vertical (minor periodic difference) direction. Mathematically, the resulting fringe $I_{\text{moiré}}$ is expressed as the convolution of the nanoscopic intensity pattern with the grating function of the third grating

$$I_{\text{moiré}} = I(y) * g_3(y) = \frac{1}{d} \int_0^d d\tau I(\tau) g_3(y - \tau) . \quad (2.38)$$

From this pattern the visibility as a significant characteristic parameter of a periodic pattern can be obtained following the definition in equation (2.5).

From a practical point of view, resolving the nanoscopic pattern with the moiré effect is more robust against fluctuations in the particles’ flux compared to a scan of the third grating. A scan has to be performed over time making the total measured flux prone to variations of the initial flux.

Up to now we have provided an intuitive access to all key features of the three-grating Talbot-Lau interferometer. The following section gives a detailed analytical description of the Talbot-Lau interferometer using the Wigner formalism.

2.5. Talbot-Lau in Wigner Representation

There is a large body of literature which studies the Talbot-Lau interferometer [34, 40, 43, 45, 47, 48, 56, 57]. This section follows the derivation of Hornberger et al. [58, 59] and is based on the Wigner representation [60]. This approach results in a simple expression for the visibility and the phase, and requires sufficiently less computational power than the angular spectrum method introduced earlier (section 2.2).

Furthermore, the Wigner representation of the quantum evolution permits a direct comparison to classical dynamics in the phase-space representation, as will be discussed in the subsequent section (section 2.6).

In the following, the Wigner function is introduced in general including its transformations under a free evolution and upon a passage through a grating. These transformations are applied step by step to the Talbot-Lau setup to conclude this section with an explicit formula for the detectable signal for a setup with pure-transmission gratings. Throughout the ensuing derivation we assume the longitudinal momentum p_z to be much larger than the transversal momenta, which allows to decouple the longitudinal and the transversal components of the wave function. $\psi_z(\mathbf{r})$ is the transverse wave function at the position z in a plane parallel to the gratings. $\mathbf{r} = (x, y)$ denotes the two-dimensional coordinates in such a plane.

2.5.1. Wigner Function, its Free Evolution and Passage Through a Grating

Wigner Function

The Wigner function is a quasi-probability distribution and is comparable to a probability distribution of a classical system in phase-space. It is defined as [60]

$$w(\mathbf{r}, \mathbf{p}) = \frac{1}{(2\pi\hbar)^2} \int d\Delta e^{\frac{i\mathbf{p}\Delta}{\hbar}} \rho\left(\mathbf{r} - \frac{\Delta}{2}, \mathbf{r} + \frac{\Delta}{2}\right), \quad (2.39)$$

which is the Fourier transformation of the position density matrix

$$\rho(\mathbf{r}, \mathbf{r}') = \int d\mu h(\mu) \psi_\mu(\mathbf{r}) \psi_\mu^*(\mathbf{r}'), \quad (2.40)$$

with $\int d\mu h(\mu) = 1$ and the two-point separation $\Delta = \mathbf{r} - \mathbf{r}'$.

Free Evolution

With a given wave function $\psi_0(\mathbf{r})$ at the $z = 0$ plane the free evolution of ψ up to the $z = L$ plane yields [59]

$$\psi_L(\mathbf{r}) = \frac{p_z}{2\pi\hbar i L} e^{\frac{ip_z L}{\hbar}} \int d\mathbf{r}_0 \exp\left(i\frac{p_z}{\hbar} \frac{|\mathbf{r} - \mathbf{r}_0|^2}{2L}\right) \psi_0(\mathbf{r}_0) + \mathcal{O}\left(\frac{\mathbf{r}^2}{L^2}\right), \quad (2.41)$$

and hence, following equation (2.40), the density matrix becomes

$$\rho(\mathbf{r}, \mathbf{r}') = \frac{p_z^2}{(2\pi\hbar)^2 L^2} \int d\mathbf{r}_0 d\mathbf{r}'_0 \exp\left(i\frac{p_z}{\hbar} \frac{|\mathbf{r} - \mathbf{r}_0|^2 - |\mathbf{r}' - \mathbf{r}'_0|^2}{2L}\right) \rho_0(\mathbf{r}_0, \mathbf{r}'_0). \quad (2.42)$$

Combining equations (2.39) and (2.42), it is found that upon free evolution of the Wigner function by a distance L it is changed to

$$w_L(\mathbf{r}, \mathbf{p}) = w_0\left(\mathbf{r} - \frac{L}{p_z} \mathbf{p}, \mathbf{p}\right). \quad (2.43)$$

Passage Through a Grating

Another step one has to consider to describe the interferometer is the transformation of the Wigner function for passing through a grating. As for the angular spectrum method in equation (2.14), a grating with its transmission function $g(\mathbf{r})$ with $|g(\mathbf{r})|^2 < 1$ results in a modification of the wave function $\psi(\mathbf{r})$:

$$\psi'(\mathbf{r}) = g(\mathbf{r})\psi(\mathbf{r}). \quad (2.44)$$

Inserting the modified wave function in the definition of the Wigner function (equation (2.39)) and the density matrix (equation (2.40)) yields the desired Wigner function after passing the

grating:

$$w'(\mathbf{r}, \mathbf{p}) = \int d\Delta e^{i\frac{\mathbf{p}\Delta}{\hbar}} g\left(\mathbf{r} - \frac{\Delta}{2}\right) g^*\left(\mathbf{r} - \frac{\Delta}{2}\right) \rho\left(\mathbf{r} - \frac{\Delta}{2}, \mathbf{r} + \frac{\Delta}{2}\right). \quad (2.45)$$

This expression can be rewritten as a convolution

$$w'(\mathbf{r}, \mathbf{p}) = \int d\mathbf{q} G(\mathbf{r}, \mathbf{q}) w(\mathbf{r}, \mathbf{p} - \mathbf{q}), \quad (2.46)$$

with the convolution kernel

$$G(\mathbf{r}, \mathbf{q}) = \frac{1}{(2\pi\hbar)^2} \int d\Delta e^{i\frac{\mathbf{p}\Delta}{\hbar}} g\left(\mathbf{r} - \frac{\Delta}{2}\right) g^*\left(\mathbf{r} - \frac{\Delta}{2}\right). \quad (2.47)$$

With the two transformations of the Wigner function, the free evolution in space (equation (2.43)) and the passage through a grating (equation (2.46)), one can now express the full Talbot-Lau setup in the Wigner representation.

2.5.2. Propagation Through the Talbot-Lau Setup

The Talbot-Lau Interferometer consists of three vertical gratings separated by a distance L_1 and L_2 . A monochromatic but uncollimated beam at the beginning of the setup can be expressed by a Wigner function of $w_0(\mathbf{r}, \mathbf{p}) = 1$. With equation (2.46) the Wigner function immediately after the first grating is

$$w_1(\mathbf{r}, \mathbf{p}) = |g_1(\mathbf{r})|^2. \quad (2.48)$$

And with the help of equation (2.43) the subsequent free evolution over the distance L_1 to the next grating yields

$$w_2(\mathbf{r}, \mathbf{p}) = w_1\left(\mathbf{r} - \frac{L_1}{p_z}\mathbf{p}, \mathbf{p}\right) = \left|g_1\left(\mathbf{r} - \frac{L_1}{p_z}\mathbf{p}\right)\right|^2. \quad (2.49)$$

Afterwards transmission through the second grating g_2 with its convolution kernel G_2 gives

$$w_3(\mathbf{r}, \mathbf{p}) = \int d\mathbf{q} G_2(\mathbf{r}, \mathbf{q}) w_2(\mathbf{r}, \mathbf{p} - \mathbf{q}) \quad (2.50)$$

$$= \int d\mathbf{q} \left|g_1\left(\mathbf{r} - \frac{L_1}{p_z}(\mathbf{p} - \mathbf{q})\right)\right|^2 \cdot G_2(\mathbf{r}, \mathbf{q}), \quad (2.51)$$

2. From Talbot-Lau Interferometry to Classical Moiré Deflectometer

while the free evolution up to the third grating leads to

$$w_4(\mathbf{r}, \mathbf{p}) = w_3\left(\mathbf{r} - \frac{L_2}{p_z}\mathbf{p}, \mathbf{p}\right) \quad (2.52)$$

$$= \int d\mathbf{q} \left| g_1\left(\mathbf{r} - \frac{L_2}{p_z}\mathbf{p} - \frac{L_1}{p_z}(\mathbf{p} - \mathbf{q})\right) \right|^2 \cdot G_2\left(\mathbf{r} - \frac{L_2}{p_z}\mathbf{p}, \mathbf{q}\right) \quad (2.53)$$

$$= \int d\mathbf{q} \left| g_1\left(\mathbf{r} - \frac{\mathbf{p}}{p_z}(L_1 + L_2) + \frac{\mathbf{q}}{p_z}L_1\right) \right|^2 \cdot G_2\left(\mathbf{r} - \frac{\mathbf{p}}{p_z}L_2, \mathbf{q}\right) . \quad (2.54)$$

The Wigner function $w_4(\mathbf{r}, \mathbf{p})$ represents the state of the beam in the plane of the third grating ($z = L_1 + L_2$). In order to obtain the particle density $w(\mathbf{r})$, which is the measurable observable in the experiment, the Wigner function has to be integrated over the momentum variable

$$w(\mathbf{r}) = \int d\mathbf{p} w_4(\mathbf{r}, \mathbf{p}) . \quad (2.55)$$

In the following the explicit grating functions for the interferometer in this work are considered to obtain the theoretical signal expected in this work.

2.5.3. Signal of the Talbot-Lau Interferometer with Pure Transmission Gratings

As previously mentioned, the Talbot-Lau interferometer operates in the near-field regime. Therefore, the finite lateral extension of the gratings does not affect the mathematical description of the interferometer. Hence the gratings can be described with a periodic function. Furthermore, as the experiment is invariant in the x -direction, it is sufficient to consider only the coordinates parallel to the grating vector, i.e. the position y , and the momentum p_y . As discussed for the angular spectrum method (chapter 2.2), a grating with the grating vector $k_d = 2\pi/d$ and a phase $\phi = 2\pi\Delta y/d$ can be expressed by its Fourier series (equation (2.9))

$$g_i(y) = \sum_{n \in \mathbb{Z}} a_n e^{ink_{d_i}y} , \quad (2.56)$$

with the Fourier coefficients (equation (2.13))

$$a_n = \eta \operatorname{sinc}(n\eta) e^{-ink_{d_i}\Delta y} =: a'_n e^{-ink_{d_i}\Delta y} . \quad (2.57)$$

For the second grating with period d_2 and open fraction η_2 we will use the Fourier coefficient b_n accordingly. With such grating function we get

$$|g_1(y)|^2 = \sum_{l \in \mathbb{Z}} A_l e^{ilk_{d_1}y} \quad \text{with} \quad A_l = \sum_{j \in \mathbb{Z}} a_j a_{j-l}^* \quad (2.58)$$

$$= \sum_{l \in \mathbb{Z}} A'_l e^{ilk_{d_1}(y+\Delta y_1)} \quad \text{with} \quad A'_l = \sum_{j \in \mathbb{Z}} a'_j a'_{j-l}{}^* \quad (2.59)$$

and

$$G_2(y, p) = \sum_{l, j \in \mathbb{Z}} b_j b_{j-l}^* \exp(ilk_{d_2} y) \delta\left(p - \hbar\pi \frac{2j-l}{d}\right) \quad (2.60)$$

$$= \sum_{l, j \in \mathbb{Z}} b'_j b'_{j-l}{}^* \exp(ilk_{d_2}(y + \Delta y_2)) \delta\left(p - \hbar\pi \frac{2j-l}{d}\right). \quad (2.61)$$

With these two expressions the integral in equation (2.54) for the Wigner function $w_4(y, p)$ in the plane of the third grating can be evaluated. For simplicity, the gratings are assumed to have identical period $d = d_1 = d_2$ and open fraction $\eta = \eta_1 = \eta_2$, and are taken to be equidistant, i.e. $L = L_1 = L_2$. The state (2.54) thus becomes

$$w_4(y, p) = \sum_{l, j, m \in \mathbb{Z}} A_l b_m b_{m-j}^* \exp\left(ik_d(l+j)y - ik_d(2l+j)\frac{p}{p_z}L\right). \quad (2.62)$$

$$\exp\left(i\pi l(2m-j)\frac{L}{L_T}\right). \quad (2.63)$$

Here the Talbot length

$$L_T = \frac{d^2}{\lambda} = \frac{d^2 p_z}{2\pi \hbar} \quad (2.64)$$

is introduced. Following equation (2.55) the density modulation, which is detectable with a spatially resolving detector, yields

$$w(y) = \int dp w_4(y, p) \quad (2.65)$$

$$\propto \sum_{l \in \mathbb{Z}} A_l B_{2l}^{(T)} \exp(ik_d l y), \quad (2.66)$$

with the Fourier components

$$B_j^{(T)} = \sum_{m \in \mathbb{Z}} b_m b_{m-j}^* \exp\left(i\pi \frac{j^2 - 2mj}{2} \frac{L}{L_T}\right). \quad (2.67)$$

The result in equation (2.66) predicts a pattern with the same period d as the gratings. The coefficients $B_j^{(T)}$ account for the second grating¹. Considering the phase of the second grating $\phi = 2\pi\Delta y_2/d$, one gets for the coefficients

$$B_{2l}^{(T)} = B'_{2l}{}^{(T)} \exp(-ik_d l 2\Delta y_2), \quad (2.68)$$

¹The Fourier components $B_j^{(T)}$ are marked with a T to distinguish them from the classical case with the Fourier components $B_j^{(C)}$ introduced later.

2. From Talbot-Lau Interferometry to Classical Moiré Deflectometer

which indicates that a vertical shift of the second grating of Δy_2 results in twice the vertical displacement on the observed pattern. In contrast, a shift Δy_1 of the first grating (equation (2.59)), causes a one to one shift on the observable pattern but in the opposite direction.

As discussed in chapter 2.4 a third grating with the same period d as the other two gratings helps to resolve the pattern if it is scanned over its vertical position y_s . The signal then yields

$$S_T(y_s) = \int dy w(y) |g_3(y - y_s)|^2. \quad (2.69)$$

With the same notation, Fourier coefficients for the third grating are denoted with C_l with its position Δy_3 . The final signal for the full three-grating Talbot-Lau interferometer leads to

$$S_T(\Delta y_1, \Delta y_2, \Delta y_3) \propto \sum_{l \in \mathbb{Z}} A_l B_{2l}^{(T)} C_l \quad (2.70)$$

$$= \sum_{l \in \mathbb{Z}} A_l' B_{2l}'^{(T)} C_l' \exp(ik_{dl}(\Delta y_1 - 2\Delta y_2 + \Delta y_3)) \quad (2.71)$$

$$= \sum_{l \in \mathbb{Z}} (A_l')^2 B_{2l}'^{(T)} \exp(ik_{dl}(\Delta y_1 - 2\Delta y_2 + \Delta y_3)). \quad (2.72)$$

In the last steps we extracted the position such that the coefficients for the first and last grating would be identical ($A_l' = C_l'$). The visibility (compare equation (2.5)) can be derived from the upper equation. Maximum signal is obtained if the three gratings are aligned and hence the phase is $\Delta y = \Delta y_1 - 2\Delta y_2 + \Delta y_3 = 0$, while minimal signal is attained if the last grating is shifted by half a period and hence $\Delta y = d/2$. The visibility therefore yields

$$\nu_T = \frac{S_{\max} - S_{\min}}{S_{\max} + S_{\min}} \quad (2.73)$$

$$= \frac{\sum_{l \in \mathbb{Z}} \left((A_l')^2 B_{2l}'^{(T)} - (A_l')^2 B_{2l}'^{(T)} e^{i\pi l} \right)}{\sum_{l \in \mathbb{Z}} \left((A_l')^2 B_{2l}'^{(T)} + (A_l')^2 B_{2l}'^{(T)} e^{i\pi l} \right)} \quad (2.74)$$

$$= \frac{\sum_{n=1}^{\infty} (A_{2n-1}')^2 B_{4n-2}'^{(T)}}{\frac{1}{2}(A_0')^2 B_0'^{(T)} + \sum_{n=1}^{\infty} (A_{2n}')^2 B_{4n}'^{(T)}}. \quad (2.75)$$

This equation enables directly to calculate the visibility of the pattern for a Talbot-Lau interferometer with a given grating separation L , grating pitch d and grating open fraction η for a particle beam with a wavelength λ . Hence, we use this formula to produce visibility plots such as that in figure 2.1. In order to make use of this equation, we truncate the series after 100 iterations.

2.6. The Classical Limit: Moiré Deflectometer

So far we have given a full quantum mechanical description of the Talbot-Lau interferometer with its underlying principle and characteristics. In general, one can argue that this full description inherently includes the classical case, the moiré deflectometer, a priori. To retrieve the visibility of the moiré deflectometer one has to follow equation (2.4) and set the wavelength λ to a sufficiently small value, so that for the given setup the Talbot length L_T is large compared to the grating distance L , i.e. $L_T \gg L$. However, with classical trajectories the key feature of the classical moiré deflectometer gets more intuitive. General features such as the pattern deflection due to an external force or the requirements of the grating alignments, as discussed in the next chapter (chapter 3), can be illustrated in a more intuitive way in the classical scenario, while still holding in the quantum case.

In the following, we first provide a general exposition of the moiré deflectometer with simple geometric trajectories. Secondly we conclude with a classical phase-space representation of the three-grating setup. This enables us to compare the Talbot-Lau in Wigner representation with its classical limit in section 2.7.

2.6.1. Pattern Formation with Geometrical Trajectories

Similarly to the Talbot-Lau interferometer, the moiré deflectometer consists of three identical transmission gratings which are aligned parallel and equidistant to each other [38]. Furthermore, and still similarly to the interferometer, particles of a non-collimated source pass through the first and second grating and create a fringe pattern with the periodicity of the gratings in the plane of the third grating. Here the first two gratings can be seen as a collimator. The shadow image of the gratings which is created in the plane of the third grating can be understood merely with the possible geometrical trajectories (compare figure 2.6(a)). From this picture it becomes clear that in contrast to the Talbot-Lau interferometer, the chosen distance L plays no role in the pattern of the moiré deflectometer as long as the three gratings are equidistant. The reason is that all possible trajectories are defined by two arbitrary slit positions $y_1 = nd$ and $y_2 = md$ ($n, m \in \mathbb{Z}$) in the plane of the first and second grating. For the position at the third grating this results in $y_3 = (2m - n)d$, which is independent of L and resembles the grating function with period d .

With a finite slit width b and hence an open fraction of $\eta = b/d$ more particle trajectories are possible, resulting in the pattern smearing out (compare figure 2.6(b)). This is equivalent to the aforementioned selection of different Talbot carpets. Therefore for open fractions below $\eta = 50\%$ it holds that the smaller the open fraction, the higher the fringe contrast (figure 2.6(c)). As for the Talbot-Lau setup, a third grating in the moiré deflectometer also magnifies the fine periodic structure by means of the moiré effect.

2. From Talbot-Lau Interferometry to Classical Moiré Deflectometer

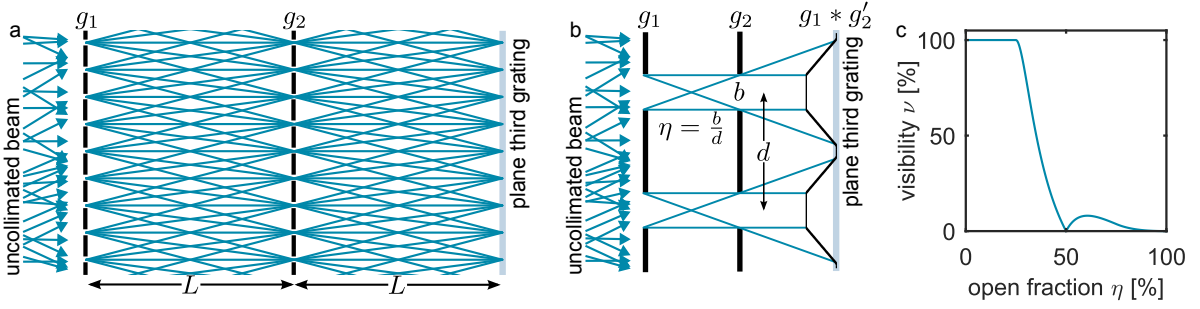


Figure 2.6.: Principle of the classical moiré deflectometer. (a) An uncollimated beam passing through two gratings forms a shadow image of the gratings in the plane of the third grating. (b) A close-up to show the effect of a finite slit width b with open fraction $\eta = b/d$. A multiple of additional trajectories are possible which smear out the pattern and therefore reduce visibility. (c) The visibility of the macroscopic pattern formed by the third grating as a function of the grating's open fraction.

If we consider the two grating functions $g_1(y, \eta, d)$ and $g_2(y, \eta, d)$, for the first two gratings as introduced in equation (2.8) an analytical expression for the fringe pattern can be retrieved from geometrical considerations [47, 48]. The pattern I_{nano} is mathematically a convolution of the two transmission functions

$$I_{\text{nano}}(y) = g_1(y, \eta, d) * g_2(y, \eta, d') \quad (2.76)$$

$$= \int d\tau g_1(\tau, \eta, d) g_2(\tau - y, \eta, d'), \quad (2.77)$$

whereby the periodicity for g_2 has to be changed according to

$$d' = d \frac{L_1 + L_2}{L_2} = 2d. \quad (2.78)$$

In the last step we assumed the gratings to be equidistant ($L = L_1 = L_2$). Following equation (2.38) the third grating is another convolution of the nanoscopic intensity pattern with the grating function of the third grating. If we use the Fourier series to express the gratings (equation (2.9)) the following expression for the macroscopic moiré pattern can be found [45]

$$I_{\text{moiré}}(y) = \frac{a_0}{2} + \sum_{n=0}^{\infty} a_n \cos(2\pi n y / d) \quad (2.79)$$

$$a_n = 4\eta^3 \frac{\sin(\pi\eta n)^3}{(\pi\eta n)^3} \cos(\pi\eta n). \quad (2.80)$$

Here we used that all gratings are identical and equidistant. It can be seen and also understood with the geometrical trajectories that the fringe pattern does not depend on the de Broglie wavelength or the particle's energy, respectively. This analytic approach helps calculate the visibility for different configurations, as shown in figure 2.6(c). Furthermore, it requires less

computational effort than the quantum description to study the alignment requirements, such as the precision of the grating pitch and small variations in the rotational and horizontal alignment. This is explained in chapter 3.1 where these alignment requirements are studied as a function of divergence α of the incident particle beam².

2.6.2. Classical Phase-Space Representation

Analogous to the Talbot-Lau interferometer in Wigner representation, the moiré deflectometer can be calculated using classical phase-space dynamics [59]. The classical phase-space density $f(\mathbf{r}, \mathbf{p})$ replaces the Wigner function, while the transform under free evolution is just as for the Wigner function (2.43) given by

$$f(\mathbf{r}, \mathbf{p}) = f_0 \left(\mathbf{r} - \frac{L}{p_z} \mathbf{p}, \mathbf{p} \right) . \quad (2.81)$$

The main difference is the convolution kernel for passing through a grating, which is now given by

$$G_C(\mathbf{r}, \mathbf{p}) = \frac{1}{(2\pi\hbar)^2} \int d\Delta e^{\frac{i\mathbf{p}\Delta}{\hbar}} |g(\mathbf{r})|^2 = |g(\mathbf{r})|^2 \delta(\mathbf{p}) . \quad (2.82)$$

With equation (2.46) the passage through a grating leads to

$$f'(\mathbf{r}, \mathbf{p}) = |g(\mathbf{r})|^2 f(\mathbf{r}, \mathbf{p}) . \quad (2.83)$$

For the full passage through the two gratings the phase-space distribution in the plane of the third grating yields

$$f_4(\mathbf{r}, \mathbf{p}) = \left| g_1 \left(\mathbf{r} - \frac{\mathbf{p}}{p_z} 2L \right) \right|^2 \left| g_2 \left(\mathbf{r} - \frac{\mathbf{p}}{p_z} L \right) \right|^2 . \quad (2.84)$$

The very same result can also be obtained from the quantum case in equation (2.54) by replacing the convolution kernel of the second grating G_2 with G_C . For the classical density pattern in the observational plane it follows

$$f(y) = \int dp f(y, p) \propto \sum_{l \in \mathbb{Z}} A_l^* B_{2l}^{(C)} \exp \left(2\pi i l \frac{y}{d} \right) , \quad (2.85)$$

with

$$B_m^{(C)} = \sum_{j \in \mathbb{Z}} b_j b_{j-m}^* . \quad (2.86)$$

²Note, to consider the beam's divergence, the integral in equation (2.77) has to be restricted to the limits of $y \pm 2L \tan(\alpha)$.

2. From Talbot-Lau Interferometry to Classical Moiré Deflectometer

Comparing the classical density pattern with the quantum result (equation (2.66)) reveals that they have the same form but differ in B_m . $B_m^{(C)}$ can be interpreted as the classical limit $L/L_T \rightarrow 0$ of $B_m^{(T)}$, which is also indicated by the notation. As this is the only difference between the quantum and the classical descriptions the analytic form of the signal and visibility in the classical case is obtained from equation (2.72) and (2.75) by replacing the Fourier components $B_m^{(T)}$ of the second grating in the quantum case by their classical equivalent $B_m^{(C)}$:

$$S_C(\Delta y_1, \Delta y_2, \Delta y_3) \propto \sum_{l \in \mathbb{Z}} (A'_l)^2 B_{2l}^{\prime(C)} \exp(ik_d l (\Delta y_1 - 2\Delta y_2 + \Delta y_3)) \quad (2.87)$$

$$\nu_C = \frac{\sum_{n=1}^{\infty} (A'_{2n-1})^2 B_{4n-2}^{\prime(C)}}{\frac{1}{2}(A'_0)^2 B_0^{\prime(C)} + \sum_{n=1}^{\infty} (A'_{2n})^2 B_{4n}^{\prime(C)}} . \quad (2.88)$$

2.7. From Quantum Description to Classical Trajectories

The previous sections gave a full analytic description of the Talbot-Lau interferometer and its classical counterpart the moiré deflectometer. We noticed that the retrieved signals S_T and S_C show a strong similitude, with the only difference being the Fourier coefficients of the second grating $B_l^{(T)}$ and $B_l^{(C)}$. This shows that for the interferometer diffraction only plays a role at the second grating, while the first and last grating generate the spatial coherence or read out the pattern, respectively. The difference of the two Fourier components lies solely in an additional phase factor

$$B_{2l}^{(T)} = B_{2l}^{\prime(C)} \cdot \exp\left(2\pi i (l^2 - jl) \frac{L}{L_T}\right) . \quad (2.89)$$

From this connection two artefacts become clear:

1) For the short-wavelength limit, which is the classical limit, the grating separation L becomes much smaller than the Talbot length $L_T = d^2/\lambda$, and therefore the phase factor vanishes. Consequently, it is justified to see the moiré deflectometer as the classical limit of the Talbot-Lau interferometer. This fact confirms that the Talbot length is the characteristic measure which separates the various regimes. Thus, for

$$L \ll L_T , \quad (2.90)$$

the device approaches its classical limit as predicted in equation (2.4).

2) The main characteristic feature of the Talbot-Lau interferometer is that the phase factor vanishes if the grating separation L equals a multiple integer of the Talbot length, i.e.

$$L = nL_T \quad \text{with} \quad n \in \mathbb{Z} . \quad (2.91)$$

At such positions the peculiar self-images of the grating appear. As the Fourier components $B_l^{(T)}$ and $B_l^{(C)}$ become equal, the Talbot-Lau interferometer is indistinguishable in these configurations from the classical moiré deflectometer. Therefore, to show that the particle exhibits wave nature one has to tune the de Broglie wavelength such, that the Talbot length does not match an integer multiple of the grating distance L in the interferometer. While the fringe pattern and hence the visibility remains constant for different wavelength in the classical case it changes significantly in the quantum regime.

2.8. Summary

This chapter aimed to give a detailed review on the Talbot-Lau interferometer and its classical limit the moiré deflectometer. Full analytical expressions were presented for the visibility – a key feature in the measurements – which enable to distinguish the classical and the wave behaviour of the particle. The Talbot length was introduced as a characteristic measure to define the classical limit of the interferometer. Therefore, it was shown that the same setup can be described in classical terms if the de Broglie wavelength is much larger than the square of the gratings period d over the grating distance L :

$$\lambda \ll \frac{d^2}{L} . \quad (2.92)$$

The presented analytic approaches provide us with powerful tools to study crucial parameters which alter the visibility. Therefore, the next chapter goes into detail on the main effects which can result in a significant visibility reduction, like the alignment of the three gratings or forces acting on the particles passing through the interferometer.

3. Visibility-Affecting Factors

The previous chapter provided powerful tools to calculate the fringe shape and visibility for an arbitrary Talbot-Lau or moiré setup. However, their performance is sensitive to numerous perturbations, such as misalignments of the three gratings or vibrations. Furthermore the interferometer exhibits a high susceptibility to forces which may alter the path of a particle propagating through the interferometer. This can result in decoherence effects or in a deflection of the interferometric pattern, resulting in variation of the detected visibility. Thereby, one has to consider overall offset fields the interferometer is exposed to, such as the gravitational field, the Earth's magnetic fields and any electric fields, as well as interactions inside the grating slits, for instance van der Waals or dipole interactions.

It is the topic of this chapter to discuss the different visibility-affecting factors and to provide limits on them which must be met in order for the Talbot-Lau interferometer and its classical equivalent the moiré deflectometer to operate successfully.

3.1. Alignment Requirements of the Three-Grating Setup

The Talbot-Lau interferometer and the moiré deflectometer were introduced in the previous chapter in their ideal form. This implies that all gratings have the same periodicity and are equidistantly placed, while the planes of the gratings as well as the grating slits are parallel. However, there are experimental limitations on the extent to which, for example, two gratings can be placed equidistantly or parallelly with respect to each other.

This section provides a detailed understanding of the different parameters with respect to their required precision and shows how the visibility decreases if the requirements are not met. The individual parameters are discussed separately to give in the end a quantitative measure of how much a particular parameter can be varied from its ideal value before the visibility of the observed fringes drops to zero. For the sake of clarity, all relations are summarised in table 3.1 at the end of this section.

Various approaches exist to derive and explain the limits on the different parameters, starting from rigorous treatments with the Wigner formalism [58], over semi-classical approaches [61, 62] up to classical explanations [47]. The approach presented in the following aims to give an intuitive access how a small misalignment affects the visibility. Classical pictures are used in the process to illustrate the criticality of the different parameters. Furthermore, the detailed visibility evolution over the different parameters is calculated with the approach

3. Visibility-Affecting Factors

presented in chapter 2.6.1.

The classical results derived and presented in this section were verified by Demetrio [47] for the general quantum case using the angular spectrum method and published collectively in [53].

3.1.1. Longitudinal Position of the Gratings

The Talbot-Lau interferometer and the moiré deflectometer are based on the re-phasing or re-focussing effect of the particle waves or the trajectories in the plane of the third grating (compare chapter 2). Small deviations in the longitudinal position of the gratings can therefore reduce the visibility of the resulting fringe pattern.

To assess this effect, we start with the classical picture in figure 3.1(a). A particle beam with divergence¹ θ forms a shadow image after the two gratings. The position of this image is a distance L after the second grating, while L denotes the distance between the first and second grating. A small misplacement by ΔL results in a blur D of the shadow image, given by

$$D = 2\Delta L \tan(\theta) . \quad (3.1)$$

If the blur equals one grating period, i.e. $D = d$, the periodic pattern vanishes. This defines the critical misplacement of the last grating where no fringe pattern can be found

$$\Delta L_{\text{crit}} = \frac{d}{2} \tan\left(\frac{\pi}{2} - \theta\right) . \quad (3.2)$$

Figure 3.1(b) gives the full evolution of the visibility retrieved with the formalism presented in chapter 2.6.1. The visibility evolution resembles the absolute values of a *sinus cardinalis* whose first zero crossing equals the critical displacement ΔL_{crit} . Note that besides the grating period d the visibility depends only on the divergence θ . For a decreasing θ , i.e. for a more collimated beam, the longitudinal grating position becomes less critical. For example, for $\theta = 1$ mrad, the pattern vanishes at $\Delta L_{\text{crit}} = 128 \mu\text{m}$, whereas for a better collimated beam with $\theta = 0.5$ mrad the pattern is washed out only at $\Delta L_{\text{crit}} = 257 \mu\text{m}$.

3.1.2. Grating Pitch

The transmission gratings in this work were photo-lithographically etched into a silicon nitride membrane². Therefore, it is important to discuss the precision of the grating pitch and the deviations in the gratings' period with respect to each other.

In order to shed light on this question, figure 3.2(a) gives a simple intuition with trajectories of classical particles. If the second grating exhibits a periodic difference of Δd with respect to the first one, a well-collimated beam will form a periodic pattern with $d' = d + 2\Delta d$ in the plane of the third grating (red trajectories). In case of a diffuse beam with divergence θ

¹We define the divergence θ of a beam as the maximum angle particle trajectories have with respect to the beam axis (compare figure 3.1(a)).

²More details on the gratings are given in chapter 4.2.1.

3.1. Alignment Requirements of the Three-Grating Setup

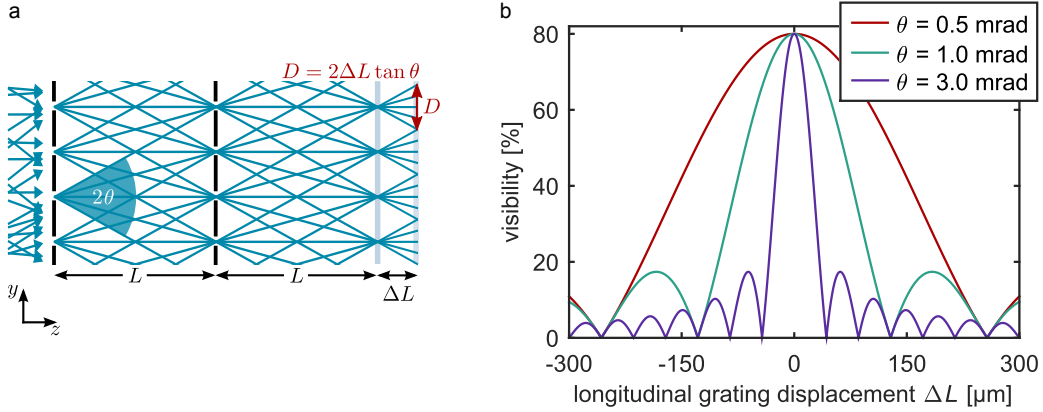


Figure 3.1.: Effect of a longitudinal misalignment of the three gratings. The third grating is not placed equidistantly with respect to the second one, but is subject to a displacement ΔL . (a) Classical picture of the effect of a longitudinal displacement of the last grating. The grating's shadow image is formed in the plane which is equidistant to the second grating. A misplacement by ΔL results in a blur D of the shadow image which is dependent on the initial divergence of the beam θ . If the blur equals one grating period $D = d$, a periodic pattern cannot be identified anymore. This defines the critical misplacement with $\Delta L_{\text{crit}} = d/2 \tan(0.5\pi - \theta)$. (b) Calculated visibility over the longitudinal grating displacement ΔL for different beam divergence angles θ . The visibility drops from the initial 80% to zero if the displacement equals the critical distance ΔL_{crit} . The larger the beam divergence, the more sensitive is the visibility to the displacement.

one can interpret each grating slit of the first grating as a point source which projects the second grating on the third one. In conflict with the collimated beam, this pattern exhibits a slightly different periodicity with $d'' = d + \Delta d$ that washes out the fundamental pattern. If the extension of the projected pattern due to the divergence angle θ causes a mismatch of the two patterns by half a period, no pattern can be identified in the plane of the third grating. Similarly as for the longitudinal misalignment, this defines a critical parameter for the difference of the first two gratings, given by

$$\Delta d_{\text{crit}} = \frac{d^2}{4L\theta} . \quad (3.3)$$

The graph in figure 3.2(b) shows the more detailed visibility evolution for a small difference in the periodicities of grating one and two. Pictured is the evolution for three different divergence angles θ . The visibility drops rapidly to zero if the difference Δd equals the critical values Δd_{crit} . For example, the visibility drops to zero for a beam with $\theta = 1$ mrad if the pitches have a difference of $\Delta d_{\text{crit}} = 118$ pm. This is a mismatch of less than 0.5‰ and corresponds to, for example, the size of a single hydrogen atom.

The visibility evolution for a small mismatch of the grating pitches shows a considerable similarity to the visibility evolution of the longitudinal misplacement (compare figures 3.1(b) and 3.2(b)). This artefact indicates a deeper relation of these two parameters. Indeed, following the schematic in figure 3.2(a), particles passing two slightly different gratings also have a

3. Visibility-Affecting Factors

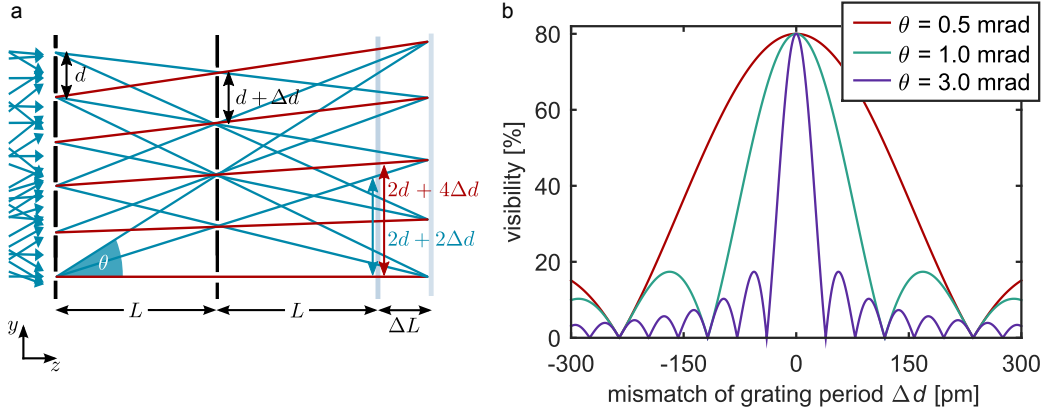


Figure 3.2.: Influence of a small difference Δd on the grating pitches. (a) Classical picture to explain the visibility reduction if the second grating exhibits a periodic difference of Δd with respect to the first one. Red trajectories indicate the pattern formation for a well-collimated beam in the plane of the third grating. A grating image is formed with a periodicity of $d + 2\Delta d$. In case of a diffuse beam (turquoise trajectories) this pattern is overlapped with a projection of the second grating onto the third one. This results in a periodic pattern of $2(d + \Delta d)$ which blurs out the above-mentioned pattern. If the extension of the projected pattern due to the divergence θ causes a mismatch of the two patterns by half a period d , the pattern vanishes completely. This defines a critical parameter $\Delta d_{\text{crit}} = d^2/4L\theta$. The effect of a mismatch in the periodicity can be compensated for by altering the distance between the second and third grating. The refocusing plane for two slightly different gratings is shifted by $\Delta L = 2L(\Delta d/a)$. (b) Calculated visibility over a small difference in the grating pitch. The visibility drops to zero if the difference in period equals the critical value of Δd_{crit} .

refocusing plane. This plane does not overlap with the ideal plane, which is equidistant with respect to the first two gratings, but is shifted by a small displacement

$$\Delta L(\Delta d) \approx 2L \frac{\Delta d}{d} . \quad (3.4)$$

This relation clarifies the similarity of the visibility behaviour and verifies the relation of the critical difference Δd_{crit} in equation (3.3) using the expression for ΔL_{crit} in equation (3.2)³. Furthermore, it indicates that a difference in the grating pitch can be compensated with the longitudinal position of the last grating following equation 3.4. It therefore yields a more general constraint for the precision of the longitudinal grating position and the pitch precision which is

$$\frac{\Delta L}{L} - 2\frac{\Delta d}{d} \ll \frac{d}{2\theta L} . \quad (3.5)$$

Note that the nanoscopic pattern in the new refocusing plane has a periodicity of $d' \approx d + 2\Delta d$. As described in chapter 2.4 a third grating is used to scan or magnify the fringe pattern. If the last grating also exhibits a small difference $\Delta d'$ in periodicity, with respect to the

3.1. Alignment Requirements of the Three-Grating Setup

nanoscopic pattern d' , a macroscopic moiré pattern with a period of $D_{\text{moiré}} \approx d^2/\Delta d'$ can be observed. Anyhow this gives a more rigorous limit if the last grating is used to scan the pattern. Therefore the size of the particle beam H has to be smaller than half the macroscopic moiré pattern to enable the scanning principle. The critical difference hence yield

$$\Delta d_{\text{crit}_s} = \frac{d^2}{4H}, \quad (3.6)$$

for scanning the third grating⁴. For $H = 3 \text{ mm}$, which is the size of the grating used in this work, the critical pitch difference is $\Delta d_{\text{crit}_s} = 22 \text{ pm}$.

3.1.3. Rotational Alignment

For the sake of simplicity the three-grating setup was solely considered in the y - z -plane. This treatment was sufficient, as the first two gratings were considered to be parallel, resulting in a translational symmetry in the x -direction. Nevertheless, with a small rotational misalignment $\Delta\alpha = \alpha_1 - \alpha_2$ between the first two gratings, this approach is no longer valid. Extending the analytic treatment introduced in chapter 2.6.1 into two dimensions [47] leads to distinct visibility minima, as can also be seen in figure 3.3(b).

A rough idea of the critical rotational misalignment can be given if one treats the effect separately in the y - z -plane and the x - z -plane. To do this, we introduce the divergence angles θ_y and θ_x which give the divergence in the respective planes. A rotation of the second grating with respect to the first one increases the effective period of the grating according to

$$d' = \frac{d}{\cos(\Delta\alpha)} \approx d + d \frac{\Delta\alpha^2}{2} + \mathcal{O}(\Delta\alpha^4). \quad (3.7)$$

Using the critical difference in the grating pitch (equation (3.3)) the rotational misalignment is therefore not allowed to exceed

$$\Delta\alpha_{\text{crit},y} = \sqrt{\frac{d}{2L\theta_y}}. \quad (3.8)$$

To consider the effect a divergence beam has in the x - z -plane, it can be noticed, that the nanoscopic pattern in the plane of the third grating rotates twice the rotational misalignment angle, i.e. $2\Delta\alpha$. This can be directly seen following the argument that a phase shift of the second grating results a shift of the nanoscopic pattern twice as large (compare equation (2.72)). In the x -direction this results in a periodic pattern in the plane of the third grating with $D \approx d/\Delta\alpha$. With a divergence beam θ_x the pattern has to vanish if a particle coming from a horizontal slit in the first grating covers more than half of the horizontal beating in the plane of the third grating, i.e. if $\theta_x \approx D/4L$. This yields a critical limit for the rotation angle of

$$\Delta\alpha_{\text{crit},x} = \frac{d}{4L\theta_x}. \quad (3.9)$$

⁴The subscript s accounts for the idea that the last grating is used to scan the nanoscopic pattern.

3. Visibility-Affecting Factors

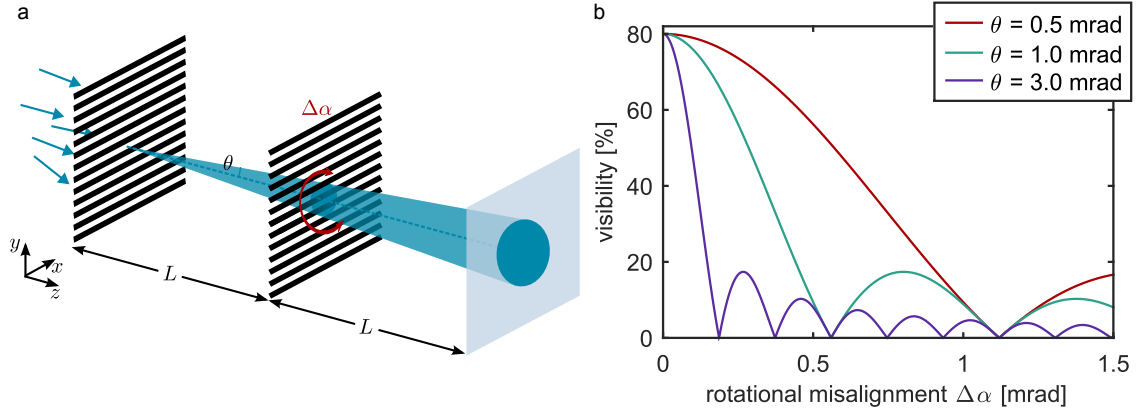


Figure 3.3.: Rotational misalignment $\Delta\alpha$ between the first two gratings. (a) The classical two-dimensional description has to be extended in the x -direction to account for a rotation of the second grating. Therefore the divergence angle θ describes the half opening of a cone which defines the maximum angle particle trajectories have with respect to the beam axis. (b) Calculated visibility for two non-parallel gratings. The critical angle, where the visibility equals zero, is $\Delta\alpha_{\text{crit}} = k(d/4L\theta)$, with a correction factor $k = 1.22$.

For the special case that the divergence of the beam in both directions is equal, i.e. $\theta_x = \theta_y$, one can follow the analytic treatment in [47] which is the three-dimensional extension of the approach presented in chapter 2.6.1. Analogous to the two-dimensional case, the divergence θ is defined as the maximum angle particle trajectories will experience with respect to the beam axis. This is equivalent to a half of the opening of a cone, just as pictured in figure 3.3(a). The graph in figure 3.3(b) shows the visibility behaviour if the rotational misalignment is considered in the full three-dimensional description. Similarly to the other critical parameters the visibility shows a sharper drop off if the divergence angle is increased. Performing the calculation for several configurations of d , L and θ , one numerically finds an expression of the first visibility minimum, that defines the critical rotational misalignment up to

$$\Delta\alpha_{\text{crit}} = k \frac{d}{4L\theta} . \quad (3.10)$$

A proportionality factor k has to be considered which reflects the definition of the divergence angle θ . For the mentioned cone which fulfills the relation $\theta \leq \sqrt{\theta_x^2 + \theta_y^2}$, one finds $k = 1.22 \pm 0.02$ [53]. The analytic treatment therefore confirms the simple assumptions in equation (3.9), which is only modified by the small correction factor k . For a beam with $\theta = 10$ mrad, this would mean a critical value of $\Delta\alpha_{\text{crit}} = 0.56$ mrad.

As mentioned before, a rotation of the second grating with respect to the first one results in twice the rotation of the nanoscopic pattern in the plane of the third grating. Furthermore, this pattern has a small reduction in periodicity according to $d' = d \cos(2\Delta\alpha)$. Similarly to the critical difference in the grating pitch, this defines a more restricted limit if the last grating is to be used to scan the pattern instead of magnifying it. With the given size of the

3.1. Alignment Requirements of the Three-Grating Setup

particle beam H , this results in a critical rotational difference of

$$\Delta\alpha_{\text{crit}_s} = \sqrt{\frac{d}{4H}} , \quad (3.11)$$

which would yield $\Delta\alpha_{\text{crit}_s} = 4.6$ mrad if the beam exposed the full size of the gratings with $H = 3$ mm.

3.1.4. Tilt Angle

The last parameter to consider is the tilt angle, which describes the parallelism of the grating planes with respect to each other. To discuss the effect the tilt around the x -axis, β_x , is separated from a tilt around the y -axis, β_y . In the following the effect of a tilt is explained with the help of a change in the second grating. The retrieved relations hold for any tilt of each grating. Furthermore, the effect of a tilt around the x - or y -axis can also be derived using the discussed expressions for the critical longitudinal misalignment and the critical difference in the gratings' period.

A tilt around the x -axis, as well as around the y -axis, leads to a variance of the distance between the gratings over the whole grating size H , according to

$$\Delta L(\beta_{x,y}) \approx H\beta_{x,y} . \quad (3.12)$$

With the definition of the critical longitudinal misalignment (equation (3.2)), one finds an expression for the maximum tilt

$$\Delta\beta_{x,y;\text{crit};L} = \frac{d}{2H \tan(\theta)} , \quad (3.13)$$

for which the nanoscopic fringe pattern fades towards the grating edge.

The tilt around the x -axis exhibits an additional effect which alters the visibility. A small angle β_x changes the effective grating period according to

$$d' = d \cos(\beta_x) \approx d - d \frac{\beta_x^2}{2} + \mathcal{O}(\beta_x^4) , \quad (3.14)$$

and hence yields a difference in the grating pitch with respect to the non-tilted first grating of

$$\Delta d \approx d \frac{\beta_x^2}{2} . \quad (3.15)$$

With equation (3.3) this defines the critical tilt around the x -axis with respect to a change in period with

$$\Delta\beta_{x;\text{crit};d} = \sqrt{\frac{d}{2L\theta}} . \quad (3.16)$$

3. Visibility-Affecting Factors

For the setup in this work, i.e. for $H = 3$ mm and a beam divergence $\theta = 1$ mrad, the critical parameters yield

$$\Delta\beta_{x,y; \text{crit};L} = 43 \text{ mrad} \quad (3.17)$$

$$\Delta\beta_{x; \text{crit};d} = 30 \text{ mrad} . \quad (3.18)$$

Here the critical value $\Delta\beta_x$ due to the change in the effective grating period is more stringent compared to the effect of the change in the distance L . Therefore one has to consider always the more demanding limit. The limits for the two different tilts can be expressed as following

$$\Delta\beta_x = \min \left\{ \sqrt{\frac{d}{2L\theta}}; \frac{d}{2H \tan(\theta)} \right\} , \quad (3.19)$$

$$\Delta\beta_y = \frac{d}{2H \tan(\theta)} . \quad (3.20)$$

critical parameter		formula	$\theta = 1$ mrad
Longitudinal Alignment	ΔL	$\frac{d}{2\theta}$	128 μm
Grating Pitch	Δd	$\frac{d^2}{4L\theta}$	118 pm
Rotational Alignment	$\Delta\alpha$	$\frac{1.2d}{4L\theta}$	0.56 mrad
Tilt Angle	$\Delta\beta_x$	$\min \left\{ \sqrt{\frac{d}{2L\theta}}; \frac{d}{2H \tan(\theta)} \right\}$	30 mrad
	$\Delta\beta_y$	$\frac{d}{2H \tan(\theta)}$	43 mrad

Table 3.1.: Critical alignment parameters and their analytic expression for which the fringe visibility of the nanoscopic pattern drops to zero. Only those relations are considered which allow the read-out of the nanoscopic pattern with a third grating using the moiré effect. The last column gives the critical parameters for the three-grating setup used in this work with a beam divergence of $\theta = 1$ mrad. (Specifications of the three-grating setup: $L = 14$ cm, $d = 257$ nm, $H = 3$ mm.)

3.2. Vibrations of the Three-Grating Setup

The previous sub-chapter discussed critical motions of different parameters in the three-grating setup which can alter the fringe visibility. Besides the precise alignment of the different gratings with respect to each other, drifts and vibrations may also affect the pattern's shape. While drifts can be avoided using short data-acquisition times and keeping the ambient temperature constant⁵, vibrational perturbations may play a crucial role if the particles' inverse time of flight is in the order of the oscillation frequencies, or if different parts of the experimental setup oscillate independently. Following the listed critical parameters in table 3.1, it becomes clear that those parameters are not relevant for considering vibrational perturbations. For example, the gratings would have to oscillate horizontally with amplitudes in the range of 100 μm to surpass the critical longitudinal alignment ΔL_{crit} . Such immense oscillations are extremely unlikely to appear. Resonance frequency measurements of the single fine-precision actuators used to align the gratings reveal resonances in the range of 200 Hz up to 25 000 Hz dependent on their load, with amplitudes around few tens of nanometres [63]. These frequencies from the acoustic regime in fact dominate the vibrational spectrum for example due to the vacuum turbo-molecular pumps or the chiller, while such small oscillation amplitudes may have a detrimental effect if they appear along the grating vector.

Therefore, in the following we focus on vertical oscillations. Thereby we can consider the full setup to carry out a simple harmonic oscillation, or the three gratings to vibrate independently. We will see that a fixed harmonic oscillation can be neglected in this work, while independent grating oscillations may have a non-negligible impact on the visibility.

The subsequent derivations follow considerations made for heavy and slow molecular interferometers [64–66].

3.2.1. Fixed Harmonic Oscillation

The basic oscillation which affects the fringe visibility is a common vertical motion of the entire three-grating setup along the grating vector with

$$\Delta y = A \sin(2\pi ft) , \quad (3.21)$$

where A denotes the oscillation amplitude, f the frequency and t the time. Following equation (2.72), particles which enter the setup with the initial phase position φ_0 of the gratings will cause a fringe shift of

$$\Delta y = \Delta y_1 - 2\Delta y_2 + \Delta y_3 \quad (3.22)$$

$$= A \left[\sin(\varphi_0) - 2 \sin\left(\varphi_0 + 2\pi f \frac{L}{v_z}\right) + \sin\left(\varphi_0 + 2\pi f \frac{L}{v_z}\right) \right] . \quad (3.23)$$

Using the angle addition and subtraction theorems the shift can be further simplified to

$$\Delta y(\varphi_0) = -4A \sin^2\left(\pi f \frac{L}{v_z}\right) \sin\left(\varphi_0 + 2\pi f \frac{L}{v_z}\right) . \quad (3.24)$$

⁵A change of 5° will result in a longitudinal material expansion of the aluminium based setup of 32 μm .

3. Visibility-Affecting Factors

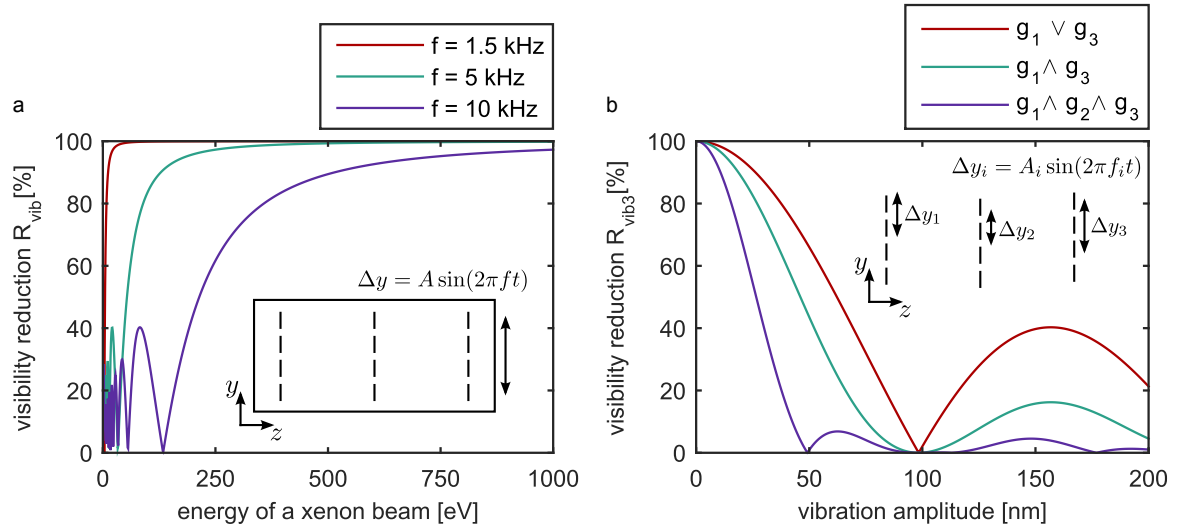


Figure 3.4.: Visibility reduction due to a fixed harmonic oscillation and independent grating oscillations. (a) If the whole setup exhibits a common oscillation ($A = d$) and the particles' inverse time of flight is in the order of the oscillation frequencies the visibility of the pattern is reduced. For the slowest particles in this work, a xenon beam with hundreds of eV, oscillations exceeding 10 kHz would be required to destroy the observed pattern. This frequency range is atypical for the noise spectrum in a laboratory, which usually experiences vibrations in the acoustic regime. Therefore, the effect of a fixed harmonic oscillation can be neglected. (b) If the three gratings vibrate independently, the visibility pattern is independent from the time of flight, as well as from the frequencies. Only the vibrational amplitude affects the pattern. Shown is the visibility reduction for different vibration configurations over the common oscillation amplitude.

3.2. Vibrations of the Three-Grating Setup

To obtain the visibility of the resulting fringe pattern, the single patterns with a phase shift following equation (2.72) have to be averaged over the initial phase position φ_0 . The phase φ_0 is thereby uniformly distributed, as the particles' arrival times are independent of the harmonic oscillation of the setup. For the sake of simplicity only the first two Fourier components are considered in the expression of the resulting signal (equation (2.72)), so that the signal can be written as

$$S(y_s) \propto 1 + \nu_0 \frac{1}{2\pi} \int_0^{2\pi} d\varphi_0 \cos\left(\frac{2\pi}{d} \Delta y(\varphi_0) + \frac{2\pi}{d} y_s\right) \quad (3.25)$$

$$= 1 + \nu_0 \frac{1}{2\pi} \int_0^{2\pi} d\varphi_0 \cos\left(\frac{8\pi}{d} A \sin^2\left(\pi f \frac{L}{v_z}\right) \sin\left(\varphi_0 + 2\pi f \frac{L}{v_z}\right) + \frac{2\pi}{d} y_s\right), \quad (3.26)$$

with ν_0 the undisturbed visibility and y_s the vertical position of the last grating to scan the pattern. With the repeated use of the angle addition and subtraction theorems and the zero-order Bessel function⁶ J_0 , the signal yields

$$S(y_s) \propto 1 + \nu_0 J_0\left(\frac{8\pi}{d} A \sin^2\left(\pi f \frac{L}{v_z}\right)\right) \cos\left(\frac{2\pi}{d} y_s\right), \quad (3.27)$$

which directly defines the visibility reduction factor

$$R_{\text{vib}} = \left| J_0\left(\frac{8\pi}{d} A \sin^2\left(\pi f \frac{L}{v_z}\right)\right) \right|. \quad (3.28)$$

Figure 3.4(a) shows the effect different vibration frequencies have, whose amplitude equals one grating period d . As the vibrational effect is more prominent for particles with a small velocity, the graph shows only the consequences for a xenon beam with energies up to 1 keV. Since the interferometer works with velocities beyond 12 km s^{-1} , corresponding to a time of flight $\tau = L/v = 12 \mu\text{s}$, frequencies below 1000 Hz can be neglected. For higher frequencies, which are less likely to appear in a laboratory, the fringe pattern of a xenon beam is altered below 1 keV. Accordingly, fixed harmonic oscillations of the whole setup are negligible in this work. Of a somewhat different nature is the case, if the three gratings oscillate independently, as discussed in the following.

3.2.2. Independent Grating Oscillations

As all three gratings in this work are mounted separately on fine-precision actuators (see chapter 4.2.2) each grating has to be considered as an independent harmonic oscillator. To calculate the resulting fringe pattern, one has to average over all possible fringe shifts weighted by their probability, which are possible for the various grating configurations. Therefore, the

⁶Named after the German mathematician Friedrich Wilhelm Bessel, the zero-order Bessel function is defined

as $J_0 = \frac{1}{\pi} \int_0^\pi d\varphi \cos(x \sin(\varphi))$.

3. Visibility-Affecting Factors

result will be independent of the three frequencies and the particles' time of flight. In a similar manner as for the fixed oscillation the reduction factor yields [64]

$$R_{\text{vib3}} = \left| J_0 \left(2\pi \frac{A_1}{d} \right) J_0 \left(4\pi \frac{A_2}{d} \right) J_0 \left(2\pi \frac{A_3}{d} \right) \right|, \quad (3.29)$$

with A_i the amplitudes of the individually vibrating gratings. As this reduction factor is independent of the particles' velocity it may not be neglected for the interferometer in this work. Figure 3.4(b) depicts the corresponding visibility reduction factor for different oscillation amplitudes and vibration configurations. In case only the first or third grating oscillates the visibility drops to zero within an amplitude range of 100 nm, while a pure oscillation of the second one would yield a faster drop of at around 50 nm. This is due to the fact that the second grating causes twice the phase shift of the resulting pattern, which is already reflected by the corresponding factor in equations (2.72) and (3.29). Vibrations measurements of the gratings fine positioner, using the piezoelectric crystal as the vibration source, indicate an oscillation amplitude around 30 nm if the resonance is hit [63]. Table 3.2 list the visibility reduction factor for an oscillation amplitude of $A = 30$ nm and different oscillation configurations. Notable among them is that an independent oscillation of all three gratings reduces the visibility down to 40 % of the initial value. For an expected fringe pattern with a contrast of 80 % this would reveal a much weaker pattern with a 32 % visibility.

In spite of the preceding, the justification of assuming the three gratings to act as independent harmonic oscillators may still be questioned. It can be argued that the resonance frequencies of the different actuators strongly depend on the load which is mounted on them. As all three gratings are mounted slightly differently (compare figure 4.6), different resonance frequencies can be safely assumed and hence the three gratings can be taken as exhibiting independent oscillations. In the worst case, where the acoustic vibration spectrum of the laboratory environment matches the grating resonances, a reduction of the initial visibility down to 40 % can be expected.

oscillating gratings	visibility reduction factor R_{vib3}
$g_1 \vee g_3$	87 %
$g_1 \wedge g_2$	75 %
g_2	53 %
$(g_1 \vee g_3) \wedge g_2$	46 %
$g_1 \wedge g_2 \wedge g_3$	40 %

Table 3.2.: Calculated visibility reduction factor R_{vib3} using equation (3.29) for different grating vibration configuration which oscillate independently but with the same amplitude of $A = 30$ nm. If all three gratings oscillate independently a fringe pattern with an initial visibility of, for example, $\nu_0 = 80$ % is reduced to $\nu_{\text{vib3}} = 32$ %. Note that the visibility reduction due to a vibration of the second grating is larger than of the first and third grating, as a shift of the second grating leads to twice as large a shift of the fringe pattern compared to the first or third grating.

3.3. Perturbations due to External Forces Acting on the Particles

The Talbot-Lau interferometer and the moiré deflectometer are both well-established devices used for measuring small particle-beam deflections arising perpendicularly to the interferometer's (or the deflectometer's) grating. A wide range of theoretical and experimental work has been reported on measuring forces ranging from electrostatic and magnetostatic forces on protons [45, 46, 67] or antiprotons [34, 44], all the way to gravitational interactions and centripetal forces on argon [38] or antihydrogen [68, 69]. This extreme sensitivity to external fields has also its negative side. If the particle beam consists of a wide range of velocity classes, the resulting pattern washes out, as each velocity class experiences a different shift on the detector. Hereinafter, first the principle of inertial sensing is introduced, followed by considering the effect of a finite velocity distribution. For simplicity, we restrict the discussion mainly to the moiré deflectometer, although the same kind of reasoning may be applied to the Talbot-Lau interferometer, too. This section concludes with a list of possible forces and limitations on their strength for the interferometer.

3.3.1. Inertial Sensitivity of the Three-Grating Setup

Consider⁷ a uniform force $F_y = ma$ parallel to the grating vector. Particles under such a condition follow parabolic paths

$$y(t) = \frac{1}{2}at^2 + v_y t + y_0 , \quad (3.30)$$

due to the uniform acceleration a , as shown in figure 3.5(a). The particle's position y is here given over the time t , while v_y denotes the particle's velocity in y -direction and y_0 the initial position at $t = 0$. Furthermore, the particles' trajectories are restricted by two arbitrary grating slits of the first and second grating with the positions $y(t = 0) = nd$ and $y(t = L/v_z =: \tau) = md$, where L is the distance between the two gratings with period d , τ the time of flight for such a distance, and n and m are integers. These constraints restrict all particle trajectories to

$$y(t) = \frac{1}{2}at^2 + \left(\frac{(m-n)d}{\tau} - \frac{1}{2}a\tau \right) t + nd . \quad (3.31)$$

A further distance L , at the position of the third grating, this yields

$$y(2\tau) = a\tau^2 - nd + 2md , \quad (3.32)$$

which is a total shift Δy with respect to the case when no uniform force acts on the propagating particle:

$$\Delta y = a\tau^2 . \quad (3.33)$$

This relation is also valid for the discussed general case with a finite slit width. As noted

⁷Following derivation follows the argument given in [45].

3. Visibility-Affecting Factors

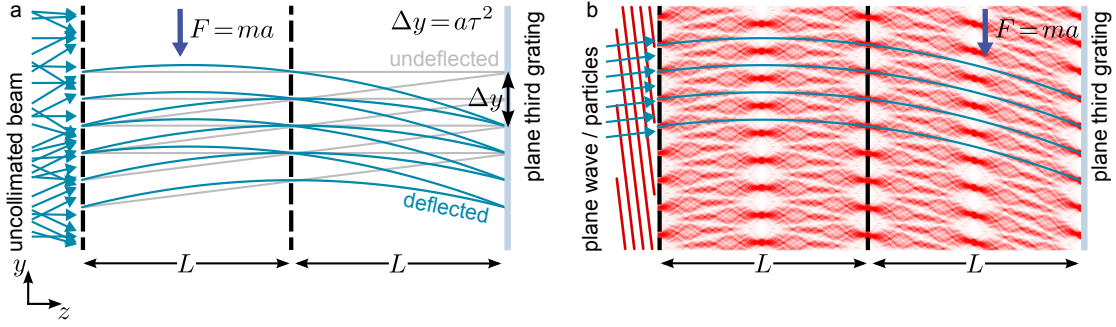


Figure 3.5.: Inertial sensitivity of the three-grating device. (a) Classical particles follow parabolic paths if a uniform force acts perpendicularly to the grating slits. The shift of the fringe pattern depends on the force and is $\Delta y = a\tau^2$, where τ denotes the time of flight between two gratings. (b) In the quantum mechanical description the underlying scalar potential of the force results in an additional phase shift for the propagating wavefield, which results in a distortion of the Talbot carpet similarly to the classical parabolic paths.

before (chapter 2.4), a phase shift of the nanoscopic pattern results directly in the same phase shift for the macroscopic moiré pattern. Therefore, it is more general to refer to the phase of the fringe under a uniform acceleration

$$\Delta\phi = \frac{2\pi}{d}\Delta y = \frac{2\pi}{d}a\tau^2. \quad (3.34)$$

If the longitudinal kinetic energy $v_z^2/2m$ of the particles is large compared to an interaction potential $|V(\vec{r})|$ the force on a particle perpendicular to the grating slits can be also implemented into the angular spectrum method for calculating the Talbot carpet (see chapter 2.2) by using the eikonal approximation [58, 70]. If the force is the gradient of a scalar potential, $F_y = -\frac{\partial}{\partial y}V(y, z)$ an additional phase factor has to be taken into account for the plane waves travelling a short time $\Delta t = \Delta z/v_z$, which is

$$\varphi(y) = -\frac{1}{\hbar v_z} \int_{\Delta z} dz V(y, z). \quad (3.35)$$

Here we assumed that the horizontal velocity is much larger than the vertical one ($v \approx v_z \gg v_y$). For a uniform field ($V(x, z) \equiv V(x)$) this result can be simplified to

$$\varphi(y) = -\frac{1}{\hbar v} V(y)\Delta z. \quad (3.36)$$

Considering this additional phase for the wavefield, the Talbot carpet deforms as shown in figure 3.5(b). As expected the Talbot carpet follows the classical trajectories resulting in the same phase shift in the plane of the third grating.

3.3.2. Critical Acceleration and the Effect of Finite Energy Distribution

A phase shift does not, per se, alter the fringe visibility of the macroscopic pattern and hence disturb the working principle of the interferometer. A problem occurs only if the particle beam a force acts upon has a finite velocity distribution. If one considers an energy distribution with mean energy E_{kin} and a certain energy spread ΔE , according to equation (3.34) each energy class experiences a different shift. Since the final fringe pattern consists of a sum of individual fringes, each with its own velocity class, the final pattern suffers from a reduced visibility if the individual fringes are out of phase with respect to each other. A critical acceleration can be defined [46, 47] posing a limit on the strength of an external field such that the total phase shift between the two specified energies $E_{\pm} = E_{\text{kin}} \pm \Delta E/2$ does not overcome π , i.e.

$$\Delta\varphi = \frac{2\pi}{d} |\Delta y(E_-) - \Delta y(E_+)| \stackrel{!}{\ll} \pi . \quad (3.37)$$

With equation (3.34) and the time of flight $\tau^2 = L^2 m/2E_{\pm}$ it follows

$$\frac{aL^2 m}{2d} \left(\frac{1}{E_-} - \frac{1}{E_+} \right) \ll 1 , \quad (3.38)$$

$$\frac{aL^2 m}{2d} \left(\frac{4\Delta E}{4E^2 - \Delta E^2} \right) \ll 1 . \quad (3.39)$$

With the assumption that the energy spread is small compared to the mean energy (i.e. $\delta E = \Delta E/E \ll 1$) one finds a simplified expression for the critical acceleration

$$a_{\text{crit}} = \frac{d}{mL^2} \frac{E^2}{\Delta E} \quad (3.40)$$

$$= \frac{d}{mL^2} \frac{E}{\delta E} . \quad (3.41)$$

Figure 3.6 shows the effect an acceleration perpendicular to the grating slits has on an particle beam with a finite energy spread. If, for a given de Broglie wavelength, the critical acceleration exceeds the acceleration caused by an external force, the visibility of the interferometric fringe pattern is influenced only to a negligible extent. Otherwise, if the critical acceleration is smaller than the acceleration caused by the force, the visibility is altered. In the noticeably graph 3.6, the external force is set such that the resulting acceleration on a hydrogen beam equals the critical acceleration for the beam parameter $E = 3.68 \text{ keV}$ (i.e. $\lambda = h/\sqrt{2mE} = 0.47 \text{ pm}$; dashed line) and $\delta E = 1\%$. Accordingly, the visibility undergoes only minor changes for lower de Broglie wavelengths (i.e. higher energies) but almost vanishes for higher wavelengths. With the above definition of a critical acceleration we can now discuss possible primary causes of such an acceleration on the particles in the next step.

3. Visibility-Affecting Factors

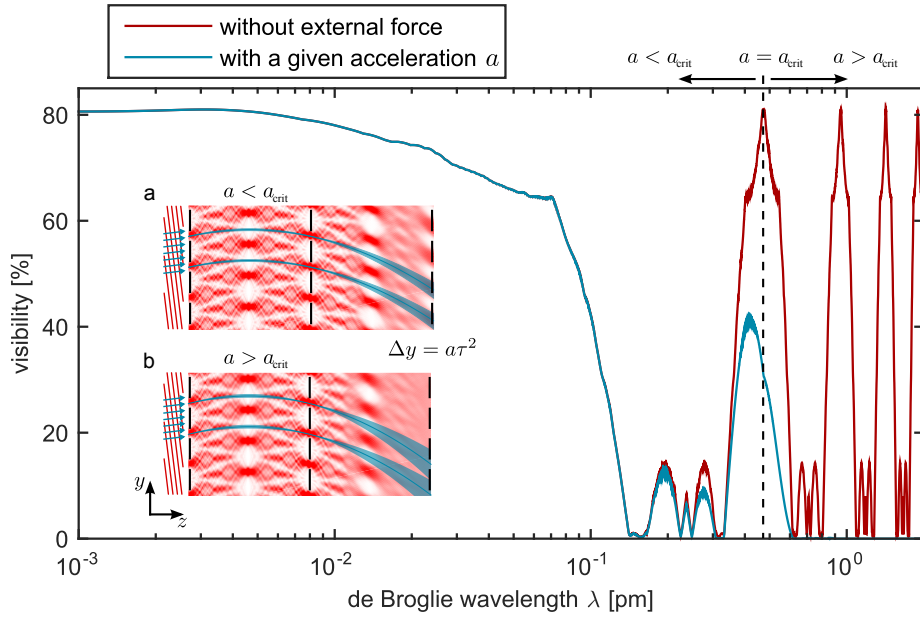


Figure 3.6.: Effect of an external force acting on a particle beam with a finite energy distribution. The acceleration a is set to the critical acceleration a_{crit} (compare equation (3.41)) of a hydrogen beam with a relative energy spread of $\delta E = 1\%$ and a mean energy of $E = 3.68$ keV (i.e. $\lambda = h/\sqrt{2mE} = 0.47$ pm; dashed line). For higher de Broglie wavelengths the critical acceleration a_{crit} is below the given value of a , resulting in a significant visibility reduction of the interferometric pattern. For lower wavelengths (i.e. higher particle energies) the given acceleration a undercuts the critical acceleration a_{crit} . This implies that the visibility is thereby influenced only to a negligible extent. (The value of the given acceleration $a = 4.6 \times 10^8$ m s^{-2} is equivalent to the force which an electric or magnetic field causes on a positively charged hydrogen atom with a strength of $E = 4.8$ V m^{-1} , or $B = 57$ mG, respectively.) The small insets (a) and (b) show the underlying Talbot carpets if the acceleration is smaller or higher than the critical value for a given particle beam. Remarkable is the patterns' washout for $a > a_{\text{crit}}$.

3.3.3. Different Forces Arising in the Setup

The Talbot-Lau interferometer in this work is used with a wide range of particles. Starting with the light hydrogen atom it runs with noble gases up to xenon. Trajectories of such neutral particles can be altered due to an electric or magnetic field gradient, as the particles possess an electric or magnetic dipole moment. Moreover, as the interferometer can be seen as an important step to show interference with charged particles, the effect of electric and magnetic fields on charged particles has to be considered. Table 3.3 lists a number of primary causes of the acceleration and gives an explicit formula to calculate their critical values. Furthermore, the forces are compared to the much weaker but more intuitive force, the gravitation. The formulae for the magnetic and electric field gradients follow the derivation in [47] and hold for hydrogen atoms with principle quantum numbers n larger than $n > 10$. In addition, the critical parameters are calculated for a hydrogen beam with arbitrary energies and relative spread, but also for a 100 eV beam, the lowest possible value in the setup, with an energy spread of 1%. The latter is expected to be realised in this work (see chapter 4.1.3). For the sake of completeness it should be realised, that an energy spread by itself can also smear out the pattern in the Talbot-Lau interferometer. This is owing to the grating distance's not matching the Talbot length of each energy class present in a realistic particle beam. Consequently, fringe patterns with a lower visibility are summed up with high-visibility fringes, resulting in a smearing-out of the observed pattern. Nevertheless, for a relative energy spread expected in this work, $\delta E \approx 1\%$, this effect is negligible in comparison to the visibility reduction due to external fields [47].

cause		formula	hydrogen in this work	$E = 100 \text{ eV}, \delta E = 1\%$
Gravitation	g_{crit}	$\frac{d}{mL^2} \frac{E}{\delta E}$	$1256 \text{ m s}^{-2} \text{ eV}^{-1} \cdot \frac{E[\text{eV}]}{\delta E}$	$12.6 \times 10^6 \text{ m s}^{-2}$
E-field Grad.	$ \nabla E _{\text{crit}}$	$\frac{d}{L^2} \frac{2}{3ea_0} \frac{E}{n^2 \delta E}$	$1.65 \times 10^5 \text{ V m}^{-2} \text{ eV}^{-1} \cdot \frac{E[\text{eV}]}{\delta E} \frac{1}{n^2}$	$1.65 \times 10^9 \text{ V m}^{-2} \cdot \frac{1}{n^2}$
B-field Grad.	$ \nabla B _{\text{crit}}$	$\frac{d}{L^2 \mu_B} \frac{E}{n \delta E}$	$2.3 \text{ kG m}^{-1} \text{ eV}^{-1} \cdot \frac{E[\text{eV}]}{\delta E} \frac{1}{n}$	$23 \times 10^3 \text{ kG m}^{-1} \cdot \frac{1}{n}$
E-field	E_{crit}	$\frac{d}{L^2 q} \frac{E}{\delta E}$	$131 \times 10^{-7} \text{ V m}^{-1} \text{ eV}^{-1} \cdot \frac{E[\text{eV}]}{\delta E}$	131 mV m^{-1}
B-field	B_{crit}	$\frac{d}{L^2 q} \sqrt{\frac{m}{2}} \frac{\sqrt{E}}{\delta E}$	$9.5 \times 10^{-6} \text{ G} / \sqrt{\text{eV}} \cdot \frac{\sqrt{E[\text{eV}]}}{\delta E}$	9.5 mG

Table 3.3.: Possible external forces that can alter the visibility of the interferometer. While gravity acts on the mass of the particles, the E- and B-field gradients act on the electric and magnetic dipole moment, respectively. If the particles are charged the influence of electric and magnetic fields has to be considered further. Precise formulae are given. The relations for the E- and B-field gradient following the derivations given in [47] where only hydrogen atoms with the principle quantum number $n > 10$ are considered with the Bohr radius a_0 and the Bohr magneton μ_B . The critical values are calculated for a hydrogen beam (for the E- and B-field a proton beam respectively) with the parameters of the setup used in this work but keeping the energy and energy spread variable. The last column gives the absolute value for the critical parameters assuming the lowest energy possible in this work (100 eV) and an energy spread of 1%.

3. Visibility-Affecting Factors

The resulting maximal fields given in table 3.3 are effortless to avoid if one uses Faraday cages and magnetic mu-metal shielding, as described for the experimental setup in chapter 4.3. A much greater impact might have forces which occur while the particles pass the grating. Such interactions between the particles and the grating material are discussed in the following section.

3.4. Realistic Gratings with Intra-Grating Interaction

Up to this point the gratings have been described as ideal transmission gratings (compare equation (2.8)). However, such an idealisation neglects the finite thickness l of gratings. Such a longitudinal grating extension provides an interaction time t between the particle beam and the gratings, dependent on the particle's velocity v_z . Consequently, the grating transmission function has to be adjusted, taking into account energy- and location-dependent modifications in the process. In general, intra-grating interactions affect the Talbot-Lau interferometer more than they affect, for instance, a Mach-Zehnder interferometer. This is the case because small phase shifts are more dominant in a near-field interferometer than of a far-field regime [59]. In the following we start with a discussion about the mathematical description of such intra-grating interactions to list afterwards explicitly possible forces inside the grating slits. The subsection concludes with an analysis of the effective open fraction and the effect such interactions have on the visibility profile.

3.4.1. Mathematical Description of Intra-Grating Interactions

Assuming the grating walls to be parallel and straight, and edge effects to be negligible, one can express the grating-particle interaction with the potential $V(y, z)$. Furthermore, the interaction is well described by the eikonal approximation (compare equation (3.35)) [59,71,72]. The modified grating function therefore yields

$$\tilde{g}(y) = g(y) \exp \left(-\frac{i}{\hbar v_z} \int_l dz V(y, z) \right) \quad (3.42)$$

$$= g(y) \exp \left(-i \frac{l}{\hbar v} V(y) \right) . \quad (3.43)$$

For simplicity, in the last step we assumed that the interaction potential is independent of the z -position inside the grating (i.e. $V(y, z) \equiv V(y)$) and that the longitudinal velocity v_z is much greater than the transverse, and thus $v_z \approx v$. Here $g(y)$ denotes the grating function of equation (2.8) for an ideal grating whose amplitude $\{0, 1\}$ describes the grating structure. With such a modified grating function the corresponding visibility of the interference pattern and its underlying Talbot carpet can be obtained with the angular spectrum method (section 2.2) or in the Wigner representation (section 2.5). Note that the modified grating function has to be only considered for the second grating. This is due to the fact that the effect of an uncollimated beam at the beginning overcomes the momentum change of diffraction on the first grating, while the third grating only acts as a mask to facilitate the readout of the

3.4. Realistic Gratings with Intra-Grating Interaction

nanoscopic pattern. Mathematically, this fact can be seen in equations (2.48) and (2.69) where only the absolute square of the two grating functions g_1 and g_3 has to be considered. Hence, the complex phase is not considered that contains the influence of intra-grating interaction. Only for the case where the eikonal approximation (i.e. equation (3.43)) is invalid, for example for very strong interaction potentials, the effective open fraction is altered which is therefore also relevant for the first and third grating and discussed later.

If we follow the Wigner representation in chapter 2.5 we have to modify the Fourier coefficients ($b_n \rightarrow \tilde{b}_n$; equation (2.57)) for the grating function of the second grating. This yields [59]

$$\tilde{b}_n = \sum_j b_j \tilde{c}_{n-j} \quad (3.44)$$

with

$$\tilde{c}_n = \frac{1}{d} \int_{-\frac{d}{2}}^{\frac{d}{2}} dy e^{-ink_d y} \exp\left(-i \frac{l}{\hbar v} V(y)\right). \quad (3.45)$$

The Fourier coefficient $B_j^{(T)}$ to express the density pattern (equation (2.72)) and the visibility of the signal (equation (2.75)) change accordingly

$$\tilde{B}_j^{(T)} = \sum_{m \in \mathbb{Z}} \tilde{b}_m \tilde{b}_{m-j}^* \exp\left(i\pi \frac{j^2 - 2mj}{2} \frac{L}{L_T}\right). \quad (3.46)$$

Similar corrections have also to be done for the classical phase-space representation (compare chapter 2.6.2). Here the classical Fourier components $B_m^{(C)}$ to calculate the signal (equation (2.88)) and the visibility (equation (2.88)) have to be replaced by [59]

$$\tilde{B}_m^{(C)} = \sum_{j \in \mathbb{Z}} B_j^{(C)} \tilde{C}_{m-j}^m \quad (3.47)$$

with

$$\tilde{C}_n^m = \frac{1}{d} \int_{-\frac{d}{2}}^{\frac{d}{2}} dy e^{-imk_d y} \exp\left(-i\pi n \frac{L}{d} \frac{Q(y)}{p_z}\right). \quad (3.48)$$

$Q(y)$ denotes the momentum kick particles get by the classical force $-\partial_y V(y)$, while they travel horizontally through the grating slit. It can be quantified as:

$$Q(y) = -\partial_y V(y) \cdot \frac{l}{v_z}. \quad (3.49)$$

3. Visibility-Affecting Factors

With the expounded modification for the Talbot-Lau setup in the Wigner representation and the classical moiré deflectometer in the phase-space description, one has powerful tools to calculate the expected visibilities assuming intra-grating interactions. Still question remains open what kind of interaction potentials one has to consider. The following gives an overview of typical particle grating interactions which have to be considered in this work.

3.4.2. Intra-Grating Interactions

The Talbot-Lau interferometer works with a wide range of neutral particles. Starting from hydrogen and helium up to the higher mass particles as argon, krypton, and xenon. In general such neutral particles experience an attractive van der Waals force close to a surface and hence is the first interaction to be considered inside the gratings. Anyhow the gratings where also exposed to energetic charged particles giving rise to another force to be considered, the induced dipole force. Such charges, for example arising during the examination of the gratings in an electron microscope or for first interferometric tests with protons and other ions, have a penetration depth of several nanometres into the gratings' material⁸. This may implant permanent charges into the grating material which cause electric gradient fields and hence act upon the particles due to their polarisability. Self-explanatory is the third interaction to be discussed, the electrostatic interaction which occur for running the interferometer with charged particles.

London Dispersion Force

For non-polar atoms the London dispersion force, or sometimes called the attractive van der Waals force, is a simple and realistic description of the interaction between a quantum object and a wall. The experimental agreement of such an interaction modelled with the London dispersion force was shown for a number of different particles [71, 72]. The interaction potential is given by [74]

$$V(l) = -\frac{C_3}{r^3}, \quad (3.50)$$

with r denoting the distance between the wall and the particle and $C_3 > 0$ the interaction constant. For many combinations of different atoms and wall materials the interaction constant can be retrieved experimentally [71, 72, 75]. Nevertheless, in general it is estimated from the Lifshitz formula [74, 76, 77]

$$C_3 = \frac{\hbar}{4\pi} \int_0^\infty d\omega \alpha(i\omega) \frac{\epsilon(i\omega) - 1}{\epsilon(i\omega) + 1}. \quad (3.51)$$

Here α denotes the dynamic polarisability of the particle which can be obtained either from experimental data, for example with absorption spectroscopy, or with appropriate models. The dielectric function ϵ for the wall material can be obtained in a similar fashion.

⁸For example 10 keV-protons have a stopping range of approximately 80 nm [73].

3.4. Realistic Gratings with Intra-Grating Interaction

Table 3.4 gives an overview of the interaction constants C_3 for different atoms. It is given once for the interaction with a wall made of Si_3N_4 and once for gold. It is worth noticing, that the van der Waals interaction is stronger with a conducting plate (Au) than an insulator (Si_3N_4). As the gratings used in this work are made of Si_3N_4 but are coated with a gold palladium mixture (compare chapter 4.2.1) the C_3 values for the interaction with gold are used hereafter.

The force due to the van der Waals interaction diverges close to the grating walls, rendering the eikonal approximation insufficient. However this does not appreciably change the interference pattern in this case as it will be discussed later in section 3.4.3.

Inside a grating slit one has to consider two walls. The final potential inside the grating yields therefore

$$V_{\text{vdW}}(y) = V\left(y + \frac{\eta d}{2}\right) - V\left(y - \frac{\eta d}{2}\right) \quad (3.52)$$

$$= -C_3 \left(\frac{1}{\left(y + \frac{\eta d}{2}\right)^3} - \frac{1}{\left(y - \frac{\eta d}{2}\right)^3} \right) \quad \text{for } y \in \left] -\frac{\eta d}{2}, \frac{\eta d}{2} \right[, \quad (3.53)$$

with $y = 0$ the middle of the grating slit. The corresponding force is

$$F_y(y) = -\partial_y V_{\text{vdW}}(y) \quad (3.54)$$

$$= -3C_3 \left(\frac{1}{\left(y + \frac{\eta d}{2}\right)^4} - \frac{1}{\left(y - \frac{\eta d}{2}\right)^4} \right) . \quad (3.55)$$

Induced Electric Dipole and Electric Field Gradient

Neutral atoms inside an electric field \vec{E} will exhibit an induced electric dipole moment

$$\vec{d} = \alpha_0 \vec{E} , \quad (3.56)$$

dependent on their static polarisability α_0 . For reference, α_0 for the different atoms is listed in table 3.1. The electric dipole moment gives rise to a potential

$$V = -\vec{d} \cdot \vec{E} \quad (3.57)$$

$$= -\alpha_0 |\vec{E}|^2 . \quad (3.58)$$

Assuming N charges are implanted into the grating slits or on the surface of the intra-grating walls, this charge distribution can be represented in first order with a single charge $Q = Ne$ in the middle of each grating bar, with e the elementary charge. Neglecting minor changes along the z -direction, this results in an electric field E_y perpendicular to the beam axis inside the grating slits of

$$E_y(y) = \frac{Q}{4\pi\epsilon_0} \left(\frac{1}{\left(y + \frac{\eta d}{2}\right)^2} - \frac{1}{\left(y - \frac{\eta d}{2}\right)^2} \right) \quad \text{for } y \in \left] -\frac{\eta d}{2}, \frac{\eta d}{2} \right[. \quad (3.59)$$

3. Visibility-Affecting Factors

Here we considered only the charges of the nearest neighbouring bars with equal amount, while $y = 0$ is the centre of the grating slit. The potential can thus be written as

$$V(y) = -\frac{\alpha_0 Q^2}{16\pi^2 \epsilon_0^2} \left(\frac{1}{(y + \frac{\eta d}{2})^2} - \frac{1}{(y - \frac{\eta d}{2})^2} \right)^2 \quad \text{for } y \in \left] -\frac{\eta d}{2}, \frac{\eta d}{2} \right[, \quad (3.60)$$

and the force

$$F_y(y) = \frac{\alpha_0 Q^2 \eta^2 d^2}{2\pi^2 \epsilon_0^2} y \frac{\frac{\eta^2 d^2}{4} + 3y^2}{(\frac{\eta d}{2} - y)^5 (\frac{\eta d}{2} + y)^5} . \quad (3.61)$$

Coulomb Interaction

If the three-grating setup is to work with charged particles as well, the above-mentioned implanted charges will have a greater effect on a charged-particles beam due to Coulomb interaction. The potential in this case yields

$$V(y) = -\frac{Qq}{4\pi\epsilon_0} \left(\frac{1}{y + \frac{\eta d}{2}} - \frac{1}{y - \frac{\eta d}{2}} \right) \quad \text{for } y \in \left] -\frac{\eta d}{2}, \frac{\eta d}{2} \right[, \quad (3.62)$$

where q is the charge of the particle beam. The corresponding force equals

$$F_y(y) = -\frac{Qq}{4\pi\epsilon_0} \left(\frac{1}{(y + \frac{\eta d}{2})^2} - \frac{1}{(y - \frac{\eta d}{2})^2} \right) . \quad (3.63)$$

	$C_3\text{-Si}_3\text{N}_4$ [meV Å ³]	$C_3\text{-Au}$ [meV Å ³]	α_0 [1×10^{-42} C m ² V ⁻¹]
H		544	74.4
He	100	274	23.3
Ar	700	1768	183.2
Kr	1100	2455	276.4
Xe		3533	450.7

Table 3.4.: Interaction constants and static polarisability for different atomic species. C_3 is given for a wall made of Si_3N_4 and gold. As the gratings used in this work are made of Si_3N_4 coated with a gold-palladium mixture (compare chapter 4.2.1) the C_3 values for the interaction with gold are used. The listed values are compiled from various experimental studies [72, 75, 76, 78].

All thus-far-discussed potentials describing the intra-grating interactions diverge at close proximity to the grating walls, making the eikonal approximation insufficient. Therefore, the following subsection discusses a reasonable cut-off criterion to take this affect into account.

3.4.3. Limit of the Eikonal Approximation and Effective Open Fraction

The eikonal approximation to evaluate the additional phase (equation (3.43)) which the particles accumulate while travelling through the grating slits may break down in a close vicinity to the grating walls, as the potential diverges. In a semi-classical notion the eikonal approximation holds for the high-energy limit. This requires a well-collimated beam (i.e. $p_z/p \approx 1$) with a short interaction time, a small grating thickness l or a small interaction strength, so that the particle trajectories through the slits can be described as straight, accumulating a phase along the z -axis with fixed y (compare equation (3.43)). Close to the wall these conditions are invalid, as classical particle trajectories would be deflected towards the grating bars in such a way, that they hit them during the transition time. Since only a small fraction of the semi-classical trajectories are affected these regions do not alter the overall visibility profile appreciably. Nevertheless, using the Wigner-representation or the angular spectrum method to calculate the visibility the regions close to the grating bars reduces the visibility due to numerical noise. Hence, following figure 3.7(a), a reasonable criterion to ignore the region close to the grating bars is defined [58]. This criterion states that in a classical picture all particles are rejected if they would hit the inner wall of the gratings while travelling the grating within the time $t_l = l/v_z$. For a given intra-grating potential $V(y)$, the time for a particle to hit the wall starting at a distance y_0 away from the wall is

$$T(y_0) = \sqrt{\frac{m}{2}} \int_0^{y_0} dy \frac{1}{\sqrt{-V(y)}}, \quad (3.64)$$

assuming the initial transverse velocity to be zero, i.e. $v_y = 0$. The point where the passage time t_l equals the time to hit the wall T , defines the critical distance y_c and therefore the cut-off criterion. Considering the before listed potentials but only from one side of the wall⁹, the critical distances for the different potentials solving the conditions $t_l \stackrel{!}{=} T$ yield:

$$\text{London dispersion force: } y_c = \sqrt[5]{\frac{25l^2 C_3}{4E}} \quad (3.65)$$

$$\text{Induced dipole: } y_c = \sqrt[6]{\frac{9l^2 \alpha_0 Q^2}{16\pi^2 \epsilon_0^2 E}} \quad (3.66)$$

$$\text{Coulomb interaction: } y_c = \sqrt[3]{\frac{9l^2 Qq}{16\pi \epsilon_0 E}}. \quad (3.67)$$

E denotes hereby the particles kinetic energy. The critical distance reduces the gratings' effective open fraction according to

$$\eta' = \frac{b - 2y_c}{d}. \quad (3.68)$$

⁹The potential in equation (3.60) for the force due to an induced electric dipole was approximated close to the wall with a $1/r^4$ dependence, where r is the distance to the wall.

3. Visibility-Affecting Factors

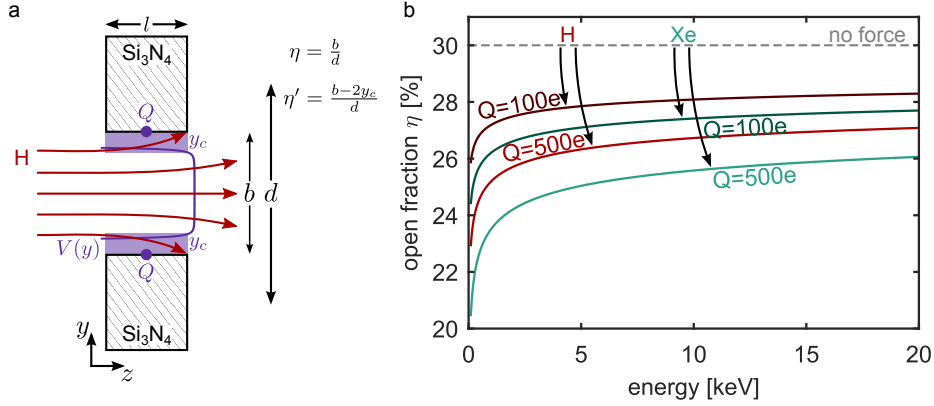


Figure 3.7.: Effective open fraction due to intra-grating interaction. (a) Implanted charges inside the grating material change the particles' trajectories as they pass the grating slits. Representing the charges as one charge Q placed at the slit walls, the potential $V(y)$ describes the intra-grating interaction due to an induced dipole force. As the potential diverges close to the walls a reasonable cut-off criterion is defined. The critical distance y_c defines the region close to the wall where classical trajectories would hit the wall while passing the grating. This defines an effective open fraction η' , where the slit width is reduced by twice the critical distance y_c . (b) The effective open fraction for an induced dipole interaction due to implanted charges. Shown is the case for hydrogen and xenon beams as a function of the kinetic energy with an initial open fraction of 30 %.

Although, the additional phase shift and hence diffraction has to be only considered for the second grating, the change in the open fraction has to be taken into account even for the first and last grating. The reason for this lies in the fringe visibility's sensitivity to the corresponding open fraction as discussed previously (compare figure 2.6(c)).

Figure 3.7(b) pictures the effect an accumulated charge Q placed at the inner grating walls has on the open fraction due to an induced dipole force on the particles. If a charge of $Q = 100e$ is implanted on each slit wall, the open fraction is reduced from initial 30 % down to approximately 28 % for a hydrogen beam, while the slower xenon beam experience an even smaller slit width. Increasing the implanted charge Q results in a further reduction of the effective open fraction. Note that the effective open fraction depends on the velocity, i.e. particles energy, and hence the open fraction decreases significantly for decreasing energies. It was shown [58] that the critical distance and hence the reduced effective open fraction are well chosen, as the phase factor calculated with the eikonal approximation is almost identical to the exact phase factor within the slit width reduced by the critical distance.

3.4.4. Effect of Intra-Grating Interactions

Having introduced different possible intra-grating interactions, the question remains what kind of interaction has to be considered in the scope of this work. For the ideal case of thin, non-charged-up transmission gratings made of Si₃N₄ and the interferometer run with non-polar atoms, the London dispersion force, is the only force among the listed to be considered.

3.4. Realistic Gratings with Intra-Grating Interaction

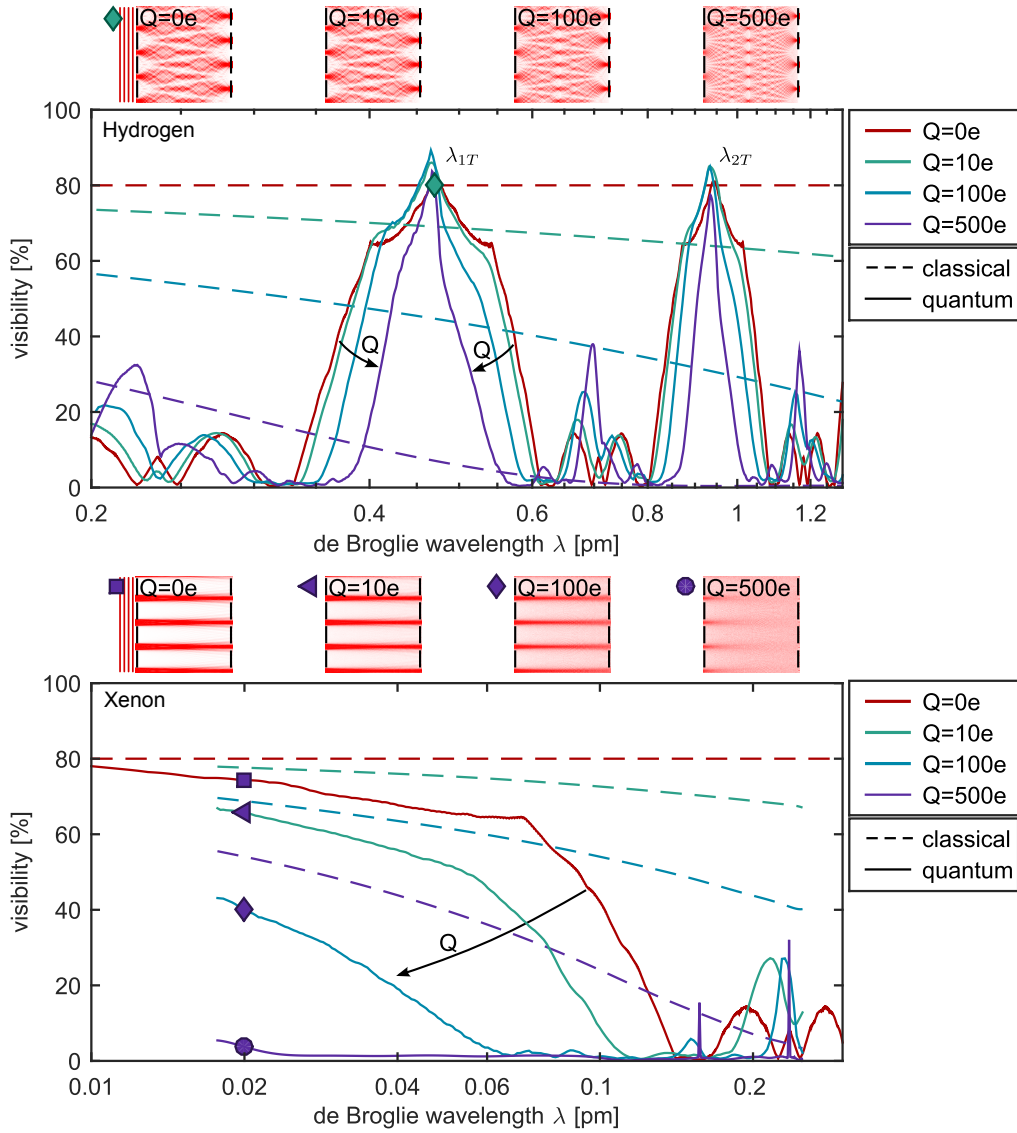


Figure 3.8.: The effect of intra-grating interactions due to implanted charges inside the grating. Hydrogen: An increasing number of charges Q do not affect the visibility significantly for wavelengths where the grating distance corresponds to multiples of the Talbot length (visibility peaks λ_{nT}) but reduces the width of the maxima. In contrast, assuming classical trajectories the visibility is steadily reduced with increasing Q up to the point where the fringe pattern vanishes. Xenon: The wavelength regime accessible with xenon atoms in this work is close to the classical limit. The visibility is reduced also in this case with increasing Q . The small insets on top of the respective images show the underlying Talbot carpet for different charges. The reduced contrast of the pattern can be noted. Note that for the classical calculations the notional wavelength of $\lambda = h/mv$ is assumed.

3. Visibility-Affecting Factors

In spite of, being the leading force to be considered in the field of large and thermal molecule interferometry [26, 58], it quickly becomes clear that for atom interferometry with energies in the range of keV, the effect is negligible. This is mainly owing to the reduction of the passage time in an atomic interferometer by more than one order of magnitude in comparison with an conventional molecular interferometer. Furthermore, the minimal effect of the van der Waals interaction can be noticed on the respective critical distance y_c , which is below 1 nm for all possible configurations in this work. Finally, simulations using the eikonal approximation show that the change in the visibility profile is below 3%.

If more noticeable deviations of the visibility profile occur, stronger interactions have to be considered such as the mentioned induced electric dipole interaction. This requires the gratings to be charged up appropriately. Figure 3.8 shows the effect a charged grating has on a neutral hydrogen and xenon beam respectively due to the mentioned induced dipole force. The upper graph shows the visibility behaviour for a hydrogen beam with wavelengths around the first and second visibility maxima, corresponding to the wavelengths where the grating distance fits the Talbot length, once and twice, respectively (compare equation (2.6)). Given is the visibility evolution considering the wave-nature of the particle and only considering classical trajectories. For the classical calculations a notional wavelength of $\lambda = h/mv$ is assumed. The effect of an increasing implanted charge Q inside the grating bars becomes prominent around the visibility peaks. While in the classical case the visibility is drastically reduced with an increasing number of charges, the high visibility in the maxima remains unchanged in the quantum description albeit with a reduced width of the peak structure. This leads to the remarkable artefact that for a high number of charges (here $Q = 500e$), no fringe pattern can be observed in the classical case, whereas high visibility fringes still remain in the wave-picture. Note that the asymmetry around the visibility peaks results from the fact that particles with smaller wavelength, and hence greater velocity, acquire a smaller phase according to equation (3.43) compared to particles with larger wavelength.

For a neutral xenon beam (figure 3.8 bottom), which covers the transition to the classical regime in this work, the picture is slightly different. While the pattern formed with classical trajectories still exhibits high-contrast fringes, the pattern is further reduced in the quantum description, as the force-free case already shows a significant visibility reduction with respect to the classical description.

The examples of hydrogen and xenon beam both show that implanted charges inside the grating significantly change the visibility dependence as a function of the particles' species and wavelength. Furthermore, the reduction in the width of the visibility maxima and the reduction for the heavy particles close to the classical limit allow to re-estimate the implanted charges with given measured data. This will be done during the discussion of the data in chapter 5.3, which also allows us to discuss the possibility of ion interferometry with the given three-grating setup. Therefore the estimated implanted charges have to be considered via the Coulomb interaction with the ions, which is discussed in chapter 5.4.

3.5. Summary

This chapter discussed in detail the multiple aspects which influence the visibility of the fringe pattern.

Having started with the alignment requirements of the three gratings with respect to each other, we observed a strong dependence of the pattern on the divergence of the beam, and state relations to calculate the critical parameters in an arbitrary setup for which the visibility of the pattern vanishes completely. Thereby we noticed that for the concrete setup used in this work longitudinal misalignments have to be sufficiently better aligned than $100\ \mu\text{m}$. Moreover, we found that a difference in the grating pitches of $100\ \text{pm}$ leads to disappearance of the pattern.

Considering vibrations of the setup, we learned that a fixed harmonic oscillation of all three gratings is only of relevance if one considers vibrational noise above $10\ \text{kHz}$, which is an atypical frequency range for the noise spectrum in a laboratory. However, if the three gratings oscillate independently, small vertical amplitudes in the range of tens of nanometre can result in a visibility reduction down to 50% of the initial expected value.

Besides mechanical constraining forces, both, external forces and forces arising inside the grating slits, also affect the visibility pattern. Therefore, a critical acceleration was introduced, which posits the maximum strength an external field can have before the field's acceleration completely washes out the pattern. To illustrate the strength of the critical field, several scenarios were considered: Gravitation, electric- and magnetic-field gradients and a homogeneous electric- and magnetic-field.

The intra-grating interaction causes an additional phase shift for particles passing the grating, depending on the position within the grating. We discussed this effect for a beam of neutral particles and stated that van der Waals interaction can be neglected. More prominent are the charges which may be implanted inside the semiconducting grating material, causing forces due to induced dipole interactions. We found that already a hundred implanted charges inside the grating bars change the profile of the visibility evolution with respect to the particles' de Broglie wavelengths.

Having provided the detailed discussion of possible visibility-affecting factors, we now turn to the experimental setup and its construction. Thereby we explain how the already mentioned mechanical constraints are accomplished and the external fields avoided. The intra-grating interactions, which cannot be fully avoided in our setup, are therefore only considered in the last chapter where we re-estimate the number of charges within the gratings and discuss the possibility of an ion interferometer.

4. Experimental Setup: Characteristics and Performance

The previous chapters gave an essential understanding of Talbot-Lau interferometry, a remarkable technique to prove the wave nature of non-coherent particle sources and with a clear transition to the classical case, the moiré deflectometer. Depending on the momentum of the particles, the same setup has to be described with quantum mechanics or can be expressed in classical terms. This section shows the implementation of a single experimental setup for a wide range of particles, which can show the full wave nature of the particles but also enables to go to the classical limit.

A sketch of the experimental setup is depicted in figure 4.1. The first part of the setup consists of an electron cyclotron resonance (ECR) source supplied with different gases such as hydrogen, helium, argon, krypton, or xenon. Depending on the gas, the source provides different kind of particles, both charged and neutral, as well as photons. These are separated with a Wien filter and a pair of Helmholtz coils. A subsequent chamber which can be filled with nitrogen serves to neutralise charged particles without energy loss, while the residual charges are subsequently deflected with two electrostatic plates. A moveable Faraday cup along the beam line is used for beam diagnostics. In front of the interferometer, exchangeable pinholes are placed to control the beam's divergence. The experimental stage consists of the three-grating interferometer, discussed previously, and is magnetically and electrically shielded with mu-metal and copper tubes. To spatially detect the pattern after the beam has passed the interferometer, a microchannel plate with a phosphor screen is placed afterwards. The particle impacts on the screen are imaged with a camera.

In the following, every part of the experiment is described in detail. Moreover data analysis of the camera images is discussed, especially in relation to the retrieval of the crucial information: the visibility of the pattern. The chapter concludes with systematic measurements to characterise the setup, in particular the precision of the grating pitch, an independent measurement of the beam divergence, and the stability of the interferometer.

4.1. Making Well-Defined Particle Beam

Having a well-defined particle beam in mass and energy is crucial to run the interferometer. An electron cyclotron resonance (ECR) source delivers not only a variety of different ions out

4. Experimental Setup: Characteristics and Performance

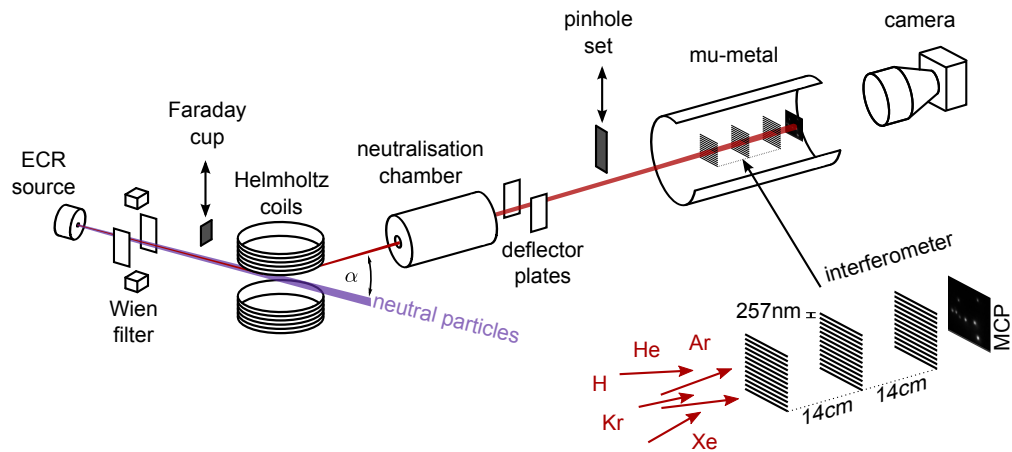


Figure 4.1.: Experimental setup: An ECR source with a plasma delivers both charged and neutral particles. The charged particles are separated with a Wien filter, while the neutrals are separated from the beam with a pair of Helmholtz coils. A variable small angle α between the source and the experimental stage can be adjusted to choose between the neutral and the charged beam to enter the experiment. A neutralisation chamber that can be flooded with nitrogen serves to neutralise the charged particles beam. The deflector plates behind the neutralisation chamber separate the generated neutral particles from the remaining charged particles. The experimental stage consists of the three-grating Talbot-Lau interferometer, which is magnetically and electrically shielded. To detect the particles at the end of the line, a microchannel plate with a phosphor screen and a camera are placed upstream. A moveable Faraday cup and a moveable set of pinholes are used for beam diagnostics and to control the beam's divergence, respectively.

of the plasma but it also generates photons corresponding to the spectral line of the used gas. Furthermore, neutral particles are formed out of the ions leaving the source through collisions. Hence, a Wien filter placed directly in front of the source selects one charged-particle species, while a subsequent pair of Helmholtz coils separate the selected charged particles from the neutral ones. A moveable Faraday cup placed behind the Wien filter not only helps to resolve the source spectrum, but it also gives an insight to the energy spread of the selected charged beam. The consecutive nitrogen gas target converts the charged beam via charge exchange to a neutral particle beam with the same energy. Different pinholes in front of the experimental stage collimate the beam for the interferometer. All these components are necessary to obtain a well-defined beam and are subsequently discussed in detail to give a deeper understanding about the characteristics of the particle beam which enters the interferometer.

4.1.1. ECR Ion Source

Electron cyclotron resonance (ECR) sources are widely used in various fields such as in medical proton therapy [79], in condensed matter physics for semiconductor manufacturing and cleaning [80], or in general in particle physics [81]. Their simple assembly and easy handling is the main reason, for which they are used for the generation of beams consisting of protons [45, 46, 82, 83] and multiple other charged ions such as argon and xenon [84–86]. The principle of such sources is shown in figure 4.2. A magnetic field B and radio frequency field are superimposed over each other inside a small cavity filled with a gas. Under the electron cyclotron resonance condition

$$\omega_{RF} \stackrel{!}{=} \omega_c = \frac{eB}{m_e} , \quad (4.1)$$

a plasma is ionised. Here the radio frequency ω_{RF} matches the electron cyclotron frequency ω_c . Under this condition, free electrons are accelerated above the ionisation potential of the atoms at hand (e.g. 13.6 eV for hydrogen, 24.6 eV for helium etc.) and ignite the plasma. Besides the elementary gas ions, other, heavier particles can also be formed inside the plasma by recombination processes, for example H_2^+ and H_3^+ for hydrogen [45, 46, 83]. In the present source, a fixed RF frequency is injected via an antenna, while three couplers improve the local electric field intensity. Following equation (4.1) the frequency of $\omega_{RF} = 2.45$ GHz requires a magnetic field of $B = 876$ G. This field is achieved with a ring magnet made of a samarium-cobalt alloy ($\text{Sm}_2\text{Co}_{17}$), which has a high temperature stability up to $T = 300$ °C [87]. Figure 4.2 shows the magnetic fields measured along the source axis and marks the area where the ECR condition is fulfilled. After the plasma is formed, the charged particles are extracted via a $500 \mu\text{m}$ hole by applying an acceleration potential U_{acc} ($U_{\text{acc}} \in [500 \text{ eV}, 20 \text{ keV}]$) to the cavity. A grounded grid in front of the source ensures a well-directed beam. However, recombination processes on this grid can result in neutral atoms with energies equal to those of the charged particles. In section 5.2, we will discuss how the interferometer can be used to characterise this kind of neutral particles which originate directly from the source. Photons due to electron transitions between two states of an atom are too produced, as discussed later in section 4.5.1.

4. Experimental Setup: Characteristics and Performance

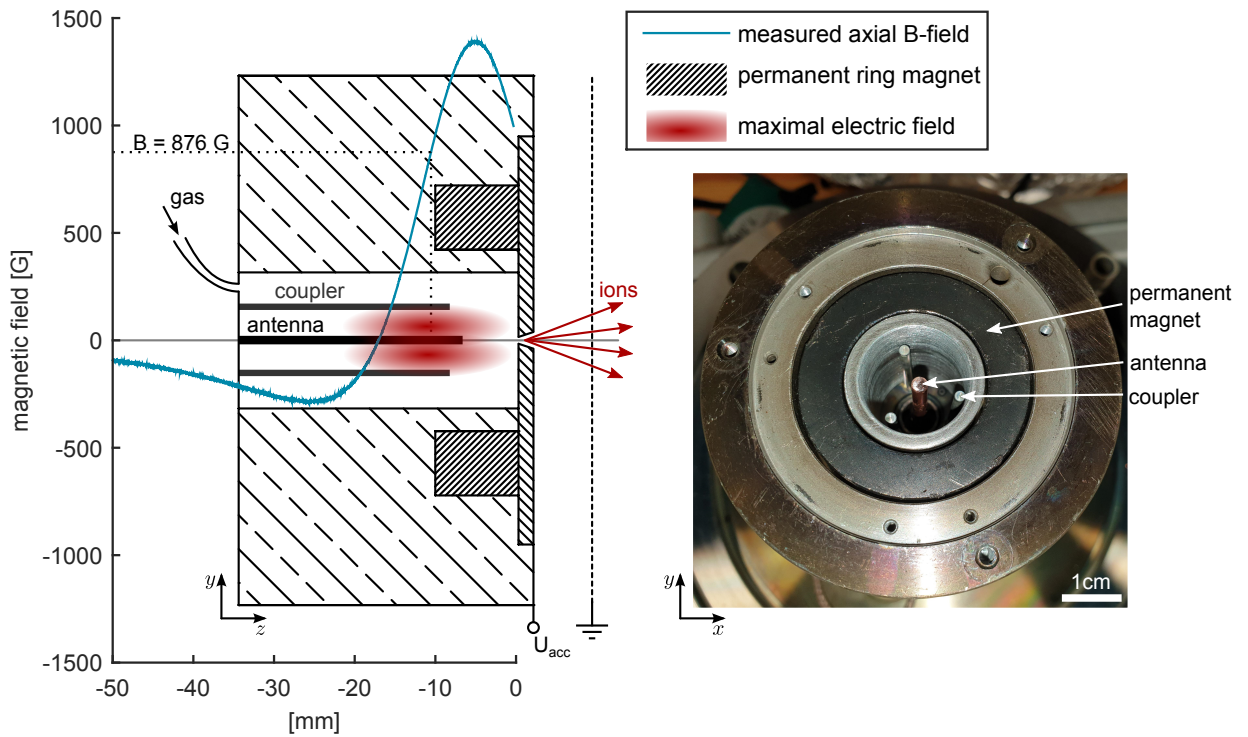


Figure 4.2.: Electron cyclotron resonance (ECR) source. Left: Schematic view of the source and the measured magnetic field of the ring magnet. The gas inside the cavity is ionized in the region where the magnetic field fulfils the ECR condition for the RF-field of the antenna ($\omega_{RF} = 2.45$ GHz, $B = 876$ G). The three couplers are used to improve the emittance of the RF antenna inside the cavity. The ions leave the source, which is on a positive potential U_{acc} , through a $500 \mu\text{m}$ hole and are accelerated towards a grounded mesh. Right: Photography of the opened source showing the ring magnet, the antenna and the couplers.

4.1.2. Wien Filter: Spectrum of the Source

In this work the ECR source is supplied with the following gases separately: hydrogen, helium, argon, krypton, and xenon. For each gas, a variety of ions are extracted. While for the noble gases corresponding multiply ionised particles occur, e.g. Xe^{n+} , the hydrogen plasma delivers protons, dihydrogen cations H_2^+ and trihydrogen cations H_3^+ . A Wien Filter can select one charged species, providing a major step towards a pure particle beam. As depicted in figure 4.3, it consists of homogeneous electric and magnetic fields applied perpendicularly to each other. Particles for which the Lorentz force equals to zero can pass through the slit at the end of the filter:

$$\vec{F}_L = q(\vec{E} + \vec{v} \times \vec{B}) \stackrel{!}{=} 0 . \quad (4.2)$$

As the velocity and the fields are perpendicular to each other, the equation is simplified to $E_x = v_z \cdot B_y$. Accelerated with the potential U_{acc} , the particle velocity is

$$v = \sqrt{\frac{2E_{\text{kin}}}{m}} = \sqrt{2\frac{q}{m}U_{\text{acc}}} , \quad (4.3)$$

and hence depends on the charge q , the mass m and the already mentioned potential U_{acc} . Combining equation (4.2) and (4.3) together, results in an expression for the electric field E_x as a function of U_{acc} and B given by

$$E_x = B_y \cdot \sqrt{2\frac{q}{m}U_{\text{acc}}} . \quad (4.4)$$

In this work, a nearly homogeneous magnetic field is generated with two permanent ferrite magnets with a magnitude of approximately $B_y = 1.2 \text{ kG}$. The electric field is supplied from two electrodes separated by a distance of $d = 30 \text{ mm}$. The desired particle can be selected by tuning the voltage between the two electrodes U_{WF} following the relation:

$$\frac{m}{q} = \frac{2B^2 d^2 V_{\text{acc}}}{U_{\text{WF}}^2} . \quad (4.5)$$

Figure 4.3 shows the measured spectrum for hydrogen and helium plasma. Both are measured on the Faraday cup behind the Wien filter. The particles, accelerated with a voltage of $U_{\text{acc}} = 2000 \text{ V}$, show clearly distinguishable peaks over the electrode voltage. Following equation (4.5) to convert the voltage to the mass-over-charge ratio in terms of the proton mass m_p and the elementary charge e reveals the particles species. For hydrogen, three well-separated peaks are visible. Consistent with the mass-over-charge ratio, they are identified as: proton, dihydrogen cations H_2^+ , and trihydrogen cations H_3^+ . For the helium spectrum only two peaks appear which indicate the two possible helium ions ${}^4\text{He}^+$ and ${}^4\text{He}^{2+}$. Note that not only is the current on the Faraday cup not directly proportional to the total particle current, but it even varies in dependence of the species. This is due to the fact that the particles hitting the Faraday cup cause emittance of several secondary electrons [88–90]. Nevertheless,

4. Experimental Setup: Characteristics and Performance

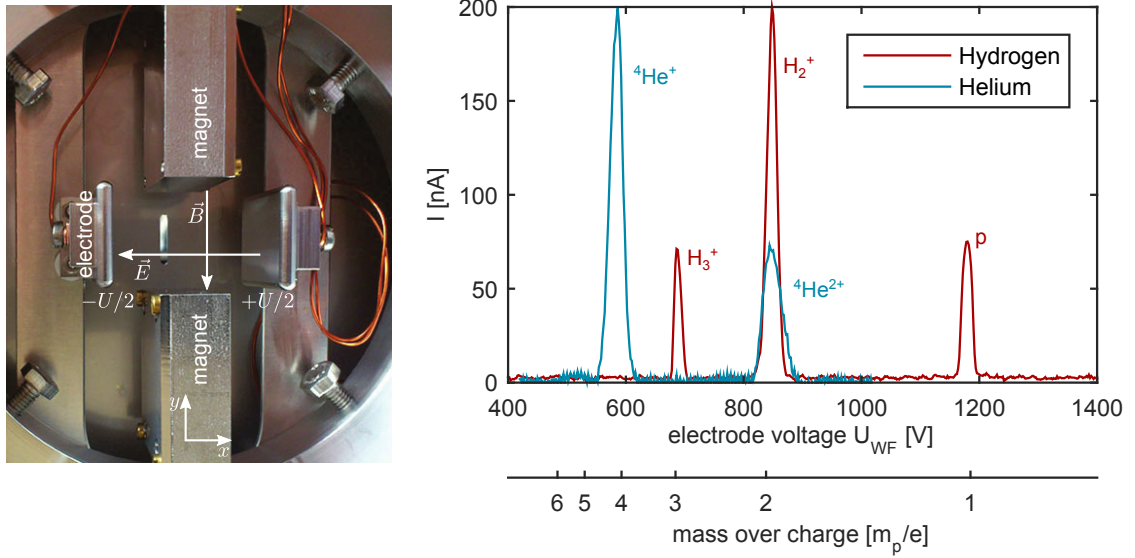


Figure 4.3.: Left: Photography of the Wien Filter. Crossed magnetic and electric fields only let pass those kind of charged particles for which the Lorentz force equals to zero. The magnetic field is generated with two permanent magnets, while the electric field can be tuned with the applied voltage U_{WF} on the electrodes. This enables to select different particles. Right: Particles spectrum of the ECR source supplied with hydrogen and helium, respectively. The current I is measured on the Faraday cup over the Wien filters electrode voltage. Converting the voltage U_{WF} to the mass-over-charge ratio in terms of the proton mass m_p and the elementary charge e reveals the particles species. For the hydrogen plasma it is proton ($m/q = 1$), H_2^+ ($m/q = 2$), and H_3^+ ($m/q = 3$); for the helium plasma ${}^4He^+$ ($m/q = 4$) and ${}^4He^{2+}$ ($m/q = 2$). (Photography: courtesy of Pierre Lansonneur.)

we can still state that the abundance of the different particle species is highly dependent on the pressure of the gas inside the ECR cavity. We observed that while in the case of hydrogen, H_3^+ is favoured for low pressure, protons are favoured for increasing pressure.

For the experiment, different particles with different acceleration voltages U_{acc} are used. The desired species is selected as described above by tuning the Wien filter voltage, following equation (4.5). At this point neutral particles coming directly from the source are still part of the beam. Hence, the subsequent experiment is placed off axis, so that the neutral particles cannot enter the three-grating setup, while the charges are bent with a pair of Helmholtz coils into the experimental zone. When neutrals are preferred or required, the Wien filter is switched off and the source is put back onto the axis, thus enabling them to reach the detector.

For heavier particles, such as argon, krypton, and xenon, the resolution of the Wien filter is not sufficient, as it scales with the inverse of U_{WF}^2 (see equation (4.5)). Hence, a small offset field generated by the Helmholtz coils and the 2D-MCP-detector (described in detail in section 4.4.1), placed one meter apart, is used spatially to separate the different ions. From this separation one can state, that heavier particles M^{n+} are ionised in the range of $n \in [1, 5]$.

4.1.3. Energy Spread

It is important to know the beam's energy spread, as it influences the visibility (compare section 3.3.2). With a fine mesh in front of the Faraday cup one can measure the energy spread of the now well-defined ion beam. Therefore, a tunable voltage U_{mesh} is applied on the mesh which hinders a particle whose energy is below $q \cdot U_{\text{mesh}}$ from reaching the Faraday cup. Scanning U_{mesh} , the intensity on the Faraday cup for a particle beam with a certain energy distribution $f(E)$ follows the integral of the distribution:

$$I(U_{\text{mesh}}) \propto \int_{U_{\text{mesh}}}^{\infty} f(E) dE . \quad (4.6)$$

Paradigmatic figure 4.4(a) shows the measured intensity as a function of the applied mesh voltage for a proton beam with an acceleration voltage of $U_{\text{acc}} = 1500 \text{ eV}$. By calculating the derivative of the measured intensity to obtain the beam's energy distribution (see equation (4.6)), it can be seen that the distribution is centred on the acceleration voltage (compare figure 4.4(b)). We find the beam's energy spread (FWHM) $\Delta E = 20 \text{ eV}$, resulting in a relative energy spread of

$$\frac{\Delta E}{E} = 1.3 \% . \quad (4.7)$$

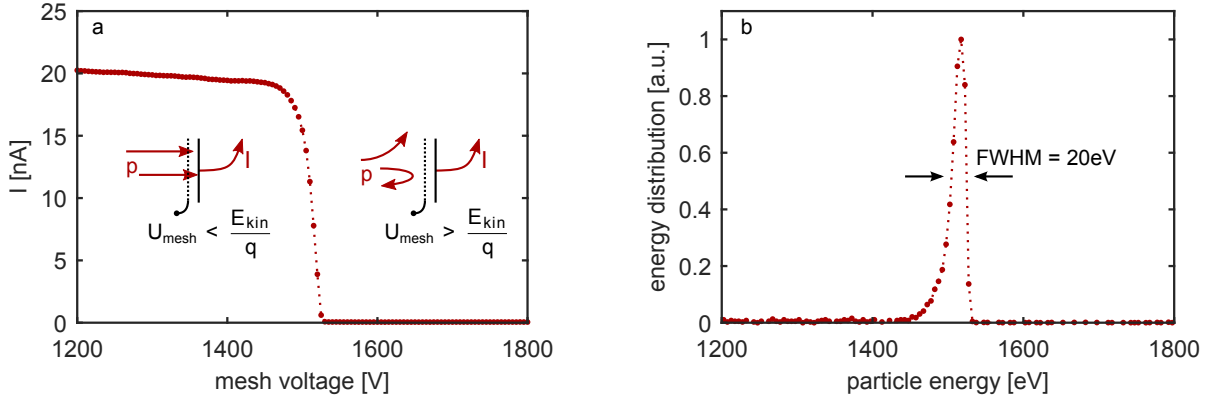


Figure 4.4.: Measuring the energy spread of a proton beam accelerated with $U_{\text{acc}} = 1500 \text{ V}$. (a) Current read on the Faraday cup as a function of the mesh voltage U_{mesh} . Particles whose energy is below the mesh potential are reflected, while higher-energy particles can pass through and are subsequently detected. The sharp drop of the intensity around 1500 V indicates that the beam's energy is 1500 eV (for a $q = 1e$ particle beam). (b) The energy spectrum of the beam is the derivative of the intensity profile in (a). It is centred around the expected mean energy of 1500 eV and has a spread (full width at half maximum) of 20 eV. The relative energy spread is therefore $\Delta E/E = 1.3\%$. (Data: [46])

4. Experimental Setup: Characteristics and Performance

4.1.4. Neutralisation Chamber: Well-Defined Neutral Particle Beam

In the previous section we saw that the source delivers different ion species with well-known energies. While for hydrogen and helium the species are easy to separate with the Wien filter, the same setup is not as effective for particles with higher mass. Nevertheless, we know that all three argon, krypton, and xenon become multiply ionised in the plasma source. This section discusses how knowledge about the source spectrum provides an important step to produce a well-defined neutral particle beam for the interferometer.

One frequently used technique to convert ion beams into their neutral equivalent is based on resonant (or near resonant) charge exchange between fast positive ions and thermal neutral particles [91]. For this purpose, the fast ion beam with the projectiles X^+ passes through a charge-exchange chamber filled with a neutral particle gas Y (the target), as shown in figure 4.5. An electron with negligible kinetic energy is transferred from the target particle to the projectile, following the equation



ΔE marks the energy difference of the ionisation potentials of the two interacting particles. In case the projectile and the target are of the same sort, ΔE vanishes and the charge transfer is called resonant. The neutralisation of the ions does not necessarily require a resonance process. Still, it is worth to minimise ΔE , as the smaller the energy difference the better is the charge exchange cross section σ . Furthermore, non-resonant conditions ($\Delta E > 0$) usually yield a broad distribution of excited states [91]. As an example, for the utilised nitrogen gas target and a proton or $^4\text{He}^+$ beam, the energy difference is $\Delta E_H = 0.9 \text{ eV}$ and $\Delta E_{He} = 10.1 \text{ eV}$, respectively. The higher energy difference for the helium ion is reflected in the smaller cross section σ as shown in table 4.1 which lists the different cross sections. In general, the charge exchange cross section is much larger than the cross sections for energy or momentum transfer. Hence, the ions can be approximated without changing their energy or direction [92]. Consequently, the energy distribution of a neutral particle beam exiting the neutralisation chamber is the same as of the incident ion beam. From the measurement in chapter 4.1.3 we can thus conclude an energy spread of less than 2% for the neutral beam. Since not all the ions are neutralized inside the chamber, the remaining charges are removed by employing an electrostatic deflector (compare figure 4.5).

The intensity of the neutral beam produced via charge exchange is determined by the charge exchange cross section σ , and by the scattering cross sections for the ions and the neutrals (σ_0, σ_+). The rate equations yield:

$$\frac{dN^+}{dz} = -N^+n\sigma - N^+n\sigma_0 , \quad (4.9)$$

$$\frac{dN^0}{dz} = N^+n\sigma - N^0n\sigma_+ . \quad (4.10)$$

N^+ and N^0 are the number of ions and neutrals at a given position z in the neutralization chamber, where n is the particle density inside the chamber and can be rewritten following

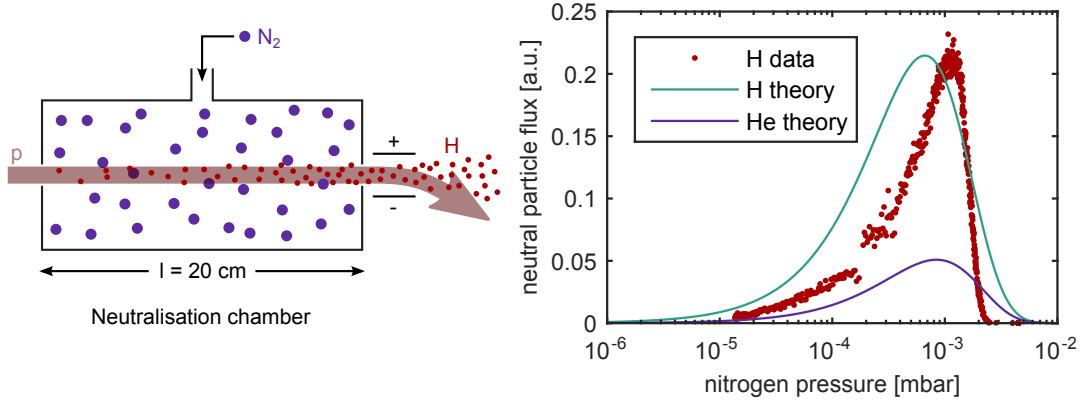


Figure 4.5.: Neutralisation chamber. Left: A schematic drawing of a setup for a fast hydrogen beam production with a neutralisation chamber. A fast proton beam with kinetic energy E_{kin} enters a charge-exchange chamber filled with nitrogen gas. As the charge exchange cross section is much larger than the cross section for energy and momentum, the resulting neutral hydrogen atoms have the same energy E_{kin} . To have a pure atom beam, the non-neutralised protons are removed with an electric field at a later stage. Right: Calculated flux for hydrogen and helium beams originating from protons and He^+ respectively using the parameters given in table 4.1. The flux is given as a function of nitrogen pressure in the chamber and compared with measurements taken with 2 keV protons. Note that a direct comparison of the theory with the experimental results is difficult, as the initial proton flux is not known and the pressure reading may be inaccurate for $p > 1 \times 10^{-3}$ mbar, due to the limitations of the utilised pressure gauge. This may explain the steep decrease in flux. Nevertheless, the shape of the data resembles the process of charged particles being converted to neutrals and scattered at higher pressure.

the ideal gas equation as

$$n = \frac{p}{k_B T}, \quad (4.11)$$

with p and T pressure and temperature inside the chamber and k_B the Boltzmann constant. Solving the differential equation yields the number of neutral particle along the beam axis z inside the gas target:

$$N^0(z) = N_0^+ \frac{\sigma}{\sigma_+ - \sigma_0 + \sigma} \exp(-n\sigma_0 z) [1 - \exp(-n(\sigma_+ - \sigma_0 + \sigma)z)], \quad (4.12)$$

where N_0^+ is the initial ion flux. For the scattering cross section σ_0 and σ_+ we can assume the colliding particles to be hard spheres with the so-called kinetic radius r . In this case, the cross section is given by

$$\sigma_{0,+} = \pi (r_1 + r_2)^2. \quad (4.13)$$

4. Experimental Setup: Characteristics and Performance

Table 4.1 lists the cross sections and the kinetic radii for hydrogen and helium.

Figure 4.5 (right) shows the pressure-dependent neutral particle flux expected after the beam has left the chamber. For this purpose equation (4.12) is evaluated for $z = 20$ cm (the length of the chamber), using the relevant cross sections. Remarkable is the shape of the curve showing two dominant principles. The increase at low pressures ($p < 1 \times 10^{-3}$ mbar) is due to conversion from charged to neutral particles. At higher pressures ($p > 1 \times 10^{-3}$ mbar) scattering of the neutral particles becomes dominant, resulting in a steep decline of the particle flux. For comparison, a measurement with a 2 keV proton beam is also shown in figure 4.5. One should treat the displayed hydrogen data with care, as the initial proton flux is not known and the pressure gauge used to measure chamber pressure shows a non-linearity in the range above 1×10^{-3} mbar, as this is the detecting limit of the gauge. Nevertheless, the experimental data resemble the overall shape of the theoretic curves.

	kinetic radius r	cross section σ with N ₂
Hydrogen	1.4 Å (H ₂)	$18.5 \times 10^{-20} \text{ m}^2$ (H ⁺)
Helium	0.91 Å (He)	$3.4 \times 10^{-20} \text{ m}^2$ (He ⁺)
Nitrogen	1.8 Å (N ₂)	

Table 4.1.: Kinetic radius and charge exchange cross section with nitrogen for different particles [93–96].

Neutralisation with Metal Target

The up to here described principle of making a pure and in energy well-defined neutral particle beam is not the only possibility to have a fast atomic beam. There are other ways how an ion can get an electron, for example via a metal target [91]. As observed before, the ECR source itself generates neutral particles. These are ions which are neutralised against a metal surface. The most probable piece of metal on which the particle can neutralise is the grounded mesh directly in front of the source. However, the wall of the vacuum chamber can also work as a neutral particle source if the charged beam is made to run against it. Nevertheless only the neutral particles directly from the mesh are used for the interferometer. Various mechanisms can be involved in the charge transfer of a metal surface to the ions. In most cases, the dominant process requires an electron from the conduction band of the metal to be transferred to a valence state of suitable energy of the ion. Furthermore, detailed experiments show that the energy of the neutral beam is proportional to the energy of the incident ions [91]. In our case one main drawback of the mesh as a neutral source becomes apparent: In contrast with the neutrals produced by the neutralisation chamber, the exact energy of the particles, is not known. Furthermore, it is in principle possible that all ions leaving the source are neutralised. In this case each species will have undergone a different neutralisation reaction and hence carry various momenta, as listed in table 4.2. In practice, this was prevented by using the Wien filter to define the desired reaction in front of the gas

target. In chapter 5.2 we will show that the use of the interferometer can help to identify which reaction process is dominant in this neutralisation process and what its energy is.

neutralisation reaction	particle momentum p
$p + e \longrightarrow \text{H}$	$p_p = p_H = \sqrt{2em_p U_{\text{acc}}}$
$\text{H}_2^+ + e \longrightarrow 2\text{H}$	$p_H = \sqrt{1/2} \cdot p_p$
$\text{H}_2^+ + e \longrightarrow \text{H}_2$	$p_{\text{H}_2} = \sqrt{2} \cdot p_p$
$\text{H}_3^+ + e \longrightarrow 3\text{H}$	$p_H = \sqrt{1/3} \cdot p_p$
$\text{H}_3^+ + e \longrightarrow \text{H}_2 + \text{H}$	$p_H = \sqrt{1/3} \cdot p_p$ $p_{\text{H}_2} = \sqrt{4/3} \cdot p_p$
${}^A\text{M}^{n+} + ne \longrightarrow {}^A\text{M}$	$p_M = \sqrt{2nAem_p U_{\text{acc}}} = \sqrt{nA} \cdot p_p$

Table 4.2.: Possible neutralisation reactions and particles' momenta compared to the protons particles momentum accelerated with U_{acc} . Different reactions are possible for the different hydrogen ions. For ions of the noble gas M with charge $q = ne$ and mass $m = Am_p$ the resulting momenta are dependent on the degree of ionisation n .

Neutralisation of Multiple Charged Ions

The question remains open how the different multiply ionised heavy particles (e.g. Xe^+ , Xe^{2+} and Xe^{n+} where n is the degree of ionisation) are neutralised. Knowing the degree of ionisation is of interest, as the particles are hardly distinguishable with the Wien filter and their resulting momentum in the neutralisation process is larger by a factor of \sqrt{n} compared to the singly ionised particles (compare table 4.2). The following two arguments may indicate whether neutral particles from singly ionised noble gas are predominant: The neutralisation of an ion with the degree of ionisation n can be expressed as a nested rate equation, since each neutralisation step from n to $n - 1$ can be separated. Therefore, for a low-pressure gas in the nitrogen target the probability of converting an ion with $n = 1$ compared to ions with $n > 1$ is much higher. Furthermore, we saw before that the charge exchange cross section decreases for increasing ΔE . For all used noble gases, it holds that ΔE increases as the ionisation energy for the n -th electron increases. This reduces the probability of a highly charged ion to be neutralised inside the chamber. Both arguments also hold for neutralisation on the metal mesh. Following these arguments, the neutral beam of the heavier particles with mass M (argon upwards) are assumed in this work to have a momentum $p = \sqrt{2eMU_{\text{acc}}}$.

4.1.5. Pinholes to Control Beam's Divergence

The contrast of the interferometric pattern does not depend only on the mass and the energy of the particles. As alluded in chapter 3.1, small misalignments of the three gratings with respect to each other significantly reduce the visibility. Besides carefully aligning the gratings (see following section) the reduction of the beam's divergence weakens the alignment requirements for the gratings. Hence, different pinholes with diameter D are placed one metre in front of the detector on a vertical translation stage. The pinhole diameter can be selected from the

4. Experimental Setup: Characteristics and Performance

following options:

$$D \in [5 \text{ mm}, 1 \text{ mm}, 200 \mu\text{m}, 100 \mu\text{m}, 50 \mu\text{m}, 10 \mu\text{m}] . \quad (4.14)$$

Correspondingly, the beam's divergence θ is given by

$$\theta = \frac{D}{1 \text{ m}} . \quad (4.15)$$

Note that for the two largest diameters, the divergence is defined by the initial divergence of the source due to its opening ($D = 500 \mu\text{m}$) and its distance to the detector ($l = 2.30 \text{ m}$).

4.2. Talbot-Lau Interferometer

The main part of the experiment is the Talbot-Lau interferometer. It is an improved version of the setup described in references [33, 34, 46]. It consists of three nanometric gratings placed equidistantly on high-precision actuators and kinematic mounts, as depicted in figure 4.6. The gratings are glued onto an L-shaped aluminium holder. The distance between the gratings is chosen to be 14 cm, thereby matching the Talbot length of a 3.6 keV hydrogen beam. With the specifications of the utilised source, this distance makes it possible, on the one hand, to detect multiple Talbot lengths for hydrogen in the quantum regime, and on the other hand, to show the classical limit, in case of e.g. xenon. In the following, the gratings are described in more detail. After that the significance of the actuators and the kinematic mounts is discussed to fulfil the high grating alignment requirements mentioned in section 3.1. A discussion on how the aforementioned requirements are achieved concludes this chapter, setting the stage for the practical application of the device to our case.

4.2.1. Gratings

The three gratings¹ are pure-transmission gratings which were photo-lithographically etched into a silicon nitride membrane [97, 98]. With a thickness of $(160 \pm 10) \text{ nm}$ and a size of $3 \times 3 \text{ mm}^2$, the grating structure is free-standing. The nanometric periodicity of 257 nm is stabilised with a larger structure oriented perpendicular to the grating bars. This so-called support structure has a periodicity of $1.5 \mu\text{m}$. The open fraction η of the nanometric as well as of the support structure varies from grating to grating and is listed in table 4.3 together with the other parameters. The inset of figure 4.6 shows an SEM² image of one grating where the nanometric slits and the support structure are clearly visible.

As the gratings are made of an insulator, they accumulate charge if exposed to an ion beam. This can result in such strong electric fields that they act even on neutral particles via induced dipole forces (compare section 3.4). To reduce the extent of this phenomenon, a metallic layer is deposited on the gratings. It has been shown that a mixture of gold (80%)

¹A special and sincere thanks to Prof. Markus Arndt from Vienna University who graciously offered us these gratings

²The image was taken at BioQuant Heidelberg with the help of the research group of Prof. Schröder. A special thanks to Anne Kast and Lisa Veith.

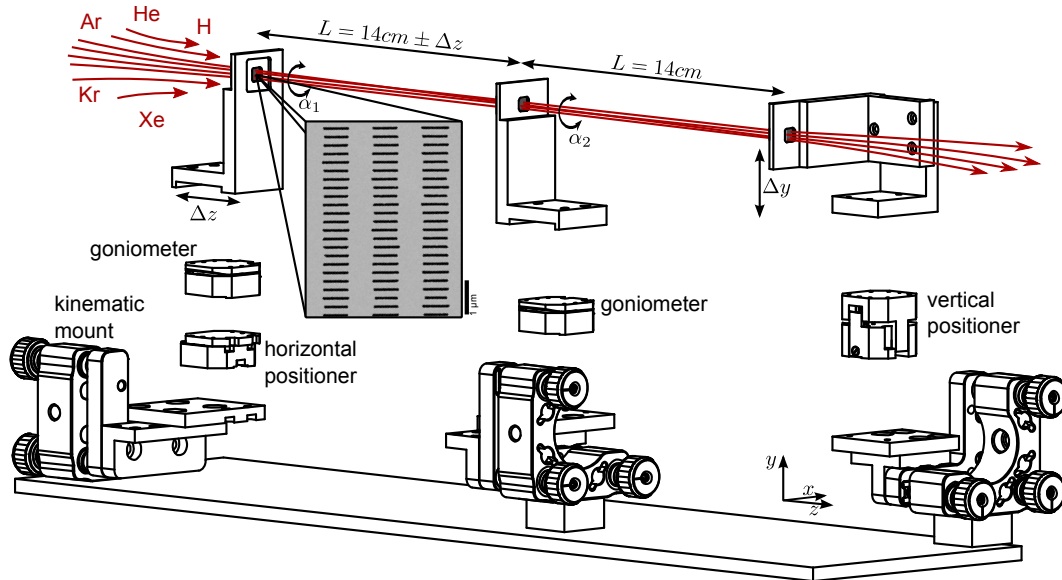


Figure 4.6.: Schematic view of the Talbot-Lau Interferometer. The three gratings are mounted on L-shaped aluminium holders which are in turn placed on different piezoelectrically-driven fine positioners. The first two gratings are each mounted on a goniometer for rotational alignment the gratings around the beam (z -)axis. Additionally, the first grating is screwed on a horizontal positioner to ensure that the gratings are equidistant to each other. The actuator for the third grating is a vertical positioner to scan the third grating. Furthermore, each unit is fixed on a kinematic mount to adjust the tilt around the x - and y -axes, and thereby ensuring the parallelism of the gratings. While the tuning of the actuators can be performed inside the vacuum with the experiment running, the kinematic mounts have to be adjusted before the experiment is started. The distance between the gratings is chosen to be $L = 14$ cm, corresponding to the first Talbot length of a 3.6 keV hydrogen beam. The small inset shows an SEM picture of the nanometric grating. Clearly visible is the periodic structure with $d = 257$ nm and the orthogonal support structure to stabilize the grating. (SEM picture courtesy of L. Veith and A. Kast.)

4. Experimental Setup: Characteristics and Performance

gratings characteristics	
material	Si ₃ N ₄
size	3 × 3 mm ²
thickness l	(160 ± 10) nm
pitch d	257 nm
open fraction η	46 %, 37 %, 37 %
pitch support structure d_s	1.5 μ m
open fraction support structure η_s	71 %, 53 %, 53 %
coating each side	20 nm AuPd (4:1)

Table 4.3.: Characteristics of the nanometric transmission gratings used in this work.

and palladium (20 %) sticks homogeneously to the silicon nitride membrane [46]. Hence, all gratings have been sputtered from both sides with a 20 nm thick layer.

The several-nanometres-thin Si₃N₄ membrane can become transparent if exposed to particles with energies above a certain limit. To estimate such limit, the transmission as a function of energy is evaluated for different kinds of particles. This is done with the computer program *Stopping and Range of Ions in Matter* (SRIM), which is a software package for calculating the transport of ions in matter, including targets with complex multi-layer configurations [73]. Designed for ions only, the software produces reliable result for any atom above 10 keV u⁻¹, as the atom will reach an equilibrium charge state within about 30 nm of the surface³. Figure 4.7 shows the results for an uncoated and coated membrane, respectively. While a pure silicon nitride membrane with the denoted thickness still lets a high fraction of hydrogen and helium through at 20 keV, the additional 20 nm of AuPd on both sides stop all particles below 20 keV. From this calculation it seems safe to use the coated gratings for the energy range below 20 keV.

4.2.2. Actuators: Aligning and Scanning the Gratings

Section 3.1 discussed the crucial influence of minor misalignments between the gratings on the visibility. To meet these requirements, all three gratings are mounted on different actuators (compare figure 4.6). The kinematic mounts correct for tilt around the x - and y -axes and have to be aligned manually outside the vacuum. The procedure for such an alignment is as follows: A He-Ne laser is coupled via a beamsplitter into a fibre. The laser beam leaving the fibre is aligned with the grating axis e.g. beam axis. As the grating itself partially reflects the laser light, the light goes back to the fibres' out-coupler. In the case the grating is perpendicular to the laser beam, adjustable with the kinematic mounts, the light will be coupled back into the fibre and detected with a photodiode on the side of the beamsplitter. As this method only works with one grating at a time, the gratings have to be sequentially mounted and aligned, the last grating as first, and ending with the first one. As the fibre's out-coupler lies

³Result of a private correspondence with James F. Ziegler, the developer of *SRIM*. At this point I want to express my thanks to him, as he has always warmly replied to my questions about *SRIM*.

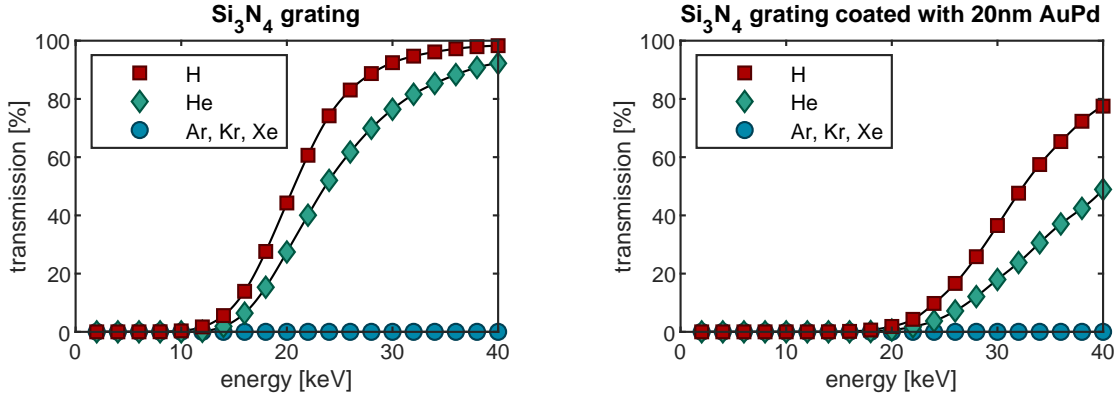


Figure 4.7.: Transmission of different particles through a pure 160 nm thin Si_3N_4 membrane (left) and a membrane coated from both sides with a 20 nm thick layer of gold (80 %) and palladium (20 %). For the second case the gratings act as true transmission gratings for energies below 20 keV.

more than 150 cm away from the first grating and has a fibre core of 200 μm , the alignment reaches a precision better than

$$\Delta\beta_x = \Delta\beta_y \lesssim 200 \mu\text{rad} . \quad (4.16)$$

This is equivalent to a z -displacement of less than 1 μm over the grating size and hence fulfils the criterion of $\Delta\beta_x \leq 30 \text{ mrad}$ and $\Delta\beta_y \leq 43 \text{ mrad}$ (compare table 3.1).

Compared to the tilt around the x - and y -axes, the rotational alignment around the beam axis (z -axis) is much more sensitive ($\Delta\alpha \leq 560 \mu\text{rad}$, compare table 3.1), as it governs the moiré periodicity (compare equation (2.35)). Therefore, the first two gratings are screwed on a goniometer⁴ with an angular resolution of 1.7 μrad [99]. Although the actuator can be tuned while the experiment is running, it is desirable to have a rough idea of the rotational alignment with respect to the last grating. A complete lack of pre-knowledge for this alignment would rule out the possibility of finding the required position, as both goniometers with an angle range of 115 mrad each have to match on 0.56 mrad to the ideal position. To pre align the gratings we use the general form of the grating equation

$$\sin(\theta_n) - \sin(\beta) = n \cdot \frac{\lambda}{d} , \quad (4.17)$$

where β is the angle of incidence and θ_n the angle of the n -th diffraction maximum. As the left side of equation (4.17) cannot exceed the value of 2, the wavelength λ of the laser to align the gratings has to be chosen correspondingly. With a blue laser diode ($\lambda = 405 \text{ nm}$) and the given periodicity of $d = 257 \text{ nm}$, it is possible to observe the first diffraction order as $405/257 = 1.58 < 2$. Therefore, the incident angle has to be set around 60°. Note that due to the construction of the setup we use the diffraction order of the back reflection. The blue

⁴ANGt101 RES from attocube [99]

4. Experimental Setup: Characteristics and Performance

laser light coming from the top ($\beta = 60^\circ$) is reflected and diffracted into the first order going to the top as well ($\theta_{-1} = 46^\circ$). The absolute position of the diffraction spot is measured up on the ceiling 2.5 m above the experiment. Small rotations of the grating directly translate into a movement of the spot on the ceiling. To align all three gratings with respect to each other, we start with the third one, which is rotationally fixed, and mark the position of the diffraction spot. Then, the whole experiment is moved on a high-precision translation stage $L = 14$ cm upwards, so that the second grating is at the position of the previous one, while the laser beam was locally fixed. Now, the rotational alignment for the second grating can be performed. Then, the setup is moved a second time to repeat the alignment procedure already used for the first grating. The appearance of fringes after the alignment procedure for the running experiment shows that the achieved alignment was significantly better than $\Delta\alpha_{1,2} \ll 100 \mu\text{rad}$.

The last alignment requirement is the z -position of the three gratings with respect to each other. With a sensor resolution of 200 nm [99], the horizontal actuator⁵ beneath the first grating enables to keep the gratings equidistant. With the above-mentioned alignment procedure for the angle alignment it is also possible to guarantee that the gratings are roughly equidistant, as a horizontal grating displacement translates into a displacement of the diffraction spot perpendicularly to the displacement of the rotation. The results and on-time corrections in the experiment show that this alignment was only precise up to $\Delta z = 200 \mu\text{m}$ and, hence was above the critical value of $128 \mu\text{m}$ for a 1 mrad beam (compare table 3.1).

The last grating is placed on a vertical positioner⁶ with a sub-nanometre positioning resolution [99] for scanning the last grating as described (compare section 2.4).

4.3. Magnetic and Electric Shielding

A field-free environment between the three gratings is crucial for avoiding decoherence effects and pattern distortions within the interferometer, especially while working with charged particles (compare section 3.3). Since our experimental device is designed to be used with both, atoms and ions, it is of utmost importance to set up the environment such that it be suitable for both, without having to interfere with it. In order to ensure the surrounding fields fall below the critical values of $E_{\text{crit}} = 131 \text{ mV m}^{-1}$ and $B_{\text{crit}} = 9.5 \text{ mG}$ (see table 3.3), the interferometer is placed inside a magnetic shielding while the gold-coated gratings and small copper tubes between the gratings work as a Faraday cage.

4.3.1. Mu-Metal to Shield the Earth's Magnetic Field

As indicated in figure 4.8 the interferometer is placed inside a cylindrical mu-metal shield to reduce the effects of magnetic fields, the predominant of which is the Earth's magnetic field. Mu-metal is a special alloy of nickel (77 %), iron (16 %), copper (5 %) and chromium (2 %), whose relative permeability can reach values higher than $\mu_r = 20 \times 10^3$ [100]. Such high permeability leads to the concentration of the magnetic flux into the material, resulting in a

⁵ANPx101 RES from attocube [99]

⁶ANPz101 RES from attocube [99]

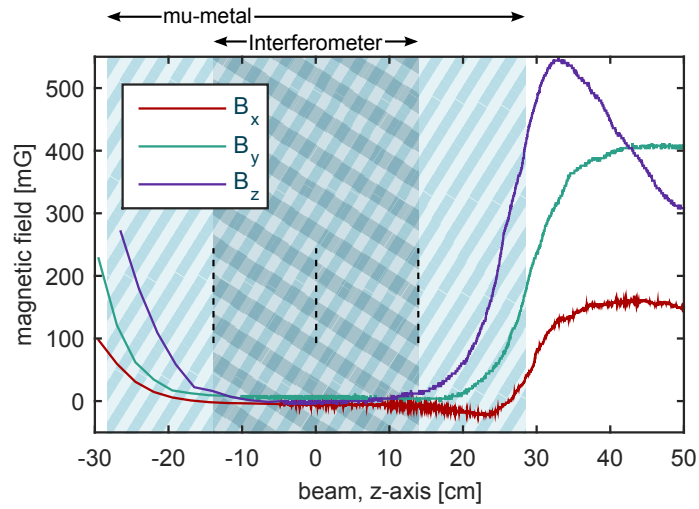


Figure 4.8.: Magnetic field along the beam axis inside a cylindrical mu-metal shield with a length of 56 cm and a diameter of 18.6 cm. The shaded area marks the position of the interferometer inside the mu-metal with respect to the measured data. The ambient field of $|\vec{B}| = 520$ mG is shielded inside the experimental area in all three axes below the detection limit of the fluxgate magnetometer, i.e. $|B_{x,y,z}| < 5$ mG. This condition is sufficient to neglect the influence of magnetic fields inside the interferometer.

lower field inside a tube of mu-metal. Typical shielding factors for such geometries can reach 1000 or more [101].

In our case, the cylindrical mu-metal shield⁷ is 56 cm long with a diameter of 18.6 cm. The 28 cm long interferometer is centrally placed inside the tube to match the best conditions. To demonstrate the efficiency of this monolayer mu-metal shield, figure 4.8 shows the different magnetic field components along the beam axis measured with a fluxgate magnetometer. The ambient magnetic field of $|\vec{B}| = 520$ mG is attenuated around the gratings in all three axes below the value of $|B_{x,y,z}| < 5$ mG, which is the detection limit of the sensor. According to calculations whose results are stated in table 3.3, this value is sufficient to neglect the influence of magnetic fields in the interferometer even for a 100 eV proton beam with a 1 % energy spread.

4.3.2. Faraday Cage to Avoid Influence of Stray Electric Fields

If the system is tested with charged particles, insulators within the setup can accumulate permanent charge, causing stray electric fields. This will heavily influence the performance of the interferometer not only with charged particles themselves but also with neutral species, as induced dipole interaction will occur. Hence, it is important to minimise insulating materials inside the interferometer and shield residual electric fields along the beam path with a Faraday cage.

As shown in figure 4.9(a), the Faraday cage is constructed of coated metallic gratings and two

⁷from Magnetic Shield LTD [101]

4. Experimental Setup: Characteristics and Performance

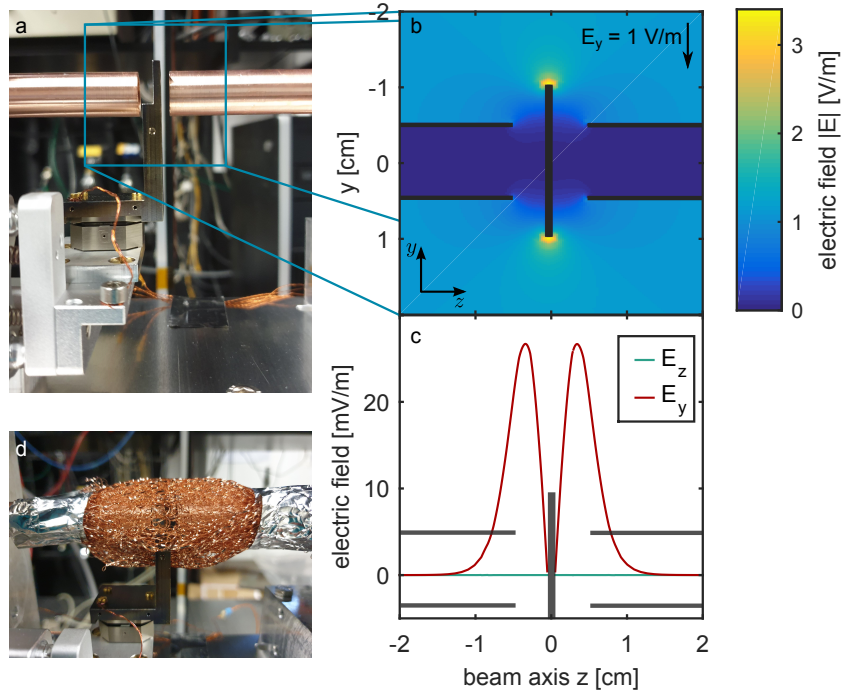


Figure 4.9.: Electric shielding using the principle of a Faraday cage. (a) The coated metallic grating and the copper tubes build a Faraday cage to shield stray electric fields caused by charged insulators. (b) Electric field distribution simulated for an ambient field of $E_y = 1 \text{ V m}^{-1}$. The shielding effect of the copper tube is clearly visible, while the gap between the grating and the tubes causes the electric field to penetrate the beam path. (c) Closer look at E_y and E_z in the middle of the beam path. Significant is the residual E_y field due to the gap. (d) Further shielding improvement with a fine and flexible copper mesh that does not disturb the grating's movement.

13 cm long and 1 cm wide copper tubes. With the principal of finite elements we estimate the effectiveness of this Faraday cage. The simulation is performed with Matlab for an ambient field of $E_y = 1 \text{ V m}^{-1}$ (figure 4.9(b)). Figure 4.9(c) shows the profile of $E_{y,z}$ along the axis of the interferometer (centre of the tube) and clearly reveals the effect of the small, 5 mm gap between the grating and the tube. At this point, ambient electric field penetrates the beam path, causing a residual vertical field up to 30 mV m^{-1} . To minimise this effect further a fine and flexible copper mesh is laid around this gap in such a way that the gratings' movement is not hindered (see figure 4.9(d)). Inside the copper tube an electric field of $8 \mu\text{V m}^{-1}$ can be expected, which is not due to insufficient shielding but rather due to a surface electron layer on the inside of the tube's wall [102].

4.4. Detection System and Data Acquisition of Fringe Pattern

The fringe pattern formed after the interferometer is detected with a combination of a two-stage microchannel plate (MCP), a phosphor screen and a camera (figure 4.10). The detection

4.4. Detection System and Data Acquisition of Fringe Pattern

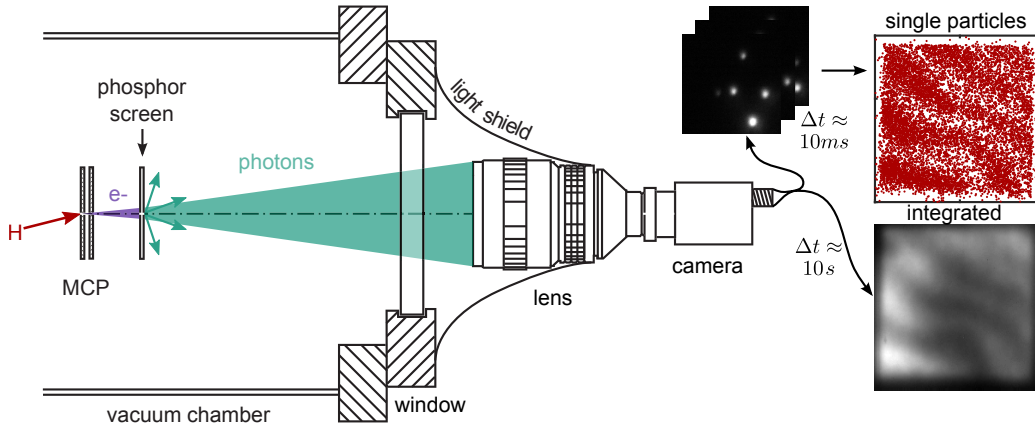


Figure 4.10.: Schematic view of the detection system with two different acquisition modes. The detection part consists of two microchannel plates (MCP), a phosphor screen inside of the vacuum chamber, and a camera outside of the vacuum chamber. Particles hit the MCP and generate a cascade of up to 1×10^6 secondary electrons. When the electron cloud impacts on the phosphor screen isotropically, green light is emitted which is detected outside of the vacuum chamber with the camera. Dependent on the electron gain of the MCP and the camera's exposure time either single-particle impact or the whole pattern integrated at once can be resolved. Images showing single particle hits are further analysed to retrieve the particles' position with a precision up to $10 \mu\text{m}$. While the integrated picture needs seconds to display the pattern, single-particle detection requires thousands of pictures to obtain the pattern. Nevertheless this results in a better resolution of the fringe pattern and its visibility than the procedure of integrating all impacts at once.

setup is sensitive to a wide range of particles, for instance energetic or metastable atoms, charged particles, or high-energy photons. It is capable of resolving single-particle impacts in two dimensions, as well as the entire fringe pattern at once, depending on the camera exposure time and the MCP adjustments. To obtain the crucial information, the visibility of the pattern, two different computer based algorithms are used (single particles detection versus continuous picture).

The current section firstly explains the principle and specifications of the hardware in order to show secondly the different computer-based methods to obtain the visibility of the periodic pattern. It concludes with a comparison of the two detection principles.

4.4.1. Microchannel Plate - Phosphor Screen - Camera

Microchannel Plate

A microchannel plate is a 2D detector with single-particle resolution and sensitivity to a broad selection of particles, such as protons, H_2^+ , H_3^+ , all ions of noble gases, and high-energy photons ($\lambda \in [1 \text{ nm}, 150 \text{ nm}]$) [103–107]. Neutral atoms such as hydrogen, helium, argon, xenon, or krypton, can also be detected, provided they have sufficient kinetic energy ($> 500 \text{ eV}$) [108]. The principle of an MCP is based on $1 \times 10^4 - 1 \times 10^7$ miniature electron multipliers, i.e.

4. Experimental Setup: Characteristics and Performance

channels which are closely packed and parallel to each other [106]. An incident particle produces secondary electrons if it hits the surface of a channel. A voltage is applied along the channel to accelerate the electrons which then produce a cascade of electrons while hitting the channel wall. To increase the efficiency, two MCPs with slightly tilted channels ($\alpha = 12$ deg) are stacked onto each other in a chevron configuration. For an applied voltage of $U_c = 2$ kV along the two plates, a typical electron gain of 5×10^6 [109] is expected. Table 4.4 gives an overview of the MCP characteristics used in this work⁸.

MCP characteristics	
active diameter	25 mm
thickness	$0.48 \text{ mm} \pm 0.03 \text{ mm}$
channel pitch size	$12.5 \mu\text{m}$
channel pore size	$10 \mu\text{m}$
bias angle	$12^\circ \pm 1^\circ$
open area ratio	min. 60 %
double MCP gain at $U_c = 2$ kV	5×10^6

Table 4.4.: Characteristics of the MCP used in the experimental setup [109].

Phosphor Screen

The avalanche of electrons is accelerated to 4 keV towards a phosphor screen. The phosphor screen is a glass plate coated with a thin layer ($\approx 6 \mu\text{m}$) of fluorescent material ($\text{Gd}_2\text{O}_2\text{S:Tb}$) and of a conducting material (indium tin oxide) to avoid accumulation of charge. The energy of the 4 keV fast electron cloud impinging on the screen is absorbed and re-emitted isotropically as visible light ($\lambda \approx 545 \text{ nm}$) with a conversion efficiency of 100 photons per electron. The decay time of 2.6 ms limits the speed of the image acquisition.

Camera

A camera⁹ outside of the vacuum chamber images the backside of the phosphor screen. For sufficiently low particle flux, exposure time of the camera set to the order of $\mathcal{O}(10 \text{ ms})$, and the MCP's gain at maximum (i.e. $U_c = 2$ kV), the obtained image shows clearly distinguishable single impacts on the detector, as can be seen in figure 4.10. For a low MCP gain (i.e. $U_c = 1.5$ kV) and long exposure time ($\mathcal{O}(10 \text{ s})$), the recorded images display the entire fringe pattern at once. While in the second case the data acquisition allows an on-time interpretation of the experiment, in the first case several thousand images with single-particle impacts with post-processing are required before a conclusion on the system can be made. Nevertheless, we will see in the following that taking single-particle images significantly improves the resolution.

For an optimal visualization of the pattern, the camera is focused to the area where the

⁸MCP from GIDS-GmbH [109]

⁹Mako G-234 from Allied Vision [110]

fringes appear. The conversion rate of the images, calibrated with a millimetre scale, is found to be

$$1 \text{ px} \hat{=} 11.4 \mu\text{m}. \quad (4.18)$$

4.4.2. Single-Particle Detection: High Spatial Resolution

The detection system is able to reveal single-particle impacts. To do so, the flux and shutter time of the camera have to be reduced while the MCP gain is at maximum, so that the particles are imaged one by one. A particle hit results in a 2D Gaussian-shaped intensity modulation over several pixels ($200 \times 200 \mu\text{m}^2$) on the camera. With such images the coordinates of the impact are retrieved on the detector for each particle with a sub-pixel resolution. In the following, the algorithm used to extract the coordinates for each particle is explained and subsequently the characteristics of detecting particles in such a way are presented, including the resolution and statistics of such impacts.

Algorithm to Retrieve Coordinates of Single-Particle Impact

A typical dataset of a 15 minute long measurement consists of approximately 10 000 images with each showing a few single-particle impacts. A computer-based algorithm is used to analyse such images in order to find the position of the particles in a reasonable time. Similar obstacles have to be faced in many fields of physics such as image analysis of localization microscopy where the centre of an airy disk in an image has to be found [111], or in photoelectric astrometry to obtain the precise location of celestial objects in a noisy image [112, 113]. The methods range from fitting a 2D Gaussian to merely taking the position of the brightest pixel [46]. While the first method is time-consuming, the second lacks precision. The algorithm utilised in this work is based on the principle of finding the unique point where the weighted relative position of the distributed pixels sums to zero. The analysis time for such an approach is in the order of the image acquisition time, whereas the accuracy is better than the pixel size and overcomes the internal resolution limit of the MCP itself.

The algorithm is structured as follows:

- All pixels with intensities below a certain threshold are suppressed. The threshold value is put to 10 % of the maximum value possible for the image's class. This eliminates most of the background noise in the images.
- The remaining pixels are grouped with their neighbouring pixels. All groups that overcome a threshold size of more than 50 px are taken into account as particle hits. Not only does this step separate single hits in one picture, but it also removes hot pixels. The outcome of this operation is a $3 \times N$ -matrix for each detected impact, where N is the number of relevant pixels for that impact characterised with the x - and y -position of the pixel and its intensity I .
- For each pixel group the mean location of the pixel distribution is calculated as follows

4. Experimental Setup: Characteristics and Performance

(centre of mass detection):

$$\vec{P} = \begin{pmatrix} X \\ Y \end{pmatrix} = \frac{1}{\sum I} \cdot \sum_{i=1}^N I_i \begin{pmatrix} x_i \\ y_i \end{pmatrix}. \quad (4.19)$$

- In the rare case of two particles impinging on the detector in close proximity to each other, the previous steps do not separate them. In such a case, \vec{P} gives the direction vector between the two impacts. To avoid this, variance $\sigma_{x,y}^2$ of the pixel distribution is calculated:

$$\begin{pmatrix} \sigma_x^2 \\ \sigma_y^2 \end{pmatrix} = \frac{1}{\sum I} \cdot \sum_{i=1}^N I_i \left(\begin{pmatrix} x_i \\ y_i \end{pmatrix} - \vec{P} \right)^2. \quad (4.20)$$

If σ exceeds a threshold of $100 \mu\text{m}$, the pixel group is not interpreted as a single-particle event and is hence taken as invalid. The limit of $100 \mu\text{m}$ was empirically deduced, testing the algorithm with well-understood data samples.

Using this algorithm we will see in the following that the accuracy of the position is not limited by the algorithm itself, but more by the working principle of the MCP.

Statistics and Resolution of Single-Particle Impacts

The above-presented algorithm allows to study the statistics of the impacts and enables a closer look at the internal resolution limit of the detector.

We start with the dark count rate of the detector. The dark counts originates primarily from the residual gas in the chamber and cosmic rays hitting the MCP. Running the MCP without beam exposure and detecting the particles for four days reveals a significant low dark count rate of

$$R = (1.3 \pm 0.1) \times 10^{-3} \text{ counts s}^{-1} \text{ cm}^{-2} \quad (4.21)$$

with the impacts distributed uniformly over the whole detector area (compare figure 4.11(b)). Compared to an average observed flux of approximately $2 \times 10^3 \text{ counts s}^{-1} \text{ cm}^{-2}$, during a regular measurement the dark counts are negligible.

The dark counts, as well as the particles originating from the source may be argued to follow the Poisson distribution, as can be seen in figure 4.11(a). The Poisson distribution expresses the probability P of a given number of events N occurring in a fixed interval of time (in our case the camera exposure time), and is given by

$$P(N) = e^{-\lambda} \frac{\lambda^N}{N!}. \quad (4.22)$$

Constraints for the Poissonian statistics are that the events have to be independent from one another and have a constant rate of occurrence λ over time. The good agreement of theory and experimental data (figure 4.11(a)) indicates that indeed the dark count rate as well as the

4.4. Detection System and Data Acquisition of Fringe Pattern

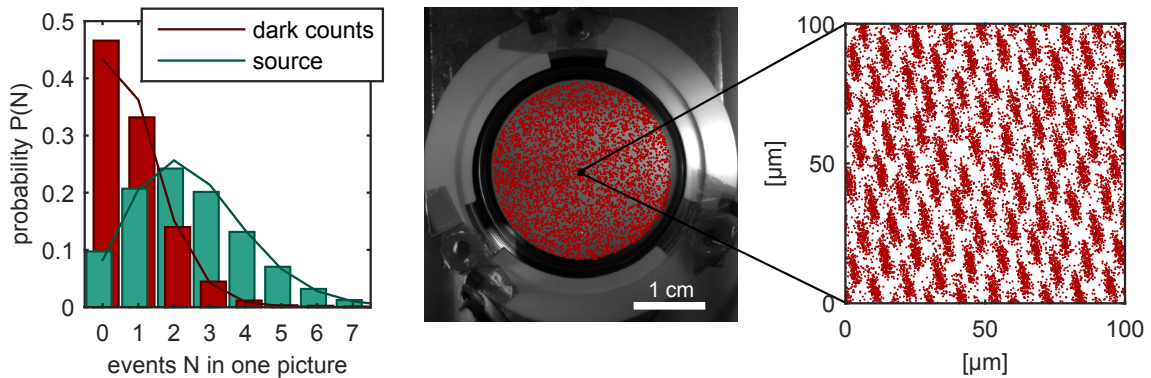


Figure 4.11.: Detecting single-particle impacts: (a) The detected particles in one camera image for dark counts as well as for the particles from the source following the Poisson distribution. (b) Image of the backside of the phosphor screen. The dark counts (red dots) are distributed equally over the entire surface. (c) Zoom in on a $100 \times 100 \mu\text{m}^2$ square with multiple particles detected. The single channels of the MCP are resolved with a pitch size of $12.5 \mu\text{m}$. This gives the internal resolution limit of the detection system.

source have a constant particle rate λ and all particles are independent. The particles could not be taken as independent, if, for example, the MCP had a dead time after each particle's arrival or if the algorithm invalidated large quantities of particles so that for example the 0-particle images would rise in probability.

Analysing around 10 000 particle impacts on a $100 \times 100 \mu\text{m}^2$ square reveals a honeycomb-like structure with a pitch (distance between sphere centres) of $12.4 \mu\text{m} \pm 0.2 \mu\text{m}$, which is consistent with the MCP channel pitch given in table 4.4. It is remarkable that the resolution of the camera and the algorithm is so high that the individual channels of the MCP can be resolved and hence the exact channel which the incident particle hit determined. Therefore, the precision of a particle impact is the channel pore size, amounting to $10 \mu\text{m}$. Note that due to the open area ratio of the MCP, 40% of the particles are not detected, as they do not hit any channel. Furthermore, detecting the single channels of the MCP reveals defects in the MCP's honeycomb structure and shows $0.6 \times 0.6 \text{ mm}$ large channel patches which are most likely a result of the production mechanism of the detector.

Since the measurement aimed at resolving the channel structure took more than three days, it indicates a high rigidity of the camera outside of the vacuum with respect to the MCP and phosphor screen. The drifts of these two components with respect to each other have to be sufficiently smaller than the channel pitch size.

Summarising the results, the single-particle detection and the algorithm to retrieve the position of the impacts have been shown to have a low dark count rate, high spatial resolution, and long time stability. The weakness of the technique is a long acquisition time ($\approx 10 \text{ min}$) for collecting enough particles to generate the pattern. In table 4.5 a summary of the most important characteristics of detecting single particles are listed.

4. Experimental Setup: Characteristics and Performance

characteristics: single-particle detection	
dark count rate	$(1.3 \pm 0.1) \times 10^{-3} \text{ counts s}^{-1} \text{ cm}^{-2}$
statistics	particle hits following Poisson distribution
precision of particle impact	$10 \mu\text{m}$
high rigidity of detection system	drifts $\ll 12.5 \mu\text{m}$ in 3 days
time for one dataset	$\approx 10 \text{ min}$

Table 4.5.: Characteristics of measuring with single-particle detection.

4.4.3. The Rayleigh Test: Efficient Way of Receiving Pattern's Period, Orientation, and Visibility

The previous section gave a list of the particle impacts with their respective x - and y -coordinates. The crucial information we have to retrieve from these data is the visibility of the periodic fringe pattern depicted by these coordinates. A simple sinusoidal fit may be a sufficient tool for obtaining this information, if the orientation angle and periodicity of the pattern are known. As these depend on the grating alignment, which we know only to a certain limit (see chapter 4.2.2), they are extracted from the dataset.

The so-called Rayleigh test is an effective tool from the field of directional statistics [114–116] to test for non-uniformity of a set of unbinned points on a circle and hence can be adapted to look for periodic patterns in a 2D plane. First described by Lord Rayleigh in 1919 [117] it finds nowadays a number of applications in different fields of physics. It is used not only to find a periodic signal in the scattered (x, y) -positions of different particles [19, 34, 44] – as it will be used in the following – but also to look for periodicity in γ - or X -ray emission from pulsars [118–120], or to study the magnetic compass navigation of robins in the field of ornithology [121, 122].

As the Rayleigh test indicates the non-uniformity of points on a circle, the (x, y) -data first have to be mapped onto a ring. To do this, we choose projection angle α_{test} and period d_{test} (identical with the circumference of the circle) under which we want to apply the Rayleigh test to verify whether our data exhibit in a periodic structure. The new polar coordinates θ_i for particle i are hence expressed by the following two steps:

$$\text{projection: } x'_i = x_i \cdot \cos(\alpha_{\text{test}}) + y_i \cdot \sin(\alpha_{\text{test}}) , \quad (4.23)$$

$$\text{mapping onto a circle: } \theta_i = \frac{2\pi}{d_{\text{test}}} \cdot x'_i . \quad (4.24)$$

The actual non-uniformity test in the new coordinate system is defined [114] as

$$Z^2 = \frac{2}{N} \left[\left(\sum_{i=1}^N \cos(\theta_i) \right)^2 + \left(\sum_{i=1}^N \sin(\theta_i) \right)^2 \right] , \quad (4.25)$$

where N is the total number of particles. The higher Z^2 , the more likely it is that a periodic pattern is present under the test parameter $(\alpha_{\text{test}}, d_{\text{test}})$.

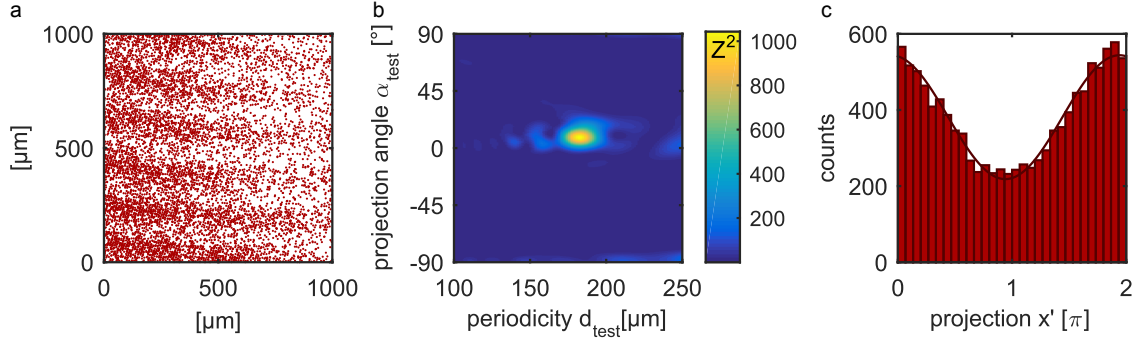


Figure 4.12.: Rayleigh test applied on xenon data to retrieve the pattern's visibility. (a) Single xenon impacts already reveal a periodic fringe pattern slightly rotated around the horizontal axis (0°). (b) Z^2 of the Rayleigh test is computed for different orientation angles α_{test} and periodicities d_{test} . A clear maximum appears at $\alpha_{\text{test}} = 6.6^\circ$ and $d_{\text{test}} = 184.7 \mu\text{m}$. (c) Mapping the dataset with the retrieved parameters onto one period. With a sinusoidal fit the visibility ν is obtained (here: $\nu = 43\% \pm 1\%$).

In order to get the information about a periodic pattern from our data, we have to find parameters $(\alpha_{\text{test}}, d_{\text{test}})$ which maximise Z^2 . Figure 4.12 shows the result of the Rayleigh test when applied on real xenon data from the interferometer for a wide parameter range (orientation angle $\alpha_{\text{test}} = (-90^\circ, \dots, 90^\circ)$, periodicity $d_{\text{test}} = (100 \mu\text{m}, \dots, 250 \mu\text{m})$). A prominent maximum of $Z_{\text{max}}^2 = 1043$ appears at $\alpha_{\text{test}} = 6.6^\circ$ and $d_{\text{test}} = 184.7 \mu\text{m}$.

With this information, the visibility is retrieved in the next step: The dataset is mapped and binned with the obtained parameters onto one period d_{test} . A sinusoidal function is approximated to these bins with the method of least squares, which optimises the phase ϕ , the amplitude A , and the offset C of the sine function, while the period is held constant. The visibility ν is subsequently calculated as $\nu = A/C$.

The Rayleigh Test Performance

To estimate the uncertainties of a single measurement, we use simulated datasets as an input for the Rayleigh test and sinusoidal fit.

The path towards such an estimation is the following:

- Fringe patterns are generated on a $1 \text{ mm} \times 1 \text{ mm}$ square with a known orientation angle, periodicity and visibility, while ensuring that all parameters are similar to the experimental conditions. The fringe pattern is created with N particles probabilistically distributed over the sample size.
- The period, angle, and visibility are re-estimated by means of the Rayleigh test and the sinusoidal fit.
- Both steps are repeated 1000 times for each configuration (ν/N) to enable approximating the standard deviation.

4. Experimental Setup: Characteristics and Performance

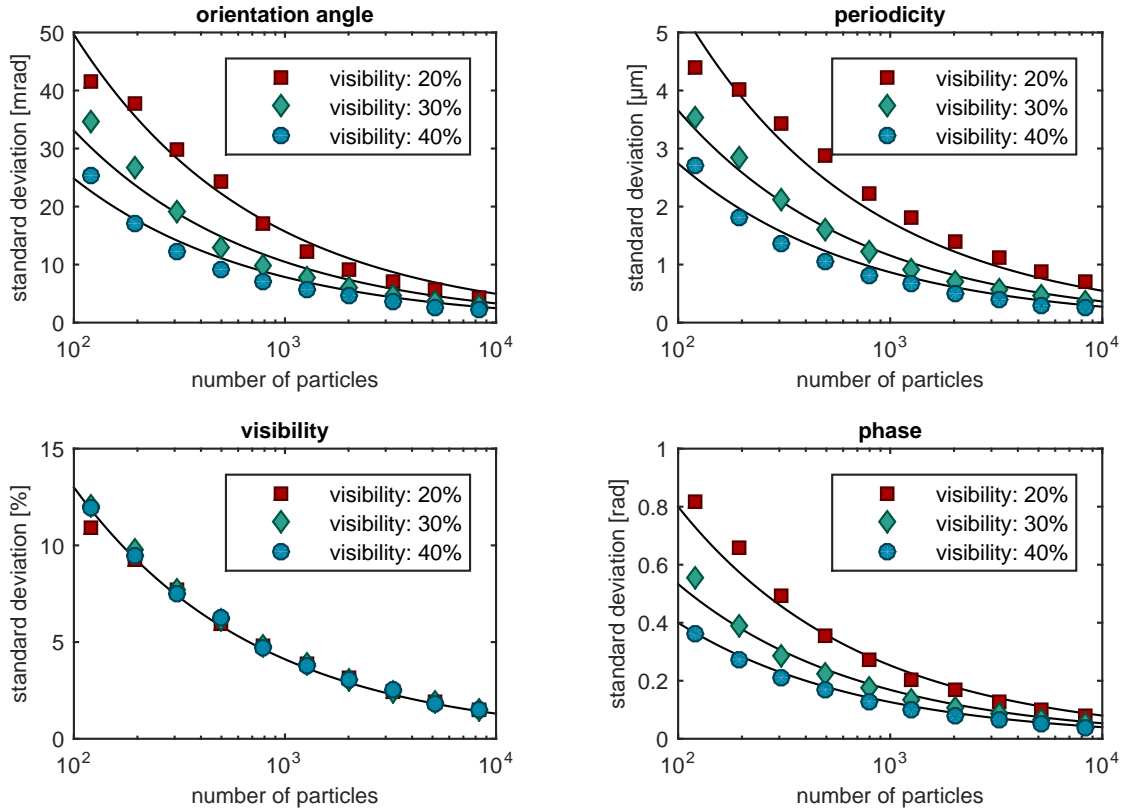


Figure 4.13.: Performance of the Rayleigh test and the sinusoidal fit. The standard deviation for the different measurands (orientation angle α , periodicity d , visibility ν , phase ϕ) are estimated with simulated datasets for different visibilities and particle numbers. In all cases a $1/\sqrt{N}$ dependence is observed (black solid line). Furthermore, for all cases except for the visibility, the error is inversely proportional to the visibility of the pattern.

4.4. Detection System and Data Acquisition of Fringe Pattern

- Since even small changes in the periodicity and angle change the phase, both the periodicity and the angle have to be fixed while the phase is being analysed. Therefore the standard deviation of the phase is estimated with the known values of period and orientation for the fit. This is repeated 1000 times with randomised samples as well.

The results are shown in figure 4.13, giving the standard deviation for the different parameters dependent on the particle number and the visibility of the given fringe pattern. Due to Poissonian statistics for all four parameters the statistical error decreases with \sqrt{N} . Furthermore, the error in the orientation angle, periodicity and phase is inversely proportional to the visibility of the pattern itself. The error for all four of them is therefore found to be:

$$\Delta\alpha = \frac{1}{\nu\sqrt{N}} \cdot 99(4) \text{ mrad} \quad (4.26)$$

$$\Delta d = \frac{1}{\nu\sqrt{N}} \cdot 11.0(5) \mu\text{m} \quad (4.27)$$

$$\Delta\nu = \frac{1}{\sqrt{N}} \cdot 1.31(3) \quad (4.28)$$

$$\Delta\phi = \frac{1}{\nu\sqrt{N}} \cdot 1.6(1) \text{ rad} . \quad (4.29)$$

The proportionality factor is retrieved from the data points via the least-square method. However, due to time constraints, it is not possible to repeat the measurement one thousand times. But if the orientation and periodicity of the fringe pattern have once been found, the error in the visibility and phase can also be estimated with a re-sampling technique. To do this, the sinusoidal fit is repeated several times, while the bin counts on the histogram are randomised. The randomisation also follows Poissonian statistics, as described in section 4.4.2. Comparing the statistical error retrieved by the re-sampling technique with the revealed dependence in equations (4.28) and (4.29) shows a difference which is within the error bar of the proportionality factor. This indicates the equivalence of both methods.

4.4.4. Integrated Data Acquisition: Saving Time

Previous chapters examined the analysis of the fringe pattern via the detection and processing of single-particle events. The single-particle detection was characterised by the high precision of the impact coordinates, but required a long acquisition time in order to have enough statistics to enable a quality assessment of the pattern formation. This section presents a different approach, taking images with a long exposure time ($\mathcal{O}(10 \text{ s})$), accumulating thousands of particles in one picture. Furthermore, the MCP gain is reduced to increase the number of particles in one image without saturating the camera. This makes it impossible to separate single events but enables rapidly to intervene in the system, for instance by changing the grating alignment parameters. A typical fringe pattern taken with this approach is shown in figure 4.14(b).

As stated before, the shape of a single-particle event resembles a Gaussian distribution with an extension over approximately $200 \times 200 \mu\text{m}^2$. Needless to say, for the integrated detection mode this makes it impossible to recognise the MCP structure or to detect periodic pattern

4. Experimental Setup: Characteristics and Performance

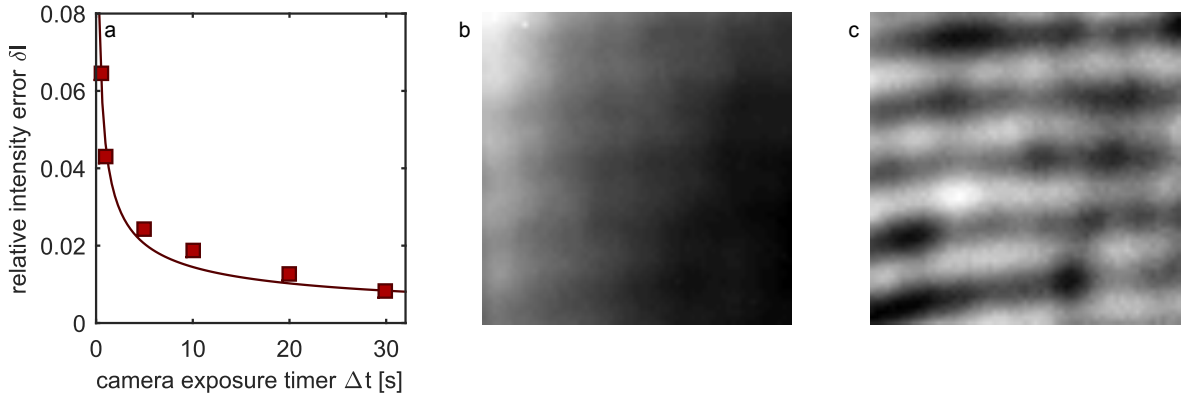


Figure 4.14.: Integrated data acquisition. (a) Poissonian statistics of the single impacts appear within the integrated data acquisition in the form of the relative error of the intensity δI . It decreases with \sqrt{N} for higher camera exposure time Δt (red curve). (b) Raw image of a fringe pattern with low visibility ($\approx 5\%$) and long exposure time ($\Delta t = 60$ s). Due to a non-homogeneous beam over the pattern size and due to a lower efficiency of the phosphor screen in the lower right corner, the fringes are hard to see. (c) Exposing the real image by, firstly, subtracting a “black” image from the raw data, and, secondly, by dividing the residual by a reference image. The black image is without particles but with the same exposure time as the raw image, and the reference image is without a pattern and thus compensates for inhomogeneity of the beam and for the phosphor screen efficiency. The fringes become apparent over the whole image size. The visibility is calculated by taking multiple points along the lines of minimum and maximum fringe intensity following equation (2.5). The reference image is the sum of multiple images (subtracted with a “black” image) each showing the fringe pattern shifted a small fraction over the whole period.

with periodicities around $100\ \mu\text{m}$. In general, particle extension on the camera reduces the fringe visibility significantly with decreasing periodicity. Therefore, the next subsection will go into detail on this feature, while the procedure to analyse the visibility out of the many-particle picture is discussed thereafter.

In contrast to the single-particle images, further effects have to be taken into account when analysing the fringe pattern from the long-exposure pictures. Firstly, residual light from the laboratory is detected, leading to an intensity offset for each pixel. Therefore, for every measurement with given exposure time Δt , an offset image is taken which is subtracted from every image captured later. Furthermore, the phosphor screen shows ageing phenomena depending on the beam intensities. This means that an area on the screen which has been exposed to the beam via the MCP has a lower conversion efficiency than the surroundings and hence appears darker. The solution to this problem is to take a beam image without a pattern as a measure for the detection efficiency of each pixel. For instance, this can be achieved by summing multiple pictures of a fringe pattern while the pattern is being shifted in small steps over one period. Not only does such a reference picture enable to solve the different local detection efficiencies, but it overcomes spatial inhomogeneities within the particle beam as well. Dividing the image with such a reference lets the fringe pattern emerge over the whole

pattern size uniformly as shown in figure 4.14(c). From this processed picture the visibility is retrieved, taking the intensity of several points along the line of minimum and maximum fringe intensity following equation (2.5).

It is worth to notice that the Poissonian statistics have to appear in the relative error of the intensity of the images, as the underlying statistics are the single-particle impacts. Hence, analysing multiple pictures with different exposure times reveals an inversely proportional behaviour with \sqrt{N} , as shown in figure 4.14(a).

4.4.5. Single-Particle Detection versus Integrated Picture: Accuracy versus Time

It might be of interest to use single-particle detection and the integrated acquisition to detect the pattern. If the interferometer has to be adjusted, it is desirable to have a fast feedback on the presence of fringes and, should this be the case, on their possible orientation and periodicity. As soon as the grating adjustment is done, visibility is the only signal relevant for the experiment. Hence the single counting mode can be used to obtain precise data. Nevertheless, it is worth to know how the visibility retrieved from an integrated picture is related to the visibility analysed with single particles.

In mathematical terms, the pattern of the integrated picture can be described as a single-particle pattern convoluted with a Gaussian function. This is just a mathematical expression of the fact that each single particle has a Gaussian extension on the camera image with a standard deviation of $\sigma \approx (70 \pm 10) \mu\text{m}$ (compare equation (4.20)). Based on this, it is clear that the visibility of the pattern is reduced with decreasing periodicity, since the extension of the Gaussian averages a larger fraction of the period. Nevertheless, it can be shown, by calculating the convolution, that the reduction of the visibility is independent of the initial visibility. To confirm this behaviour, we took two fringe configurations with variable periodicity. One with approximately 95 % visibility and one with around 30 % visibility.¹⁰ The result is shown in figure 4.15. The left side shows a direct comparison of the same pattern, once detected via a single-particle recognition and once with a camera exposure time of $\Delta t = 60$ s. The projection angle α was retrieved with the Rayleigh test and applied to the integrated image, too. A great difference in visibility is clearly noticeable. While the single-particle pattern shows a visibility of $\nu_s = 27$ %, the integration technique results in a significantly lower visibility $\nu_c = 3$ %. The right side shows the ratio ν_c/ν_s as a function of periodicity for the two mentioned visibility configurations. A linear dependence in the depicted period range between the ratio and the periodicity is found, while a different initial visibility has no effect on the relation between the two different acquisition modes. Note that even for large periodicities, for which $d \gg \sigma$ holds, the ratio is expected levelling to 1. Applying a linear regression to the data yields the

¹⁰While the 30 % visibility fringe was achieved with the interferometer described in this work, the 95 % visibility is obtained with the three-grating-deflectometer described in [45]. The principle of that deflectometer is the same as for our current interferometer, only that its gratings have a pitch of $d = 40 \mu\text{m}$ and are separated by $L = 35.4$ mm. In both cases is the period of the resulting fringe pattern changed by means of rotating the last grating as described in chapter 2.4.

4. Experimental Setup: Characteristics and Performance

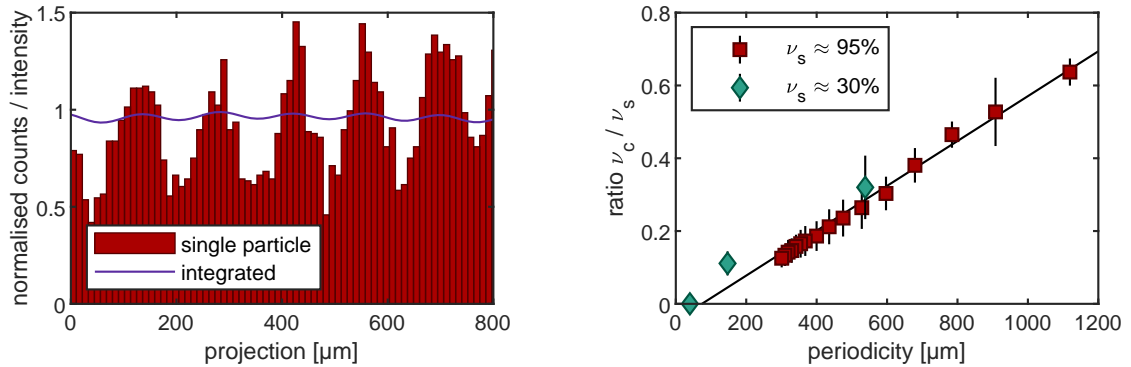


Figure 4.15.: Comparison of the two different ways of detecting a fringe pattern. Left: For the same grating alignment and beam properties, a histogram with single-particle events is shown under the same projection angle α as for the integrated picture. The difference in visibility is clearly identifiable. While in the first case a visibility of $\nu_s = 27\%$ is measured, the second case reveals a $\nu_c = 3\%$ fringe. Right: The ratio ν_c/ν_s shows a strong dependence on the periodicity of the pattern. In fact, for the relevant periodicity range it shows a linear behaviour which is independent of the original visibility (here shown for fringes with $\nu_s \approx 95\%$ and $\nu_s \approx 30\%$).

following conversion rate:

$$\frac{\nu_c}{\nu_s} = 0.62 \text{ mm}^{-1} \cdot d - 0.05 . \quad (4.30)$$

This knowledge provides a tool to convert directly the fringe visibility between the two different acquisition modes. Therefore, in the remainder of this work, no distinction will be made between the two ways of obtaining the visibility (ν_s and ν_c). Note that typically single-particle ν_s provides information about the visibility ν . In rare cases, when ν_c was measured, it is converted to ν_s and hence to ν with equation (4.30).

4.5. Characterising Single Components by Using the Setup as a Whole

Combining the elements of the described experimental setup – namely the source, the gratings and the detector – allows us to get a deeper understanding of the individual components as well as of the whole system. The following sections discuss the photons coming from the ECR source, the divergence of the neutral particle beam, the precision of the grating pitch, and the temporal stability of the interferometer.

4.5.1. Photons Originating from the Source

Placing one grating close to the detector allows to understand the spectrum of neutral particles which emerge directly from the source. It is observed that neutral particles do not only result from collisions inside the experimental chamber but that they also originate from

4.5. Characterising Single Components by Using the Setup as a Whole

the source and are detected on the MCP if the acceleration voltage U_{acc} is put to zero. It is unlikely that the detected particles in case of $U_{\text{acc}} = 0 \text{ V}$ are neutralised ions, as these ought to have thermal energies and hence not be detectable with the MCP. More plausible is the assumption that the remaining neutrals are photons which originate from electronic transitions inside the plasma.

To test this hypothesis one grating is placed at a distance $l = 9 \text{ mm}$ in front of the detector and illuminated with neutrals from an argon plasma ($U_{\text{acc}} = 0 \text{ V}$). The result is not a clear shadow image of the $3 \times 3 \text{ mm}^2$ grating. Instead, additional shadows appear in the horizontal and vertical direction. Following the grating equation, these maxima are identified with the diffraction orders due to the nanometric structure ($d = 257 \text{ nm}$) and the support structure ($d_s = 1.5 \mu\text{m}$). While up to four maxima on each side are seen for the fine structure, the larger structure exhibits only the first order maxima. From the distances of the maxima on the detector and the grating-detector distance, the corresponding wavelength λ can be calculated:

$$\lambda = (105 \pm 7) \text{ nm} . \quad (4.31)$$

Comparing with the spectrum of argon shows that the given wavelength lies in the close vicinity of the spectral lines $\lambda = 106.7 \text{ nm}$ and $\lambda = 104.8 \text{ nm}$ [123]. Therefore, it is likely that the neutrals coming from the source when $U_{\text{acc}} = 0 \text{ V}$ are photons from the electronic transitions inside the plasma.

It may certainly appear surprising that photons from a plasma should interfere on a grating, as the plasma possesses a certain spatial extension and consequently the photons have negligible spatial coherence. To understand this, we consider the coherence criterion, which prescribes the maximal diameter of the source d_{source} for interference with a wavelength λ to be observed on an object with a diameter D and a distance L away from the source:

$$d_{\text{source}} \ll \frac{\lambda}{D} L . \quad (4.32)$$

For the given setup, assuming that only 1 mm^2 of the grating participates in the interference pattern, we see that the source has to be smaller than

$$d_{\text{source}} \ll \frac{105 \text{ nm}}{1 \text{ mm}} 2.30 \text{ m} \approx 250 \mu\text{m} . \quad (4.33)$$

The resulting $250 \mu\text{m}$ is half the size of the pinhole on the ECR source which may suggest that the effective source size is reduced or the grating area participating in the interference pattern is smaller than 1 mm^2 .

Finally, we state the photon abundance compared to the neutrals from the source if U_{acc} is switched on. Measurements for argon show that the ratio of photons to neutral particles is in the order of 1% and therefore negligible for the use of the neutral atomic beam.

4.5.2. Systematic Study of Individual Actuator Movements and their Informative Value about the System

A systematic scan of each single actuator can provide a deeper understanding of the system. With a y -scan we can verify whether the fringes are due to the nanometric structure and are not an artefact of the support structure. Moreover, it helps to characterise the fine positioning of the vertical actuator. α -scans on grating one and two allow conclusions to be drawn about the precision of the grating pitch, as minor differences in the pitch are reflected in the behaviour of the moiré pattern. A horizontal z -scan provides information about the divergence of the used particle beam. In the following, each scan and the conclusions drawn from it is discussed more closely.

y -Scan: Proof of Nanometric Moiré Fringes

In order to confirm whether the detected fringes are moiré fringes caused by the nanometric gratings as described in chapter 2.4 or whether they are of a different origin, a vertical scan of the last grating can be performed. As discussed before, a vertical shift of the third grating by one grating period results in a fringe shift of 2π also for the moiré pattern. Figure 4.16 depicts single-fringe projections for different piezoelectric voltages of the third actuator, which exactly reflects this behaviour. The evolution of the fringe phase is clearly visible and shows a linear dependence on the voltage. A linear regression of the phase allows precisely to calibrate the actuator and yields

$$d = 257 \text{ nm} \hat{=} 4.0 \pm 0.1 \text{ V} . \quad (4.34)$$

This is consistent with the actuator specifications and hence proves the reliability of the nanometric moiré fringes.

α -Scan: Precision of the Grating Pitch

Small variations in the grating pitch do not alter only the moiré visibility, as discussed in chapter 3.1.2, but also its behaviour, in correspondence with equation (2.35). A full rotational scan of the first two gratings elucidates the difference between the fringe pattern in the plane of the third grating (the so-called nanoscopic pattern) and the last grating itself which is used to magnify the pattern using the moiré effect.

Figure 4.17 displays the period and the orientation angle of the detected moiré fringe over a systematic scan of α_1 and α_2 , respectively. If the nanoscopic fringe pattern and the last grating were perfectly aligned and had the same period, a uniform and homogeneously illuminated square would be expected on the detector, which is mathematically equivalent to divergence of the fringe period to infinity. In contrast, a minor periodic difference $\Delta d = |d_1 - d_2|$ would result in a finite moiré beating with a macroscopic periodicity of

$$D = \frac{d_1 \cdot d_2}{\Delta d} , \quad (4.35)$$

4.5. Characterising Single Components by Using the Setup as a Whole

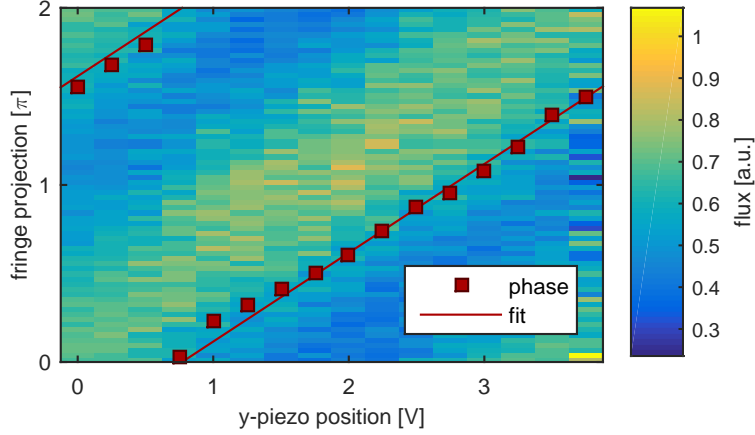


Figure 4.16.: Vertical scan (y-scan) of the last grating for a typical fringe (here taken with a neutral hydrogen beam). Shown is the fringe projection for different piezoelectric voltages of the vertical actuator. The phase shows linear dependence on the voltage, while a full shift is accomplished over 4 V. This is consistent with a grating shift of one period with $d = 257$ nm. (The error bar for the phase lies within the marker size.)

which is a special case of equation (2.35) for $\alpha = 0$. Hence, the fringe period in figure 4.17 directly implies that there must be a difference in period. Note, that a rotational change of the second grating (α_2) causes the nanoscopic fringe pattern to rotate twice the angle, whereas α_1 has a one-to-one relation to the rotation of the pattern in the plane of the third grating. This is the reason why the spread of the data in figure 4.17(c) is half as large as in figure 4.17(a). Fitting the full moiré equation (2.35) to the fringe period yields a difference between the last grating and the nanoscopic fringe pattern of

$$\Delta d = 140 \pm 20 \text{ pm} . \quad (4.36)$$

Such a discrepancy can be explained by a pitch difference of half of its value between the first and second grating, i.e. $\Delta d = d_2 - d_1 = 70$ pm, following the argumentation in chapter 3.1.2. Furthermore, such a minor difference of 0.5‰ in the grating pitches can also be explained with a small tilt β_x of one of the gratings, as the effective period is reduced according to

$$d_{\text{eff}} = \cos(\beta_x)d . \quad (4.37)$$

For the measured difference, this would imply a tilt of

$$\beta_x = 33 \pm 2 \text{ mrad} = 1.9^\circ \pm 0.1^\circ . \quad (4.38)$$

This value is two orders of magnitude higher than expected from the results of the gratings' alignment (compare equation (4.16): $\Delta\beta_x \lesssim 200 \mu\text{rad}$). Consequently the periodic mismatch is more likely to arise from the gratings themselves.

Looking at the orientation of the moiré pattern in figures 4.17(b) and (d) exposes a further

4. Experimental Setup: Characteristics and Performance

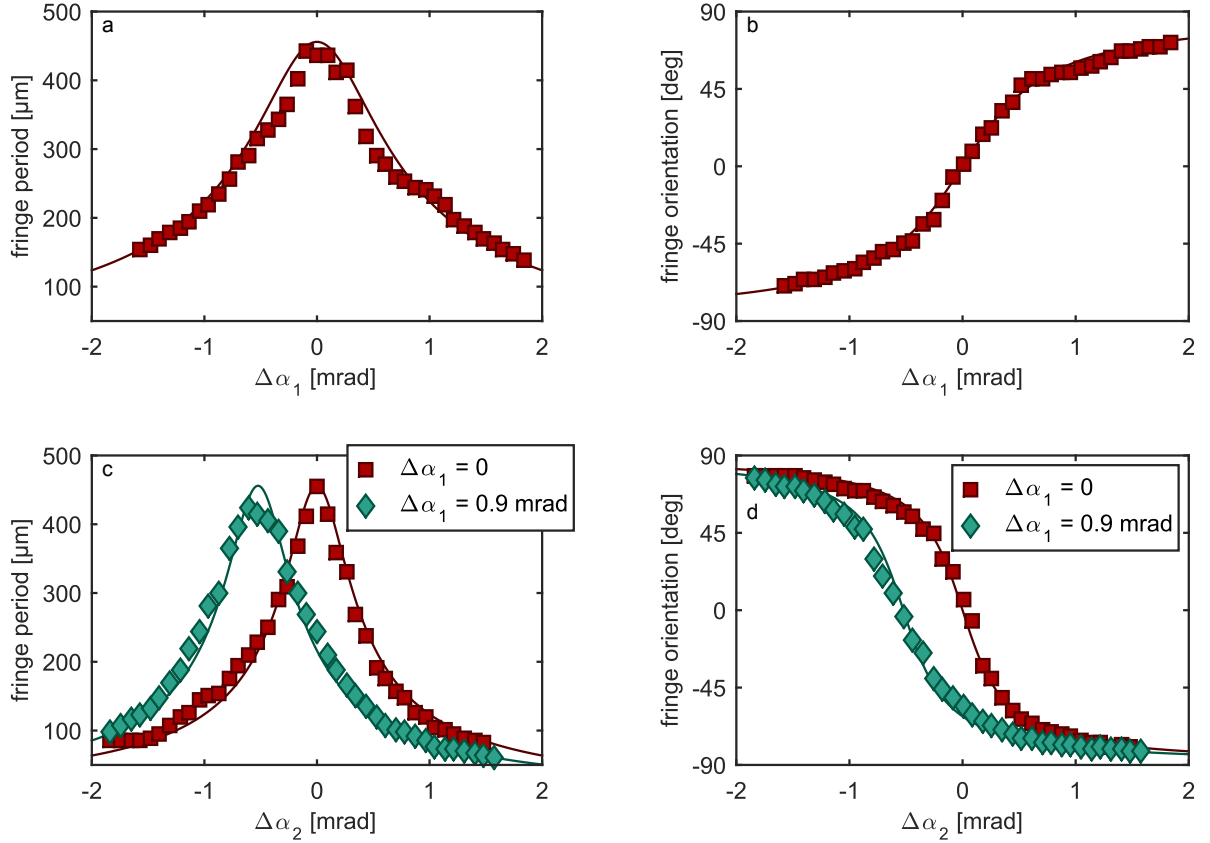


Figure 4.17.: Rotational scan of the first (α_1) and second (α_2) grating and the behaviour of the moiré pattern. Fitting the theoretical cure (equation (2.35)) to the data reveals, that the nanoscopic fringe pattern is larger than the last grating by $\Delta d = 140 \pm 20$ pm. The rotation angles (grating angle and fringe orientation) are given anti-clockwise along the beam axis. The error bar is within the marker size.

interesting artefact. From a geometric consideration, it can be seen that a rotation of the first grating by α_1 causes a rotation of the nanoscopic fringes on the third grating in the *opposite* sense, i.e. $\alpha_n = -\alpha_1$. On the other hand, a rotation of the second grating by α_2 leads to a rotation of the nanoscopic pattern in the *same* direction but with double the amplitude, i.e. $\alpha_n = 2\alpha_2$. This explains the different evolution of the fringe orientation over α_1 and α_2 . However, a still closer look also reveals that the movement of the macroscopic moiré fringes is just the opposite to the nanoscopic fringes. This evidence proves that the periodicity of the nanoscopic fringes is larger than the periodicity of the last grating, i.e.

$$d_{\text{nano}} > d_3, \quad |d_{\text{nano}} - d_3| = 140 \pm 20 \text{ pm} . \quad (4.39)$$

4.5. Characterising Single Components by Using the Setup as a Whole

In the opposite case ($d_{\text{nano}} < d_3$) the moiré orientation would follow the nanoscopic fringe orientation. For the difference between the first and second grating this means:

$$d_2 > d_1, \quad |d_2 - d_1| = 70 \pm 10 \text{ pm}. \quad (4.40)$$

The fact that the second grating rotates the pattern twice its own angle can be also noticed in figure 4.17(c) and (d) where the measurement was repeated for a fixed offset angle $\Delta\alpha_1 = 0.9 \text{ mrad}$ resulting in the curve's rotating in the negative direction only by a half of $\Delta\alpha_1$.

z -Scan: Beam's Divergence

Figure 4.18 shows the visibility for three different gases if the first grating is horizontally misplaced by a distance Δz . Such a displacement brings the gratings out of the equidistant position and hence reduces the visibility of the fringes. Another factor which affects the visibility is the divergence of the beam which governs how fast the visibility drops as Δz increases (compare section 3.1). Hence, the horizontal scan can be used as a measure of divergence. A least squares optimisation of the measured gases' visibility depicted in figure 4.18 with the theoretical curve (section 3.1.1) yields the following diffusivity of the different particle beams:

$$\alpha_{\text{H}} = 1.05 \pm 0.04 \text{ mrad}, \quad (4.41)$$

$$\alpha_{\text{Kr}} = 0.24 \pm 0.02 \text{ mrad}, \quad (4.42)$$

$$\alpha_{\text{Xe}} = 0.23 \pm 0.05 \text{ mrad}. \quad (4.43)$$

Here we see the necessity for a well-collimated beam, as the maximum critical misplacement is

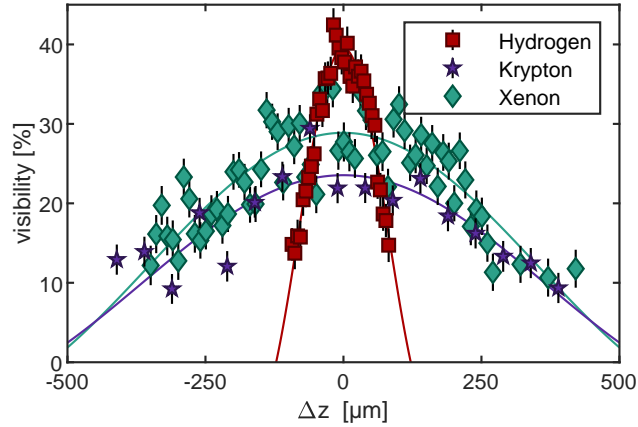


Figure 4.18.: Horizontal z -scan to measure the beam divergence. Shown is the visibility as a function of the z -displacement with respect to the ideal position $\Delta z = 0$ (maximum visibility corresponds to equidistant gratings). Measurements were performed with a 3.6 keV hydrogen beam, a 17.7 keV krypton beam, and a 14.7 keV xenon beam. The width of the visibility gives an insight on the beam's divergence. It holds that the smaller the width is, the larger the divergence becomes.

4. Experimental Setup: Characteristics and Performance

reduced with higher diffusivity. In this measurements, the neutral particle beam was produced on the grounded mesh in front of the source. Hence, the diffusivity should be determined by the opening of the source ($D = 500 \mu\text{m}$) and distance to the interferometer ($l = 2.30 \text{ m}$), i.e. $\alpha = D/l = 0.22 \text{ mrad}$. Comparing the results shows that this fits well for krypton and xenon, whereas for hydrogen an effective source diameter of five times the actual source opening (i.e. $D_{\text{H}} = 2.5 \text{ mm}$) has to be taken into account, indicating a larger neutralisation area for the hydrogen production on the grounded mesh.

4.5.3. Stability of the Interferometer

The last question we address is the question about the stability of the interferometer. In section 4.4 it was shown that the MCP is sufficiently stable with respect to the camera outside the vacuum. An upper limit of $12.5 \mu\text{m}$ was given for the drift of the detection system in three days (see table 4.5). For the interferometer the critical drift is much smaller. A drift of one grating with respect to another grating, of one period, i.e. 257 nm , would wash out the fringe pattern and reduce the detected visibility significantly. To study this effect a hydrogen fringe at 3.6 keV was measured with single-particle events over three hours (see figure 4.19). The dataset was then divided into smaller subsets with a sampling time Δt , which were investigated separately. The left graph shows the thereby retrieved visibility for the pattern over different sampling times. Unsurprisingly, as the number of detected particles increases with the sampling time, the statistical error decreases accordingly. More interesting, however, is the kink in the visibility for a sampling time of approximately 100 min . There, the visibility drastically drops, indicating that a phase shift in this time domain starts to play a crucial role. The right side in figure 4.19 depicts the evolution of the fringe phase for two different sampling times. Here we clearly see that the fringe pattern drifts over half a period in 150 min , with minor drifts in the range of 10 min on top of it. For the interferometer, this would mean a corresponding grating shift of around 130 nm in three hours. For a higher sampling time, as shown for example for $\Delta t = 30 \text{ min}$, the analysis cannot resolve the minor phase shift in its detailed trend anymore, but only the overall drift. In comparison with the plot on the left, averaging over the minor drifts does not reduce the visibility significantly ($\Delta t = 10 \text{ min} \rightarrow \nu = 15.6 \pm 1 \%$, $\Delta t = 30 \text{ min} \rightarrow \nu = 15.1 \pm 0.5 \%$). On the other hand data sampling of more than 100 min would include different subsets with phases greater than a quarter of period. This would reduce the fringe visibility significantly, as the kink in the left graph makes clear.

From these results we learn that longer data acquisitions do not produce more precise results, as the statistical error decreases. A longer acquisition time also makes room for systematic error such as drift of the fringe pattern due to instabilities inside the interferometer. Therefore, in the present work we made sure to avoid systematic errors due to drifts by always analysing the full dataset and its subsets.

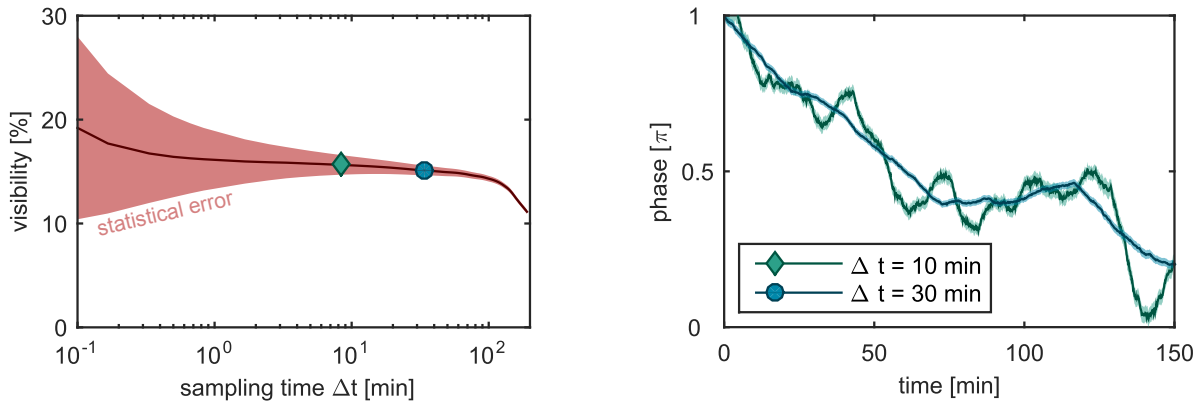


Figure 4.19.: Pattern stability over time. Left: Sampling a three-hour-long data set into subsets with a sampling time Δt in order to analyse the visibility. The statistical error in the visibility decreases as the sampling time increases. While the visibility is nearly constant for a sampling time up to $\Delta t = 100$ min, it decreases rapidly for larger sampling times. This effect is due to a phase shift of the pattern in this time domain, resulting in a wash-out of the pattern and hence reduction of the measured visibility. Right: Analysing the phase shift reveals a drift over half a period in 150 min, which is equivalent to a drift of the third grating by 130 nm. Such a drift is the reason for the decline in visibility for higher sampling times. Evaluating the drift for a small sampling time ($\Delta t = 10$ min) resolves also minor phase modulations over the overall phase drift, while a higher sampling time ($\Delta t = 30$ min) only shows the long-term shift.

4.6. Summary

An experiment has been designed and built to show the interferometrical and classical behaviour in one setup for a wide range of neutral particles.

Its first stage produces a well-defined particle beam of atomic hydrogen, helium, argon, krypton, or xenon. To this end, an ECR source delivers the respective charged particles at an energy ranging from 500 eV to 20 keV, which are neutralised upstream at a metal or gas target without losing energy. A small energy spread of 1.3% has been measured for the hydrogen beam. In order to control the divergence of the beam, different pinholes can be introduced in front of the interferometer.

The main part of the experiment is the three-grating Talbot-Lau interferometer. All three gratings with a pitch of 257 nm are placed on a set of actuators to ensure that the gratings are parallel and equidistant. The whole device is placed inside a mu-metal shield which reduces the Earth's magnetic field by a factor of more than a hundred. Any influence of stray electric fields is avoided by means of copper tubes and a copper mesh between the metallic coated gratings.

Particles participating in forming a fringe pattern are detected upstream with a two-stage MCP, a phosphor screen, and a camera. Detecting individual particles can be performed with a position resolution up to $10 \mu\text{m}$, while the dark count rate is kept less than 1%. With the Rayleigh test, an efficient way of obtaining the pattern's period, orientation, and visibility has been shown. For faster data acquisition multiple particles can be detected at once, albeit

4. *Experimental Setup: Characteristics and Performance*

at the cost of reduced visibility due to finite extension of the particle's impacts on the camera. A linear relation between the visibility obtained with single particles and integrated pictures makes it possible to correct for this effect.

With this completed experimental setup, systematic studies on its different parts reveal important insights into the experiment. It has been shown that photons whose spectral lines are consistent with those of the plasma originate from the source, and can interfere on the gratings. Furthermore, the nanoscopic fringe in the plane of the third grating is larger than the last grating by $\Delta d = 140 \pm 20$ pm due to similar small differences in the gratings' pitch. With the grating not placed equidistantly, the divergence of the beam for hydrogen, krypton, and xenon has been measured.

This characterised setup fulfils all the conditions necessary to show interference on the three-grating interferometer with hydrogen and helium, and on its classical counterpart with argon, krypton, and xenon. The next chapter presents these results and shows how we come from the quantum to the classical limit with one setup.

5. From Classical Xenon Fringes to Hydrogen Interferometry

The previous chapters gave a detailed understanding of the principle of the three-grating setup and its description as a Talbot-Lau interferometer or as a classical moiré deflectometer. Thereby the preceding chapter explained explicitly the experimental realisation and implementations of the ideas presented in the theoretical chapters. Especially, it provided a set of procedures to expose the three-grating setup with well-defined particle beams in mass and energy and to extract the visibility out of the resulting periodic pattern.

The present chapter summarises the experimental results. Starting with two similarly looking fringe patterns, we demonstrate that for one of them its energy dependence can still be described in classical terms, while for the second one a quantum mechanical description, considering particles' wave character, has to be taken into account. Furthermore, we show how the characteristic behaviour of the Talbot-Lau interferometer can be used as a spectrometer if the composition of the particle beam is not well understood. Finally, the obtained data provide the possibility to estimate the charge implanted into the gratings by considering the intra-grating interaction discussed in section 3.4 and give an outlook on the feasibility of an ion interferometer with an equivalent setup.

5.1. Necessity of Considering Quantum Behaviour

Figure 5.1 shows two typical macroscopic fringe patterns as obtained with the three-grating setup and a neutral xenon beam (left: 11.6 keV Xe-beam) or a neutral hydrogen beam (right: 3.7 keV H-beam). The last grating was tilted ($\alpha_3 \approx 1$ mrad) to magnify the nanoscopic pattern and single particle hits were detected and their center of mass analysed (compare sections 2.4 and 4.4.2). The Rayleigh test and a sinusoidal fit (compare section 4.4.3) reveal for both patterns similar visibilities $\nu \approx 40\%$. The histogram on the right of each picture depicts a projection of the pattern along the orientation angle, i.e. along the horizontal axis, and clearly reveals the fringes.

At first glance, both patterns can be explained by means of classical trajectories theoretically discussed in section 2.6: an uncollimated beam passes through the first two gratings and forms a shadow image due to geometric constraints of the trajectories in the plane of the third grating.

5. From Classical Xenon Fringes to Hydrogen Interferometry

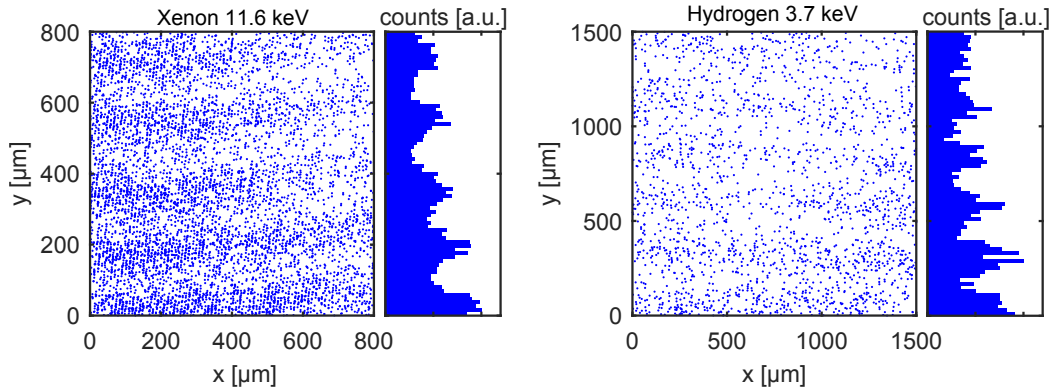


Figure 5.1.: With the same three-grating device a fringe pattern is observed with a xenon beam ($E = 11.6$ keV) and a hydrogen beam ($E = 3.7$ keV). Both patterns exhibit similar visibility ($\nu \approx 40\%$) and appear explicable by using classical trajectories. The histogram on the right of each picture shows the fringe projection in the direction of the pattern, i.e. the horizontal direction.

For a beam of particles with classical trajectories, a gradual reduction in the visibility of the observed pattern is expected for decreasing particle energy. This is owing to an increased interaction time of the particle beam with external perturbations inside the grating slits as the particle energy is reduced. And, indeed, changing the energy for the xenon beam shows a visibility reduction for slower particles (see figure 5.2), which justifies the description of the experiment with the particles' classical trajectories. Furthermore, changing the particle species to the next lighter noble gas, e.g. krypton or argon, reveal a similar behaviour (see figure 5.2). At 20 keV, the fringes start with a high contrast (around 40%) which goes down to almost 0% as the energy approaches 2 keV.

However, the situation is very different for the fringe pattern of the hydrogen beam (compare figure 5.2) and invalidates the attempt to describe the pattern in classical terms. Starting from the fringe pattern with an energy of $E = 3.7$ keV and further increasing the particles' energy causes the visibility to drop. The contrast goes down to 0% at around 5 keV, causing the pattern to disappear for the whole higher energy range accessible within the experimental setup. Reducing the energy from 3.7 keV causes a reduction of contrast as well, until a complete disappearance at 2.8 keV. However, the fringe pattern reappears with a similar contrast of 30% around 950 eV. Repeating the measurement with a helium beam reveals a similar behaviour, but with only one visibility maximum in the accessible range of energies. Furthermore, the visibility maximum lies at 950 eV, the same as one of the hydrogen contrast peaks, while the maximum at 3.7 keV seen in hydrogen, disappeared.

The different behaviour for the hydrogen and helium beam compared to the classical description consistent with xenon, krypton, and argon provides strong indication about the insufficiency of the classical theory and calls for an explanation in terms of the particles' wave nature. In order to affirm quantum behaviour, we change the visualisation of the visibility and plot all the measured data as a function of the de Broglie wavelength following equation (1.1). Such representation of the different data sets as depicted in figure 5.3 shows a greater

5.1. Necessity of Considering Quantum Behaviour

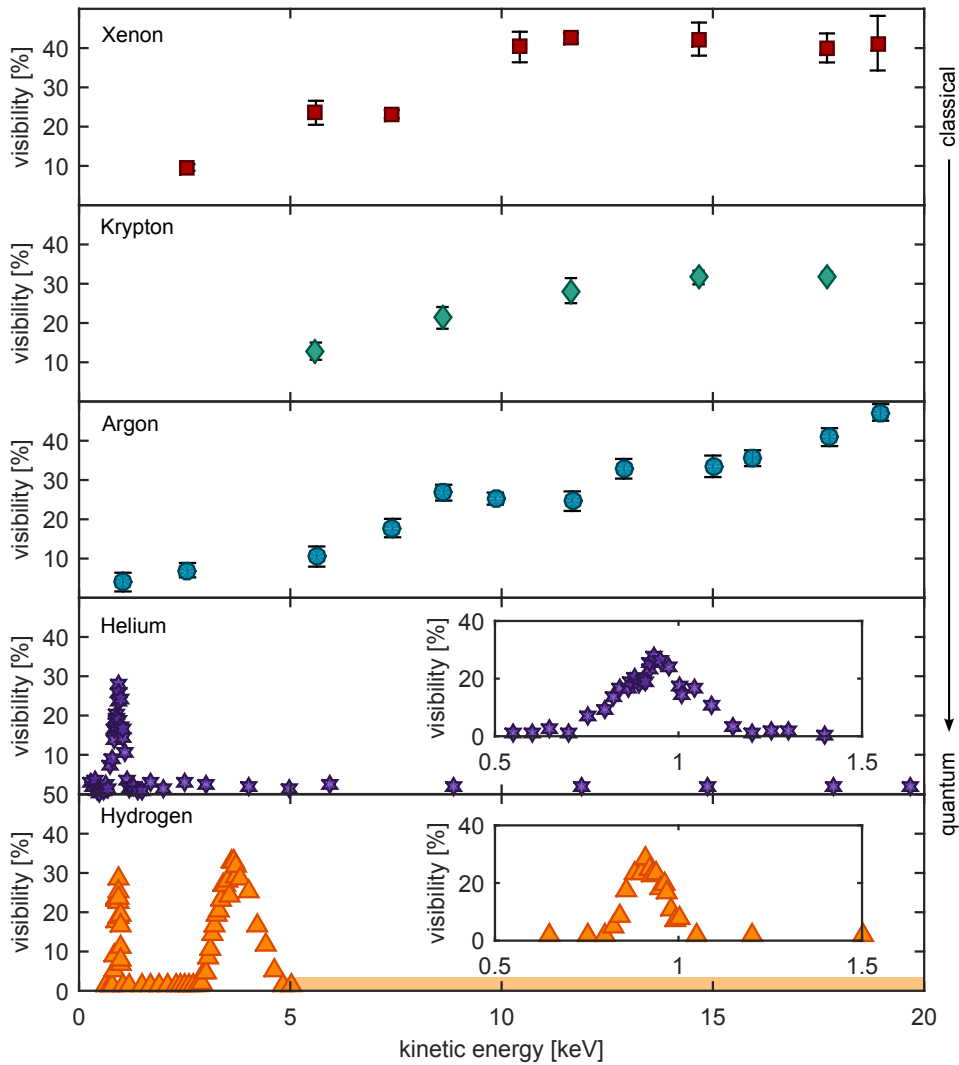


Figure 5.2.: Visibility as a function of particle energy reveals a significant difference between the different atom species. For heavier atoms, like xenon, krypton, and argon, visibility diminishes with decreasing particle energy. This is explainable in classical terms by considering that with lower energy, the particle velocity is reduced, providing a longer interaction time for disturbing forces which act upon the particles and smear out the pattern. For lighter particles, like helium and hydrogen, no fringe pattern is identified in the higher energy range, while distinct visibility peaks appear around 1 keV and 4 keV. The classical picture is insufficient to explain the visibility peaks and therefore the data demand that the particles' wave character be taken into account. (Note: Unless specified otherwise, the error bars are within the marker size. Furthermore, the higher energy range for hydrogen was visually analysed with the integrated data acquisition mode revealing no fringe pattern. Hence, the yellow bar indicates the noise floor in this energy range. The small insets show a magnification of the peaks around 1 keV.)

5. From Classical Xenon Fringes to Hydrogen Interferometry

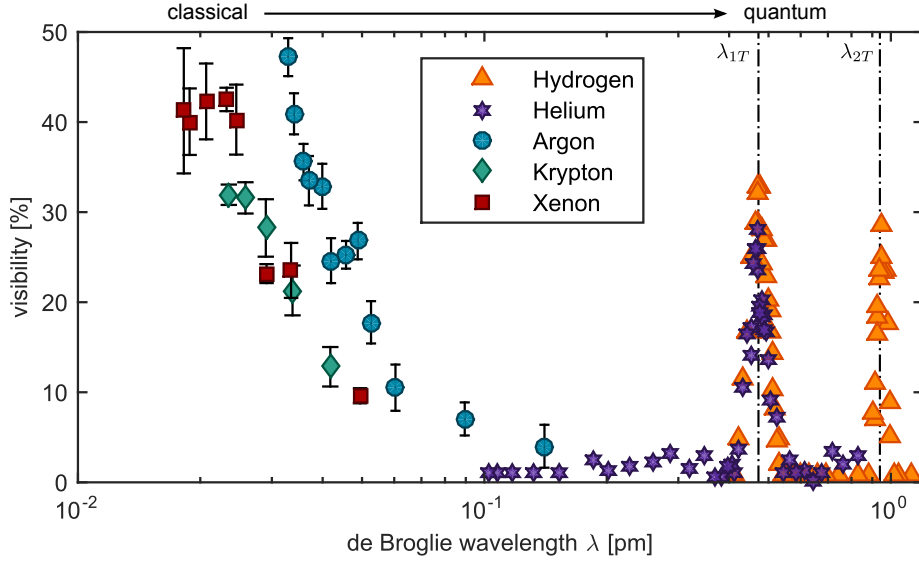


Figure 5.3.: Mapping the various datasets for the different particles as a function of the de Broglie wavelength $\lambda = h/p = h/\sqrt{2mE}$ reveals a uniform picture which can be only explained by considering the wave nature of the particles. As predicted for the Talbot-Lau interferometer, visibility maxima appear at the position where the Talbot length corresponds to an integer fraction of the grating distance. Therefore, the visibility peaks for the hydrogen and helium beams mark the position for which the Talbot length is equal to the grating distance and in the case of the second peak equal to half the grating distance. The heavier particles have much smaller de Broglie wavelengths than the wavelength corresponding to the first Talbot length, and hence mark the transition to the classical regime.

consistency as all data seem to fall on one curve compared to the cases of plotting the visibility versus the particles' kinetic energy. Hence, it reveals the underlying quantum mechanical structure of the experiment and allows us to review the characteristics of the Talbot-Lau interferometer introduced in chapter 2.

The Talbot-length: The Talbot length L_T , introduced in equation (2.1), defines the distance after the grating for which a self-image of the grating itself can be observed. When considering a Talbot-Lau interferometer, instead of a single grating, equation (2.6) shows that several fringes with high contrast are expected to appear whenever the de Broglie wavelength is a multiple of 472 fm, i.e. $\lambda_{nT} = n \cdot 472$ fm. To prove this condition, we use a Gaussian curve to fit the peaks in figure 5.3, which yields a maximum visibility for the following wavelengths:

$$\text{Hydrogen:} \quad \lambda_{1T} = 474 \text{ fm} \pm 2 \text{ fm} = (1.004 \pm 0.004) \cdot 472 \text{ fm} \quad (5.1)$$

$$\lambda_{2T} = 951 \text{ fm} \pm 2 \text{ fm} = (2.015 \pm 0.004) \cdot 472 \text{ fm} \quad (5.2)$$

$$\text{Helium:} \quad \lambda_{1T} = 470 \text{ fm} \pm 3 \text{ fm} = (0.996 \pm 0.006) \cdot 472 \text{ fm} . \quad (5.3)$$

5.2. Talbot-Lau Interferometer as a Spectrometer

The peak values obtained by fitting the data agree with the theoretical prediction within 0.5%, thus supporting the claim that the detected contrast maxima can be ascribed to the first and second Talbot length for hydrogen, and to the first Talbot length for helium. Note that combining equations (1.1) and (2.6) to

$$E_{n,m} = \frac{h^2 L^2}{2d^4} \cdot \frac{1}{n^2 m} \quad (5.4)$$

reveals that the visibility peak for hydrogen around 950 eV and for helium at precisely the same energy represent the second and first Talbot order, respectively. The reason for which the two peaks appear at the same kinetic energy is the energy's quadratic dependence on the Talbot order n .

Classical Limit: In equation (2.7), we stated that a particle beam can be described classically in our setup if the de Broglie wavelength is much smaller than 472 fm. Figure 5.3 shows that all the heavier particles, such as xenon, krypton and argon, have de Broglie wavelengths smaller than 100 fm. In the previous reasoning we argued, that the classical description is able to explain the pattern generated with such particles and hence referred to it as classical. The theoretical description of the interferometer legitimates this assumption of taking the classical reasoning for the heavier particles, as this wavelength regime marks the transition from the quantum to the classical regime.

The measured data with well-defined beams have demonstrated the working principle of the Talbot-Lau interferometer for a wide range of particles. In addition, it has been shown that for de Broglie wavelengths which are small in comparison to the Talbot wavelength the setup can be described classically. Equipped with this understanding, the Talbot-Lau interferometer can be conversely used to analyse properties of a beam if, for instance, the composition of the beam is not well understood, as discussed in the following.

5.2. Talbot-Lau Interferometer as a Spectrometer

In chapter 4.1 we discussed how a well-defined particle beam can be achieved with known particle mass and velocity. There, we also introduced the working principle of a pressure chamber to convert ions via a charge exchange reaction into fast atoms with the same kinetic energy. This step was of significant relevance to show the characteristic behaviour of the Talbot-Lau interferometer in the previous section (5.1). Besides such a particle production, we also reported on neutral atoms produced directly from the source (compare section 4.1.4). These neutral particles were assumed to be formed on the grounded grid in front of the plasma cavity. In this case we had no access to the information about the specific neutralisation reaction that generated the detected particles. Due to lack of this knowledge, in table 4.2 we listed all possible reactions and their resulting momenta in dependence on the acceleration voltage U_{acc} , leaving open the precise composition of the neutral particle beam which is directly produced from the source.

5. From Classical Xenon Fringes to Hydrogen Interferometry

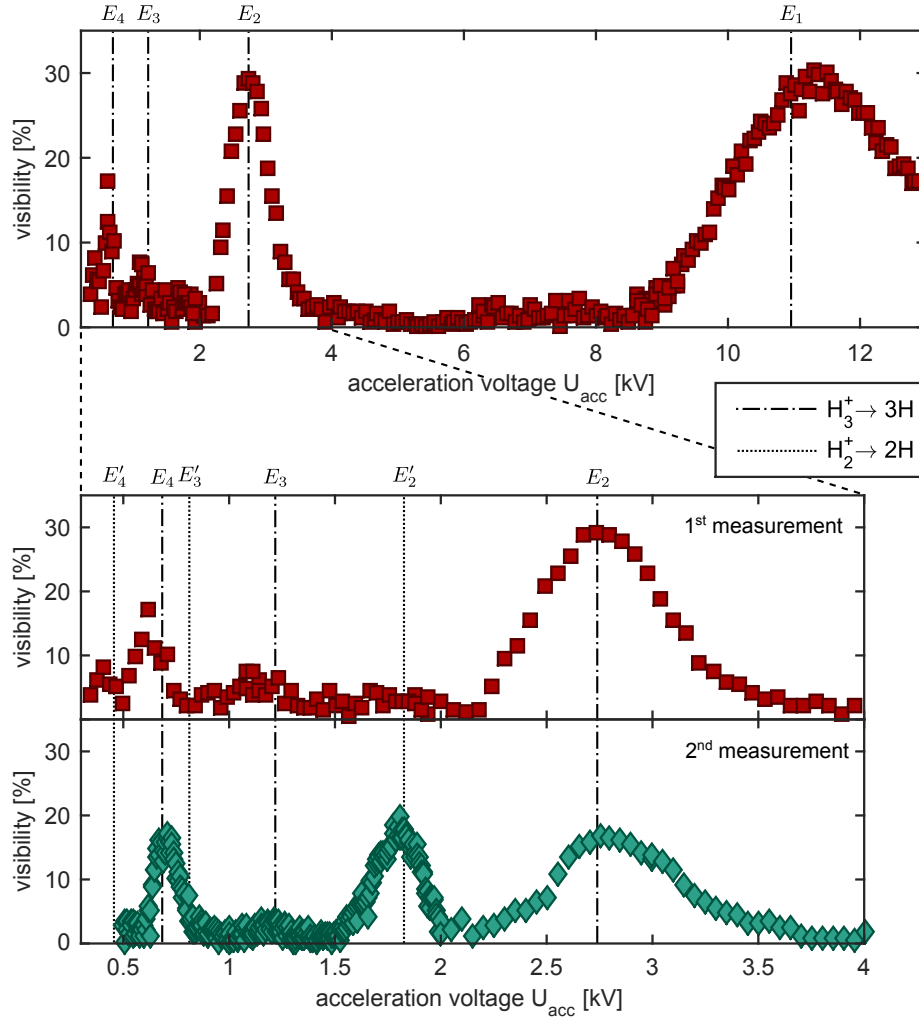


Figure 5.4.: Using the working principle of the Talbot-Lau interferometer as a spectrometer. Shown are two measurements of the fringe patterns visibility over the applied acceleration voltage U_{acc} . For the first measurement (red) well separated visibility peaks can be identified corresponding to the reaction $\text{H}_3^+ \rightarrow 3\text{H}$. The indicated vertical lines E_n mark the calculated positions of the visibility peaks with Talbot order n . The second measurement (green) shows another peak which can be described with the reaction $\text{H}_2^+ \rightarrow 2\text{H}$ (E'_n), indicating that the composition of the particle beam changed for the second measurement. Note that for both possible reactions the peak for the third Talbot order is strongly suppressed.

5.2. Talbot-Lau Interferometer as a Spectrometer

1st measurement	2nd measurement	reaction	Talbot order
11.40 kV \pm 0.03 kV	-	$\text{H}_3^+ + e \rightarrow 3\text{H}$	0.98 \pm 0.01
2.77 kV \pm 0.01 kV	2.84 kV \pm 0.02 kV	$\text{H}_3^+ + e \rightarrow 3\text{H}$	1.98 \pm 0.02
-	1.80 kV \pm 0.004 kV	$\text{H}_2^+ + e \rightarrow 2\text{H}$	2.01 \pm 0.01
-	1.19 kV \pm 0.02 kV	$\text{H}_3^+ + e \rightarrow 3\text{H}$	3.03 \pm 0.03
0.61 kV \pm 0.11 kV	0.71 kV \pm 0.004 kV	$\text{H}_3^+ + e \rightarrow 3\text{H}$	4.08 \pm 0.22

Table 5.1.: Identified positions of the visibility peaks in figure 5.4 and their possible underlying production mechanism with the corresponding calculated Talbot order following equation (5.4).

The Talbot-Lau interferometer is a powerful tool to address this question. For certain particle momenta the interferometer will exhibit high-contrast fringes. Following equations (1.1) and (2.6) the specific momenta for which this is the case are

$$p_n = \frac{hL}{d^2n}. \quad (5.5)$$

With this relation and the collection of possible reactions in table 4.2 it is possible to get an insight into the beam's composition. For this, we measure the fringe patterns' visibility over the acceleration voltage U_{acc} for the neutral particles coming directly from the source, as shown in figure 5.4 (red data points). As predicted, the visibility evolution shows distinct maxima comparable to the well-understood case in figure 5.2. The positions of the peaks are identified via a Gaussian fit and listed in table 5.1. Following equation (5.4) and comparing the data in figure 5.2 it can be observed that the energies at which the peaks are located are around three times higher than what is expected for hydrogen produced via a charge exchange reaction in the neutralisation chamber. This artefact strongly indicates that in the source, hydrogen atoms must be formed from accelerated H_3^+ . Note that the state of the source itself can influence the composition of the beam: After a maintenance intervention on the source, a secondary, previously unrecorded peak appeared at around 1.8 kV, while the contrast of the main peak at 2.77 kV fell from 30 % to 15 % (figure 5.4 green data points). A comparison between the newly formed peak with the possible reactions reveals that the peak could be due to hydrogen atoms occurring from accelerated H_2^+ . This means that the beam for the second measurement is a mixture of hydrogen atoms originating from the following reactions:



A mixed particle beam for the second measurement (green) can also explain why the visibility of the H_3^+ -peak decreased by half of its initial value in comparison to the first measurement (red). For the fringes at the H_3^+ -peak, additional hydrogen atoms coming from H_2^+ will only lead to a constant offset to the fringe pattern, thus reducing visibility.

5. From Classical Xenon Fringes to Hydrogen Interferometry

In summary, the peaks in the source spectrum fit well to the assumption of the two mentioned production mechanisms. Furthermore, visibility peaks up to the fourth order for the H_3^+ production mechanism can be observed. It is, however, surprising to notice that the third order for H_3^+ is strongly suppressed, while the fourth order shows the same magnitude as the first and second orders. We observe a similar effect with the beam originating via H_2^+ acceleration: While the second order is clearly identified, the third order is suppressed as well. Also worth noticing is the same magnitude of the peaks for the two different production mechanisms. This could be understood if the particle beam consists of an approximately equal number of hydrogen atoms originating from H_2^+ and H_3^+ . However, there are no strong arguments why this must be the case.

To address these questions the case of a well-understood particle beam should be reconsidered in order to mimic the assumed composition of the particle beam. With the introduced pressure chamber and the Wien filter installed in front of it, it is possible to select the H_2^+ and H_3^+ ions separately and to convert them via charge exchange into neutral hydrogen atoms, following the same production mechanisms as studied before. Such an experiment can shed light on the questions about the suppressed third order and the equal height of the visibility peaks, and to confirm the working principle of the Talbot-Lau interferometer as a spectrometer.

5.3. Strength of Intra-Grating Interactions

The measured visibility in figure 5.3 reveals a striking and noteworthy difference in comparison to the calculated visibility profile in figure 2.1. On the one hand, heavy particles with wavelengths below 0.1 pm show a faster decrease in visibility as theoretically predicted, while, on the other hand, the visibility maxima for the Talbot condition are narrower than expected. To understand such a change in the visibility evolution we discussed various factors, which affects the patterns' visibility, in chapter 3. However, most of them, such as the gratings' misalignment or independent vibrations, merely reduce the visibility by a constant factor. Hence, even when considering such a negative influence, one still expects the same shape of the visibility profile. The situation is different if one assumes intra-grating interactions. In section 3.4 we showed that charges placed inside the grating bars can change the overall visibility behaviour. We use this knowledge in the following in order to explicate the differences in the visibility plots and to estimate the number of implanted charges. Hereby we neglect the absolute values of the visibility, as these can be influenced by a mixture of the aforementioned artefacts (vibrations, misalignment etc.) and focus on the overall shape of the visibility evolution.

To estimate the amount of charges Q implanted inside the grating, we have to find the simulated visibility profile (compare section 3.4.2) for a specific Q which suits best the measurements. For this purpose we perform numerous simulations to retrieve the visibility profiles for all kind of mentioned particles, each time assuming a different implanted charge covering the range between $Q = 0e$ and $Q = 2000e$ with a step size of $Q = 10e$. Using the least square method on this set of simulations with the data, and further introducing a free parameter for the proportional visibility reduction indicates the best agreement of the data with the simulation performed for a specific Q .

5.3. Strength of Intra-Grating Interactions

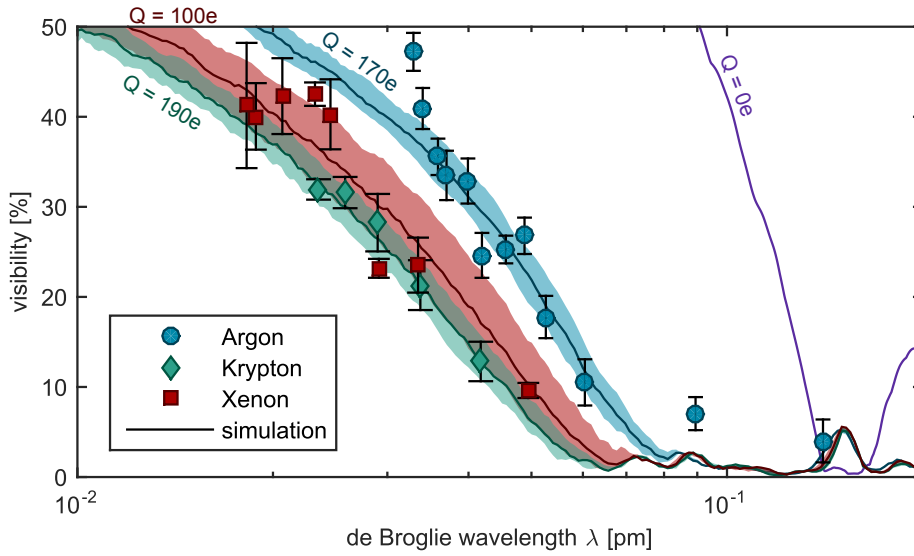


Figure 5.5.: Interpreting the measured visibility with intra-grating interactions due to implanted charges. The visibility for argon, krypton and xenon drops to zero at much smaller wavelengths ($\lambda \approx 0.06$ pm) compared to the simulated visibility profile not considering intra-grating interactions, i.e. $Q = 0$ e. A good agreement with the data is obtained if implanted charges are assumed to be Ar: $Q = 170$ e, Kr: $Q = 190$ e, Xe: $Q = 100$ e. The shaded areas correspond to the estimated error on Q of $\Delta Q = \pm 20$ e. Note that an increasing Q affects a stronger interaction potential inside the grating slits due to induced dipole interaction.

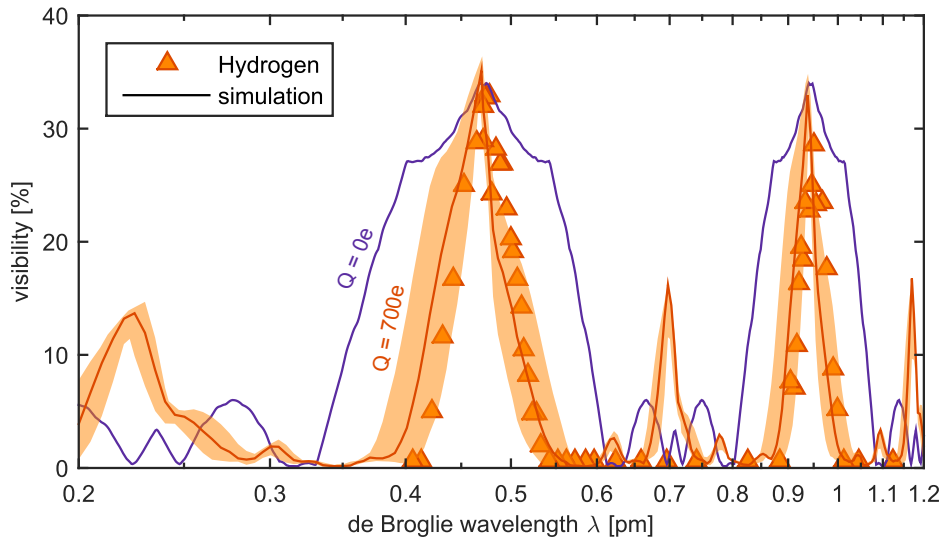


Figure 5.6.: Hydrogen: The width of the visibility peak around the first and second Talbot order decreases with increasing intra-grating interactions. The best agreement with the simulation is found for an implanted charge of $Q = 700$ e with an error interval (shaded area) between 300 e and 1400 e.

5. From Classical Xenon Fringes to Hydrogen Interferometry

Figure 5.5 pictures the data for de Broglie wavelengths below 0.1 pm and hence for argon, krypton, and xenon compared with the best fitting simulations. It can be clearly seen that the data points drop down at a sufficient smaller value for λ , as expected for the undisturbed case, i.e. $Q = 0 e$ (purple). The best agreement of the experimental data with the simulation is obtained for the depicted values of Q in the graph. While for argon a charge of 170 times the elementary charge e is found to reproduce the experimental observation, the result for krypton is $Q = 190 e$ and for xenon $Q = 100 e$. As a guide to the eye, the shaded area indicates what happens if Q is changed by $\Delta Q = \pm 20 e$, which also gives the error on the evaluated charges¹.

Significantly higher results for Q are obtained for the hydrogen beam in figure 5.6. Here, the figure of merit is the width of the visibility peak around the first and second Talbot orders. As can be seen, the simulation would agree with Q being of the order of 700 implanted charges, up to 7 times greater than what is found for the heavier nobles gases. The indicated error range includes implanted charges ranging from $Q = 300 e$ up to $Q = 1400 e$. A similar result is obtained from the helium data ($Q = 740 e$; same error range as for hydrogen). The similar outcome of hydrogen and helium can be explained due to the fact that for both species the width of the visibility peaks are comparable (see figure 5.3) and both atoms having a similar static polarisability (see table 3.4).

Taking into account intra-grating interactions due to implanted charges allows to describe satisfactorily the shape of the observed evolution of the visibility as a function of λ . It provides an explanation why the visibility peaks are much narrower and why the drop for heavy atoms is at smaller wavelengths than expected. The estimated charges Q are not consistent with respect to the different kind of particles. While for the heavy noble gases charges between 100 e and 200 e are enough to account for the different visibility evolution, hydrogen and helium require a charge of around 700 e. To explain this difference, it is to be emphasised that every measurement was performed on a different day, as changing gas in the source required time. Furthermore, while the measurement for argon, krypton, and xenon were completed within a week, hydrogen and helium were measured around two weeks later. Due to the calibration of the Wien filter and the pressure chamber, all three gratings were frequently exposed to the corresponding ion beam inbetween the individual measurements. All these factors could explain the different values for Q .

Yet another possible explanation for the difference in Q could be taking an equilibrium charge into account which is dependent on the beam parameters. It may be argued that while the experiment is running, a small fraction of the atoms hit the inner wall of the gratings, thereby building up a surface charge with a final strength Q . An argument for the difference in magnitude for the various gases, could be the particles' penetration depth. As previously discussed concerning figure 4.7, lighter particles, e.g. hydrogen, have a larger penetration depth compared to heavier particles, e.g. xenon, with the same kinetic energy, and hence could

¹The best fitting simulation is assumed to have the minimal sum of squared residuals with respect to the data and compared to the other simulations. The standard error of the residual is given by $\sigma = \sqrt{\frac{1}{N} \sum_N r_i^2}$ with N denotes the number of data points. The error on the charge considers all simulated dataset, whose sum of the squared residuals r are within the standard error of the simulation with the minimal squared residuals.

cause a larger implanted charge Q . The final equilibrium charge Q would hence depend on the particles' species and might degrade as soon as the beam is shut down.

Even if the question about the different number of charges cannot be answered fully, it provides a valuable estimate to discuss the feasibility of a proton interferometer in the next section.

5.4. Ion Interferometer with Material Gratings

In consideration of the success of utilising the Talbot-Lau interferometer to measure on hydrogen atoms, it is worth to discuss the feasibility of the same setup for ions or, in our case, protons. Various efforts exist to realise a matter wave experiment with ions [30, 31, 33]. The additional parameter charge, combined with the ions' mass (compared to electron interferometry) may give rise to a set of new experiments, such as measurements of the Aharonov-Bohm effect [22–24] or of deviations from Coulomb's inverse-square law [25]. Besides a biprism interferometer [30, 31], which requires a coherent particle source, the presently-discussed Talbot-Lau interferometer is a strong candidate to address this experimental field [25]. Of course, the main difference, the charges, gives rise to a number of experimental problems due to the ions' sensitivity to electric and magnetic fields. While external magnetic and electric fields can be sufficiently shielded (compare chapter 4.3), the fields inside the material gratings, and hence intra-grating interactions due to implanted charges, may be the critical point of this setup.

Using the Coulomb potential introduced in section 3.4 (equation 3.62) and the estimation of the implanted charges in section 5.3, we can calculate the visibility for the present Talbot-Lau interferometer when utilised with a proton beam. Figure 5.7 shows the calculated visibility profile for different implanted charges Q compared to the force-free case. As discussed above for the dipole interaction in case of hydrogen and the noble gases, the peak around the first Talbot order gets narrower with the increasing strength of the intra-grating interactions. This occurs because the intra-grating force due to Coulomb interactions exceeds the induced dipole interaction by more than six orders of magnitude. In order to observe constructive interference a well-defined de Broglie wavelength of protons to match the visibility peak is required. Table 5.2 lists critical deviation $\Delta\lambda$ for different Q for which the visibility drops significantly, such that detection of the fringe pattern is made impossible. For instance, an implanted charge of $Q = 100e$ requires to match the wavelength for the first Talbot order $\lambda_{1T} = 471.78$ fm with a precision better than $\Delta\lambda = 0.25$ fm. Transferred to the particles kinetic energy this means a precision better than $\Delta E = 4$ eV for $E_{1,1} = 3652$ eV. This is 1 ‰, and hence more than one order of magnitude smaller than the measured energy spread of 1.3 ‰ (equation (4.7)). Note that due to an energy spread of the beam of 1.3 ‰, the visibility peak is broadened but its maximum falls from the initial 100 ‰ to below 20 ‰, as the pattern is averaged with the patterns of the adjacent energies. Besides the de Broglie wavelength and hence the energy, a working proton interferometer with implanted charges would require a precise knowledge of the grating distance L and the period d , as these define the corresponding wavelength of the Talbot order (compare equation (2.6)). As further listed in table 5.2, for $Q = 100e$ and the described setup ($L = 14$ cm, $d = 257$ nm) this would mean an absolute alignment of the grat-

5. From Classical Xenon Fringes to Hydrogen Interferometry

ing distance better than $\Delta L = 74 \mu\text{m}$ and the grating pitch known to a level of $\Delta d = 68 \text{ pm}$. Note that implanting negative charges, e.g. $Q = -100e$, yields the same maximum visibility and width as the case with positive charges, although the skewness of the two cases differs.

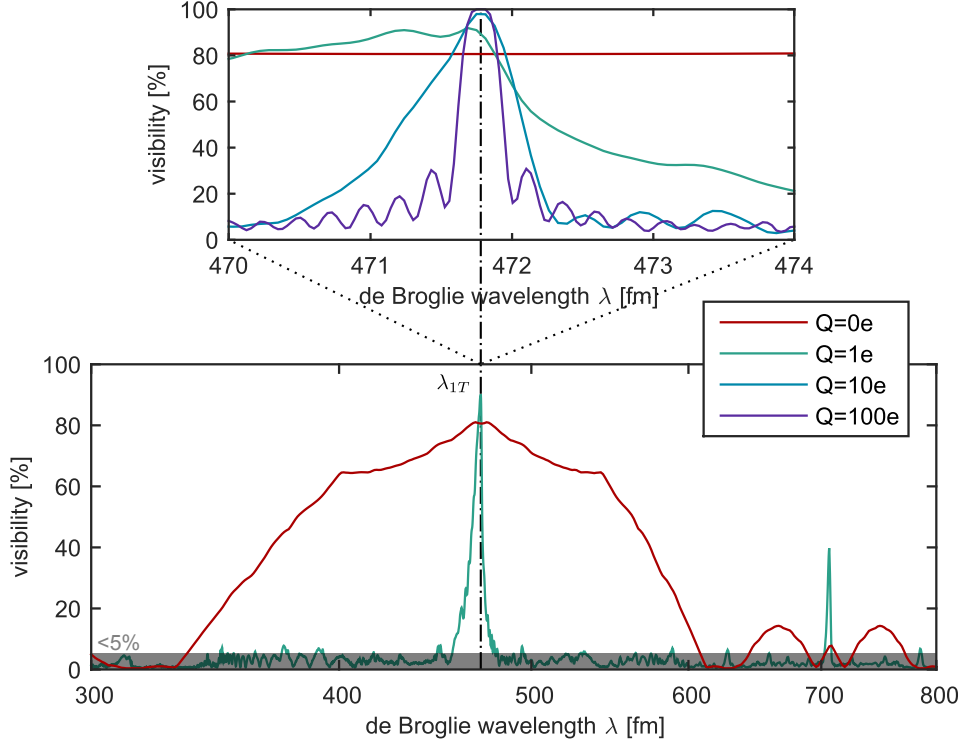


Figure 5.7.: The effect of an implanted charge Q for proton interference. The force inside the slits due to the Coulomb interaction exceeds the induced dipole interaction by more than six orders of magnitude. This results in a narrow peak around the wavelength corresponding to the first Talbot length. For an implanted charge of $Q = 100e$ the Talbot order has to be matched sufficiently better as $\Delta\lambda = 0.25 \text{ fm}$, which corresponds to the beam's energy precision of $\Delta E = 4 \text{ eV}$ at $E_{1,1} = 3652 \text{ eV}$.

Q [e]	$\Delta\lambda$ [fm]	ΔE [eV]	ΔL [μm]	Δd [pm]
1	14	220	4200	3800
10	1.2	19	356	327
100	0.25	4	74	68

Table 5.2.: Critical parameters to consider for a proton interferometer for different implanted charges Q . To detect the visibility maximum around the first Talbot order, the listed parameters have to be known with the stated precision. The values are estimated for idealised current setup with $d = 257 \times 10^{-9} \text{ nm}$ and $L = 14 \text{ cm}$, and hence $E_{1,1} = 3652 \text{ eV}$, which corresponds to a de Broglie wavelength of $\lambda_{1T} = 471.78 \text{ fm}$.

Following the above arguments, realisation of a proton interferometer with the current setup would need a control of the beam energy with precision of 1 eV. Furthermore, if we make a realistic assumption that the distance L is known only to the limit of $\Delta L = 100 \mu\text{m}$ and the grating period d to $\Delta d = 100 \text{pm}$, the position of the visibility peak is only known up $\Delta E = 11 \text{eV}$. This requires a fine scan around the expected position of $\pm\Delta E$ in order to find the peak. In principle this is feasible with the current setup, but only if the high voltage power supply is upgraded to a high precision voltage power supply with low ripple (i.e. $\lesssim 1 \%$) and if the beam energy spread is reduced for example implementing a double multi-pole Wien filter [124]. However in the current state of the art, alternative approaches which use laser gratings to diffract the ion beam [25, 125] are much more robust, as in those intra-grating interactions do not play any role.

5.5. Summary

In the beginning of the theory chapter (chapter 2) we illustrated with the help of figure 2.1 the overall behaviour of a Talbot-Lau interferometer. Now, the current chapter concludes with the same illustration in figure 5.8 but this time filled with the measurements realised in this work. We have proved the characteristic behaviour of such an interferometer for different de Broglie wavelengths over more than two orders of magnitude. We showed the sharp visibility peaks at wavelengths $\lambda_{nT} = nd^2/L$ corresponding up to the fourth Talbot order and the transition to the classical regime for $\lambda \ll d^2/L$. Furthermore, we have demonstrated the principle of a spectrometer based on such an interferometer, which provides an insight into the momentum composition of the beam, in case the beam production mechanism is not well understood. Moreover, deviations of the measured data points with respect to the theoretical curve provide a deeper understanding of intra-grating interactions due to implanted charges inside the material gratings. The presence of such charges and their estimated value set constraints on the feasibility of showing proton interference with the present setup. We have concluded this chapter by arguing that proton interferometry would be possible even with implanted charges, if one could achieve energy control precision better than 1% and small energy spread.

5. From Classical Xenon Fringes to Hydrogen Interferometry

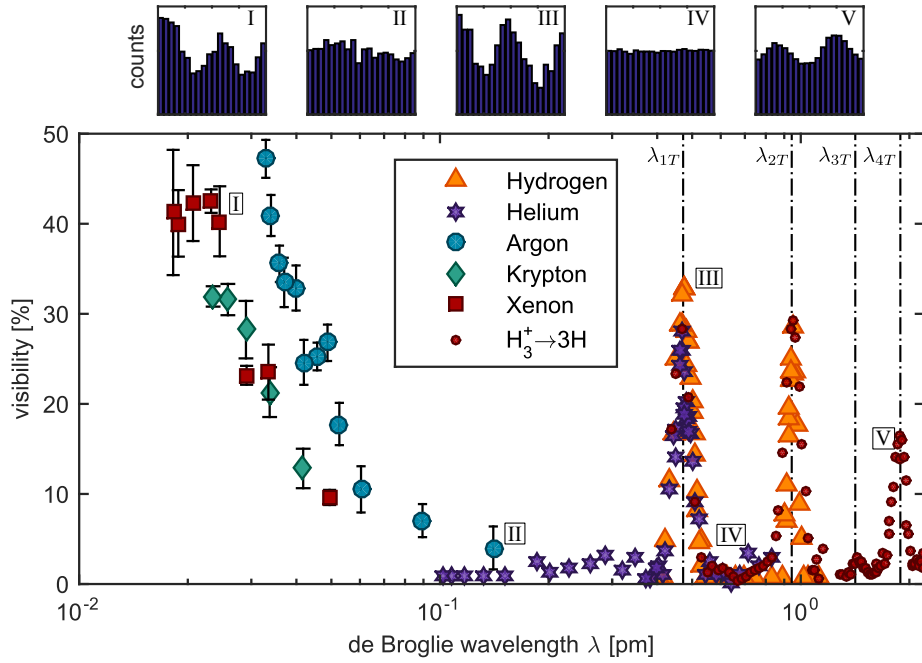


Figure 5.8.: Combined representation of all data, including the $H_3^+ \rightarrow 3H$ production directly at the source. It reveals the characteristic behaviour of the Talbot-Lau interferometer with rephasing – i.e. visibility maxima – at wavelengths λ_{nT} for which the grating distance L corresponds to multiples of the Talbot length $L_T = d^2/\lambda$. The transition to the classical regime is represented by the heavier atoms (xenon, krypton, argon) due to their smaller wavelengths, $\lambda < \lambda_{1T}$. Histograms on top show the raw data for the indicated positions from which the visibility is extracted.

6. Conclusion and Outlook

In the course of this work, a three-grating setup was theoretically studied and successfully experimentally realised with a wide range of atoms, namely hydrogen, helium, argon, krypton, and xenon to show the working principle of a Talbot-Lau interferometer and its transition to the classical regime, described in terms of a moiré deflectometer. The presented results enabled a discussion about the feasibility of an ion interferometer with the current setup.

We started with a full analytical description of the three-grating device as a Talbot-Lau interferometer. Without requiring a coherent source and using near-field interference effects, the interferometer was used to verify the wave nature of multiple particles. Furthermore, we showed that the same device can be classically described as a moiré deflectometer if the de Broglie wavelength of the impinging particles is sufficiently small.

We then proceeded to studying different effects influencing the visibility of the expected pattern. Particular attention was paid to the study of alignment requirements of the three-grating setup. We used a classical framework to derive quantitative formulae to set a limit on the required precision, considering the longitudinal position of the gratings, the grating pitch, and a tilt of the gratings around each axis. Discussing the influence of vibrations and external forces acting on the particles gave further constraints for a working interferometer. A detailed theoretical description of possible intra-grating interactions occurring inside the material gratings set a pathway to study the feasibility of a proton interferometer in the last chapter.

With the presented theoretical background and the constraints for a working setup, this work analysed in detail the experimental realisation of the three-grating device. Starting from the source and following the beam axis down to the detector, each component was explained and characterised separately. Here, we pointed out how a well-defined atom beam is produced with a known energy, a small divergence, and an energy spread around 1%. Furthermore, the Talbot-Lau interferometer was designed with high precision actuators and built in such a way that all alignment requirements could be complied with. The detection system and the data acquisition were shown to resolve single-particle impacts with a precision of $10\ \mu\text{m}$. The description of the experimental setup ended with a list of experiments, including fine scans over all actuators, to further characterise the apparatus. Thanks to these tests, we found out that, in addition to the expected particles, the source also produced photons consistent with the spectral lines of the gas inside the plasma source. Moreover, with a rotational scan of the first and second grating we were able to measure a difference in the periodicities of the three

6. Conclusion and Outlook

gratings in the order of 140 pm.

In the final stage, the interferometer was exposed to different particles with energies up to 20 keV. The selected species were hydrogen, helium, argon, krypton, and xenon. Hence we had access to a wide range of de Broglie wavelengths between 0.02 pm and 2.2 pm. The reported data for all particles verified the full characteristic behaviour of the Talbot-Lau interferometer and hence the particles' description in terms of the wave-particle duality. Furthermore, we could show that for the heavier particles and thus smaller wavelengths, the data also matched a classical description. In this context, we presented the idea of using the Talbot-Lau interferometer as a spectrometer to understand the composition of a particle beam whose energy is known only up to a proportionality factor. The deviation of the calculated signal from the obtained data gave an insight into the intra-grating interactions which were modelled by simulating implanted charges inside the gratings. Charges of more than a hundred times the elementary charge had to be assumed in order to understand the discrepancy between theory and experiment. This gave rise to the question about the feasibility of an ion interferometer. This is because assuming deposited charge of 100 e inside the gratings sets major constraint on the experimental realisation of a proton interferometer. We concluded that the main parameters of the experiment – the particle's energy, the distance between the gratings, and the grating period – have to match each other on a per mille scale to achieve an interference signal. This also includes the requirement that the energy spread of the beam be on the same per mille scale.

Thus, we concluded that in order to achieve proton interferometry, it is crucial either to improve the source or to avoid implantation of any charges inside the gratings. On the side of the proton source, a decrease in the energy spread, down to the demanded per mille level is required, while also the absolute precision of the beam's energy has to be known at this scale. This demands an improvement of the ion-beam optics but also a higher precision on the applied acceleration voltage. The gratings, on the other hand, could be improved with an additional gold-coating to shield the effect of implanted charges. Summarising, we argue that the above-mentioned improvements on the source and gratings make a realisation of a Talbot-Lau interferometer for protons more feasible.

Bibliography

- [1] Louis de Broglie. The wave nature of the electron. *Nobel Lecture*, December 12 1929.
- [2] Louis-Victor de Broglie. *On the Theory of Quanta*. PhD thesis, Paris, 1925.
- [3] Henning Sievers. Louis de broglie und die quantenmechanik. 1998.
- [4] Alistair C. Crombie. *Robert Grosseteste and the origins of experimental science 1100-1700*. Clarendon Pr., Oxford, 1953.
- [5] Isaac Newton. A new theory about light and colors. *American Journal of Physics*, 61(2):108–112, 1993.
- [6] Christiaan Huygens. *Traite de la lumiere*. chez Pierre Vander Aa marchand libraire, 1690.
- [7] Paul Ehrenfest. Welche Züge der Lichtquantenhypothese spielen in der Theorie der Wärmestrahlung eine wesentliche Rolle? *Annalen der Physik*, 341(11):91–118, 1911.
- [8] Albert Einstein and Leopold Infeld. *Physik als Abenteuer der Erkenntnis*. Sijthoff, Leiden, 2. edition, 1949.
- [9] C.J. Davisson. The diffraction of electrons by a crystal of nickel. *Bell System Technical Journal*, 7(1):90–105, Jan 1928.
- [10] I. Estermann and O. Stern. Beugung von molekularstrahlen. *Zeitschrift für Physik*, 61(1-2):95–125, 1930.
- [11] Helmut Rauch and Samuel A. Werner. *Neutron interferometry*. Oxford Univ. Pr., Oxford, 2. ed. edition, 2015.
- [12] Dana P. Mitchell and Philip N. Powers. Bragg reflection of slow neutrons. *Phys. Rev.*, 50:486–487, Sep 1936.
- [13] Markus Arndt, Olaf Nairz, Julian Vos-Andreae, Claudia Keller, Gerbrand Van der Zouw, and Anton Zeilinger. Wave-particle duality of C₆₀ molecules. *nature*, 401(6754):680–682, 1999.

BIBLIOGRAPHY

- [14] Björn Brezger, Lucia Hackermüller, Stefan Uttenthaler, Julia Petschinka, Markus Arndt, and Anton Zeilinger. Matter-wave interferometer for large molecules. *Phys. Rev. Lett.*, 88:100404, Feb 2002.
- [15] Lucia Hackermüller, Stefan Uttenthaler, Klaus Hornberger, Elisabeth Reiger, Björn Brezger, Anton Zeilinger, and Markus Arndt. Wave nature of biomolecules and fluorofullerenes. *Phys. Rev. Lett.*, 91:090408, Aug 2003.
- [16] Stefan Gerlich, Sandra Eibenberger, Mathias Tomandl, Stefan Nimmrichter, Klaus Hornberger, Paul J Fagan, Jens Tüxen, Marcel Mayor, and Markus Arndt. Quantum interference of large organic molecules. *Nature communications*, 2:263, 2011.
- [17] Sandra Eibenberger, Stefan Gerlich, Markus Arndt, Marcel Mayor, and Jens Tüxen. Matter-wave interference of particles selected from a molecular library with masses exceeding 10000 amu. *Physical Chemistry Chemical Physics*, 15(35):14696–14700, 2013.
- [18] Yaakov Y Fein, Philipp Geyer, Patrick Zwick, Filip Kialka, Sebastian Pedalino, Marcel Mayor, Stefan Gerlich, and Markus Arndt. Quantum superposition of molecules beyond 25 kda. *Nature Physics*, pages 1–4, 2019.
- [19] S. Sala, A. Ariga, A. Ereditato, R. Ferragut, M. Giammarchi, M. Leone, C. Pistillo, and P. Scamporrino. First demonstration of antimatter wave interferometry. *Science Advances*, 5(5), 2019.
- [20] Christopher R. Ekstrom, Jörg Schmiedmayer, Michael S. Chapman, Troy D. Hammond, and David E. Pritchard. Measurement of the electric polarizability of sodium with an atom interferometer. *Phys. Rev. A*, 51:3883–3888, May 1995.
- [21] T. L. Gustavson, P. Bouyer, and M. A. Kasevich. Precision rotation measurements with an atom interferometer gyroscope. *Phys. Rev. Lett.*, 78:2046–2049, Mar 1997.
- [22] Y. Aharonov and D. Bohm. Significance of electromagnetic potentials in the quantum theory. *Physical Review*, 115(3):485–491, 1959. cited By 4386.
- [23] M.P. Silverman. Optical manifestations of the aharonov-bohm effect by ion interferometry. *Physics Letters A*, 182(4):323 – 329, 1993.
- [24] G. Schütz, A. Rembold, A. Pooch, H. Prochel, and A. Stibor. Effective beam separation schemes for the measurement of the electric aharonov-bohm effect in an ion interferometer. *Ultramicroscopy*, 158:65 – 73, 2015.
- [25] B. Neyenhuis, D. Christensen, and D. S. Durfee. Testing nonclassical theories of electromagnetism with ion interferometry. *Phys. Rev. Lett.*, 99:200401, Nov 2007.
- [26] Yaakov Fein, Philipp Geyer, Patrick Zwick, Filip Kialka, Sebastian Pedalino, Marcel Mayor, Stefan Gerlich, and Markus Arndt. Quantum superposition of molecules beyond 25 kda. *Nature Physics*, pages 1–4, 09 2019.

- [27] Joseph P. Cotter, Christian Brand, Christian Knobloch, Yigal Lilach, Ori Cheshnovsky, and Markus Arndt. In search of multipath interference using large molecules. *Science Advances*, 3(8), 2017.
- [28] Claus Jönsson. Elektroneninterferenzen an mehreren künstlich hergestellten Feinspalten. *Zeitschrift für Physik*, 161(4):454–474, 1961.
- [29] G Gronniger, B Barwick, and H Batelaan. A three-grating electron interferometer. *New Journal of Physics*, 8(10):224, 2006.
- [30] U. Maier. *Ein Biprisma Interferometer für Ionen*. PhD thesis, Eberhard-Karls-Universität Tübingen, 1997.
- [31] G. Schütz, A. Rembold, A. Pooch, S. Meier, P. Schneeweiss, A. Rauschenbeutel, A. Günther, W.T. Chang, I.S. Hwang, and A. Stibor. Biprism electron interferometry with a single atom tip source. *Ultramicroscopy*, 141:9 – 15, 2014.
- [32] A Rembold, G Schütz, R Röpke, W T Chang, I S Hwang, A Günther, and A Stibor. Vibrational dephasing in matter-wave interferometers. *New Journal of Physics*, 19(3):033009, mar 2017.
- [33] Philippe H. M. Bräunig, James Storey, and Markus K. Oberthaler. Atlix: Antimatter talbot-lau interferometry experiment. *Internal Proposal of the AEgIS collaboration*, 2014.
- [34] Philippe H. M. Bräunig. *Atom Optical Tools for Antimatter Experiments*. PhD thesis, Ruperto-Carola University of Heidelberg, December 2014.
- [35] John F. Clauser and Shifang Li. Talbot-von lau atom interferometry with cold slow potassium. *Phys. Rev. A*, 49:R2213–R2216, Apr 1994.
- [36] Roger Bach, Glen Gronniger, and Herman Batelaan. An electron talbot-lau interferometer and magnetic field sensing. *Applied Physics Letters*, 103(25), 2013.
- [37] William B. Case, Mathias Tomandl, Sarayut Deachapunya, and Markus Arndt. Realization of optical carpets in the talbot and talbot-lau configurations. *Opt. Express*, 17(23):20966–20974, Nov 2009.
- [38] Markus K. Oberthaler, Stefan Bernet, Ernst M. Rasel, Jörg Schmiedmayer, and Anton Zeilinger. Inertial sensing with classical atomic beams. *Physical review A*, 75(4):3165–3176, 1996.
- [39] Tobias M. Wintermantel. Measurement of gravity using a moiré deflectometer for metastable argon atoms. Bachelor thesis, 2013.
- [40] H.F. Talbot. Lxxvi. facts relating to optical science. no. iv. *Philosophical Magazine Series 3*, 9(56):401–407, 1836.

BIBLIOGRAPHY

- [41] Lord Rayleigh. Xxv. on copying diffraction-gratings, and on some phenomena connected therewith. *Philosophical Magazine Series 5*, 11(67):196–205, 1881.
- [42] M. V. Berry and S. Klein. Integer, fractional and fractal talbot effects. *Journal of Modern Optics*, 43(10):2139–2164, 1996.
- [43] E. Lau. Beugungserscheinungen an Doppellrastern. *Annalen der Physik*, 437(7-8):417–423, 1948.
- [44] S Aghion, O Ahlén, Claude Amsler, Akitaka Ariga, T Ariga, A Belov, Karl Berggren, Germano Bonomi, P Bräunig, J Bremer, R.s Brusa, L Cabaret, Carlo Canali, Ruggero Caravita, Fabrizio Castelli, Giovanni Cerchiari, Simone Cialdi, Daniel Comparat, G Consolati, and Johann Zmeskal. A moiré deflectometer for antimatter. *Nature communications*, 5:4538, 07 2014.
- [45] Simon R. Müller. Moiré deflectometer for charged particles. Master’s thesis, University of Heidelberg, 2015.
- [46] Pierre Lansonneur. *Moiré Deflectometry with a Low-Energy Ion Beam for the AEGIS Experiment*. PhD thesis, l’Université Claude Bernard Lyon 1, January 2018.
- [47] Andrea Demetrio. *Feasibility of a gravity measurement on antimatter using a Talbot-Lau interferometer*. Heidelberg, 2018.
- [48] Fabian Bergermann. Characterization of the moiré deflectometer for the aegis-experiment. *Diploma thesis, Kirchhoff Institute for Physics*, 2012.
- [49] Joseph W. Goodman. *Introduction to Fourier optics*. McGraw-Hill, 1996.
- [50] Kyoji Matsushima, Hagen Schimmel, and Frank Wyrowski. Fast calculation method for optical diffraction on tilted planes by use of the angular spectrum of plane waves. *J. Opt. Soc. Am. A*, 20(9):1755–1762, Sep 2003.
- [51] Lingfeng Yu and Myung K. Kim. Wavelength-scanning digital interference holography for tomographic three-dimensional imaging by use of the angular spectrum method. *Opt. Lett.*, 30(16):2092–2094, Aug 2005.
- [52] Christopher J Vecchio and Peter A Lewin. Finite amplitude acoustic propagation modeling using the extended angular spectrum method. *The Journal of the Acoustical Society of America*, 95(5):2399–2408, 1994.
- [53] Andrea Demetrio, Simon R. Müller, Pierre Lansonneur, and Markus K. Oberthaler. Progress toward a large-scale ion talbot-lau interferometer. *Phys. Rev. A*, 96:063604, Dec 2017.
- [54] Greg A. Voth, Arthur La Porta, Alice M. Crawford, Eberhard Bodenschatz, Curt Ward, and Jim Alexander. A silicon strip detector system for high resolution particle tracking in turbulence. *Review of Scientific Instruments*, 72(12):4348–4353, 2001.

- [55] A. S. Tremsin, J. V. Vallerga, J. B. McPhate, O. H. W. Siegmund, and R. Raffanti. High resolution photon counting with mcp-timepix quad parallel readout operating at >1khz frame rates. *IEEE Transactions on Nuclear Science*, 60(2):578–585, April 2013.
- [56] J. Jahns, A.W. Lohmann, and J. Ojeda-Castañeda. Talbot and lau effects, a para-geometrical approach. *Optica Acta: International Journal of Optics*, 31(3):313–324, 1984.
- [57] Ch. Siegel, F. Loewenthal, and J. E. Balmer. A wavefront sensor based on the fractional Talbot effect. *Optics Communications*, 194:265 – 275, 2001.
- [58] Stefan Nimmrichter and Klaus Hornberger. Theory of near-field matter-wave interference beyond the eikonal approximation. *Phys. Rev. A*, 78:023612, Aug 2008.
- [59] Klaus Hornberger, John E. Sipe, and Markus Arndt. Theory of decoherence in a matter wave talbot-lau interferometer. *Phys. Rev. A*, 70:053608, Nov 2004.
- [60] E. Wigner. On the quantum correction for thermodynamic equilibrium. *Physical Review*, 40(5):749–759, 1932.
- [61] Klaus Hornberger, Stefan Gerlich, Hendrik Ulbricht, Lucia Hackermüller, Stefan Nimmrichter, Ilya V Goldt, Olga Boltalina, and Markus Arndt. Theory and experimental verification of kapitza–dirac–talbot–lau interferometry. *New Journal of Physics*, 11(4):043032, apr 2009.
- [62] Stefan Gerlich. *Interferometry and Metrology with Macromolecules*. PhD thesis, University of Vienna, September 2011.
- [63] *User Manual - Premium Line, Positioners & Scanners*. attocube systems AG, 2015.
- [64] Alexander Stibor. *Optical Methods for Macromolecule Interferometry*. PhD thesis, University of Vienna, November 2005.
- [65] A. Stibor, K. Hornberger, L. Hackermueller, A. Zeilinger, and M. Arndt. Talbot-lau interferometry with fullerenes: Sensitivity to inertial forces and vibrational dephasing. 2004.
- [66] Paul R. Berman, editor. *Atom interferometry*. Academic Press, 1997.
- [67] P. Lansonneur, P. Bräunig, A. Demetrio, S.R. Müller, P. Nedelec, and M.K. Oberthaler. Probing electric and magnetic fields with a moiré deflectometer. *Nuclear Instruments and Methods in Physics Research Section A: Accelerators, Spectrometers, Detectors and Associated Equipment*, 862:49 – 53, 2017.
- [68] G. Drobychev et al. (AEgIS collaboration). Proposal for the aegis experiment at the cern antiproton decelerator. *SPSC-P-334; CERN-SPSC-2007-017*, 2007.

BIBLIOGRAPHY

- [69] S. Aghion et al. (AEgIS collaboration). Prospects for measuring the gravitational free-fall of antihydrogen with emulsion detectors. *Journal of Instrumentation*, 8:P08013, 2013.
- [70] Charles J. Joachain. *Quantum collision theory*. North-Holland, Amsterdam, 1975.
- [71] R. Brühl, P. Fouquet, R. E. Grisenti, J. P. Toennies, G. C. Hegerfeldt, T. Köhler, M. Stoll, and C. Walter. The van der waals potential between metastable atoms and solid surfaces: Novel diffraction experiments vs. theory. *Europhysics Letters (EPL)*, 59(3):357–363, Aug 2002.
- [72] R. E. Grisenti, W. Schöllkopf, J. P. Toennies, G. C. Hegerfeldt, and T. Köhler. Determination of atom-surface van der waals potentials from transmission-grating diffraction intensities. *Phys. Rev. Lett.*, 83:1755–1758, Aug 1999.
- [73] James F. Ziegler. Srim-2003. *Nuclear Instruments and Methods in Physics Research Section B: Beam Interactions with Materials and Atoms*, 219-220:1027 – 1036, 2004. Proceedings of the Sixteenth International Conference on Ion Beam Analysis.
- [74] I.E. Dzyaloshinskii, E.M. Lifshitz, and L.P. Pitaevskii. The general theory of van der waals forces. *Advances in Physics*, 10(38):165–209, 1961.
- [75] Gianfranco Vidali, G. Ihm, Hye-Young Kim, and Milton W. Cole. Potentials of physical adsorption. *Surface Science Reports*, 12(4):135 – 181, 1991.
- [76] E. Zaremba and W. Kohn. Van der waals interaction between an atom and a solid surface. *Phys. Rev. B*, 13:2270–2285, Mar 1976.
- [77] A.D. McLachlan. Van der waals forces between an atom and a surface. *Molecular Physics*, 7(4):381–388, 1964.
- [78] H. Hoinkes. The physical interaction potential of gas atoms with single-crystal surfaces, determined from gas-surface diffraction experiments. *Rev. Mod. Phys.*, 52:933–970, Oct 1980.
- [79] M. Muramatsu and A. Kitagawa. A review of ion sources for medical accelerators. *Review of Scientific Instruments*, 83(2):02B909, 2012.
- [80] K. Choi, S. Ghosh, J. Lim, and C.M. Lee. Removal efficiency of organic contaminants on Si wafer by dry cleaning using UV/O₃ and ECR plasma. *Applied Surface Science*, 206(1):355 – 364, 2003.
- [81] Bernhard Wolf, editor. *Handbook of ion sources*. CRC Press, Boca Raton, 1995.
- [82] Terence Taylor and Jozef F. Mouris. An advanced high-current low-emittance dc microwave proton source. *Nuclear Instruments and Methods in Physics Research Section A: Accelerators, Spectrometers, Detectors and Associated Equipment*, 336(1):1 – 5, 1993.

- [83] David Spence and Keith R. Lykke. Generation of high purity cw proton beams from microwave driven sources. In *Particle Accelerator Conference, 1995., Proceedings of the 1995*, volume 2, pages 1019–1021 vol.2, May 1995.
- [84] R. Geller. ECRIS: the electron cyclotron resonance ion sources - (status). *Zeitschrift für Physik D Atoms, Molecules and Clusters*, 21(1):S117–S121, 1991.
- [85] T. Taylor. High-current dc microwave ion sources. *Review of Scientific Instruments*, 63(4):2507–2512, 1992.
- [86] P. Sortais, T. Lamy, J. Médard, J. Angot, L. Latrasse, and T. Thuillier. Ultracompact/ultralow power electron cyclotron resonance ion source for multipurpose applications. *Review of Scientific Instruments*, 81(2):02B314, 2010.
- [87] High performance magnets. www.first4magnets.com. Accessed: 2019-10-10.
- [88] James S. Allen. The emission of secondary electrons from metals bombarded with protons. *Phys. Rev.*, 55:336–339, Feb 1939.
- [89] L N Large and W S Whitlock. Secondary electron emission from clean metal surfaces bombarded by fast hydrogen ions. *Proceedings of the Physical Society*, 79(1):148, 1962.
- [90] J. A. Ray and C. F. Barnett. Secondary electron emission of metals bombarded with 120ev to 5kev protons. *Journal of Applied Physics*, 42(8):3260–3261, 1971.
- [91] Hans Pauly. *Atom, molecule, and cluster beams II*. Springer series on atomic, optical, and plasma physics. Springer, Berlin; Heidelberg; New York, 2000.
- [92] Harrie Stewart Wilson Massey, EHS Burhop, and HB Gilbody. *Recombination and fast collisions of heavy particles*. Clarendon Pr., Oxford, 2. ed. edition, 1974.
- [93] Ahmad Fauzi Ismail, Kailash Chandra Khulbe, and Takeshi Matsuura. *Gas Separation Membranes*. Springer eBook Collection : Chemistry and Materials Science. Springer, Cham, 2015.
- [94] M. E. Rudd, R. D. DuBois, L. H. Toburen, C. A. Ratcliffe, and T. V. Goffe. Cross sections for ionization of gases by 5-4000-kev protons and for electron capture by 5-150-kev protons. *Phys. Rev. A*, 28:3244–3257, Dec 1983.
- [95] M. E. Rudd, T. V. Goffe, A. Itoh, and R. D. DuBois. Cross sections for ionization of gases by 10–2000-keV He^+ ions and for electron capture and loss by 5–350-keV He^+ ions. *Phys. Rev. A*, 32:829–835, Aug 1985.
- [96] C. F. Barnett and P. M. Stier. Charge exchange cross sections for helium ions in gases. *Phys. Rev.*, 109:385–390, Jan 1958.
- [97] TA Savas, Satyen N. Shah, Mark Schattenburg, J M. Carter, and Henry I. Smith. Achromatic interferometric lithography for 100-nm-period gratings and grids. *Journal of Vacuum Science & Technology B: Microelectronics and Nanometer Structures*, 13:2732–2735, 12 1995.

BIBLIOGRAPHY

- [98] T. A. Savas, M. L. Schattenburg, J. M. Carter, and H. I. Smith. Large-area achromatic interferometric lithography for 100 nm period gratings and grids. *Journal of Vacuum Science Technology B: Microelectronics and Nanometer Structures*, 14:4167–4170, November 1996.
- [99] attocube systems ag. www.attocube.com. Accessed: 2019-10-10.
- [100] David Jiles. *Introduction to Magnetism and Magnetic Materials*. Chapman & Hall/CRC, second edition, 1998.
- [101] Magnetic shields electromagnetic engineering. www.magneticshields.co.uk. Accessed: 2019-08-10.
- [102] J. M. Lockhart, F. C. Witteborn, and W. M. Fairbank. Evidence for a temperature-dependent surface shielding effect in Cu. *Phys. Rev. Lett.*, 38:1220–1223, May 1977.
- [103] G.W. Fraser. The soft x-ray quantum detection efficiency of microchannel plates. *Nuclear Instruments and Methods in Physics Research*, 195(3):523 – 538, 1982.
- [104] G.W. Fraser. X- and γ -ray imaging using microchannel plates. *Nuclear Instruments and Methods in Physics Research*, 221(1):115 – 130, 1984. Proceedings of the International Workshop on X- and gamma-Ray Imaging Techniques.
- [105] G.W. Fraser. The ion detection efficiency of microchannel plates (mcps). *International Journal of Mass Spectrometry*, 215(1-3):13 – 30, 2002. Detectors and the Measurement of Mass Spectra.
- [106] Joseph Ladislav Wiza. Microchannel plate detectors. *Nuclear Instruments and Methods*, 162(1-3):587 – 601, 1979.
- [107] J Oberheide, P Wilhelms, and M Zimmer. New results on the absolute ion detection efficiencies of a microchannel plate. *Measurement Science and Technology*, 8(4):351–354, apr 1997.
- [108] B.L Peko and T.M Stephen. Absolute detection efficiencies of low energy H, H-, H+, H2+ and H3+ incident on a multichannel plate detector. *Nuclear Instruments and Methods in Physics Research Section B: Beam Interactions with Materials and Atoms*, 171(4):597 – 604, 2000.
- [109] Gids-gmbh german image detector systems. <https://www.gids-gmbh.com>. Accessed: 2019-08-10.
- [110] Allied vision technologies gmbh. www.alliedvision.com. Accessed: 2019-08-10.
- [111] Frederik Gröll, Manfred Kirchgessner, Rainer Kaufmann, Michael Hausmann, and U Keschull. Accelerating image analysis for localization microscopy with fpgas. pages 1–5, 09 2011.

- [112] L. Lindegren. Photoelectric astrometry - a comparison of methods for precise image location. In *IAU Colloq. 48: Modern Astrometry*, page 197, Jan 1978.
- [113] M. Gai, D. Carollo, M. Delbò, M. G. Lattanzi, G. Massone, F. Bertinetto, G. Mana, and S. Cesare. Location accuracy limitations for ccd cameras. *Astronomy and Astrophysics*, 367:362–370, Feb 2001.
- [114] Kantilal V. Mardia and Peter E. Jupp. *Directional statistics*. Wiley series in probability and statistics. Wiley, Chichester [u.a.], 2000. Includes bibliographical references and index.
- [115] Christophe Ley and Thomas Verdebout. *Modern directional statistics*. Chapman & Hall/CRC interdisciplinary statistics series. CRC Press, Taylor & Francis Group, Boca Raton; London; New York, 2017.
- [116] R. J. Beran. Asymptotic theory of a class of tests for uniformity of a circular distribution. *Ann. Math. Statist.*, 40(4):1196–1206, 08 1969.
- [117] Lord Rayleigh O.M. F.R.S. Xxxi. on the problem of random vibrations, and of random flights in one, two, or three dimensions. *The London, Edinburgh, and Dublin Philosophical Magazine and Journal of Science*, 37(220):321–347, 1919.
- [118] R Buccheri, K Bennett, G F. Bignami, J B. G. M. Bloemen, V Boriakoff, P Caraveo, Wim Hermsen, Gottfried Kanbach, R N. Manchester, Jean-Louis Masnou, H A. Mayer-Hasselwander, M.E. Ozel, J A. Paul, B Sacco, L Scarsi, and A W. Strong. Search for pulsed gamma-ray emission from radio pulsars in the cos-b data. *Astronomy and Astrophysics*, 128:245–251, 10 1983.
- [119] M. P. Muno, F. K. Baganoff, M. W. Bautz, W. N. Brandt, G. P. Garmire, and G. R. Ricker. X-ray sources with periodic variability in a DeepChandraImage of the galactic center. *The Astrophysical Journal*, 599(1):465–474, dec 2003.
- [120] Denis Leahy, Ronald Elsner, and M C. Weisskopf. On searches for periodic pulsed emission - the rayleigh test compared to epoch folding. *The Astrophysical Journal*, 272, 10 1983.
- [121] Wolfgang Wiltschko and Roswitha Wiltschko. Magnetic compass of european robins. *Science*, 176(4030):62–64, 1972.
- [122] S Engels, NL Schneider, N Lefeldt, CM Hein, M Zapka, A Michalik, D Elbers, A Kittel, PJ Hore, and H Mouritsen. Anthropogenic electromagnetic noise disrupts magnetic compass orientation in a migratory bird. *Nature*, 509(7500):353–356, 2014.
- [123] Lennart Minnhagen. Spectrum and the energy levels of neutral argon, ar i. *J. Opt. Soc. Am.*, 63(10):1185–1198, Oct 1973.
- [124] G Martinez and K Tsuno. Design of wien filters with high resolution. *Ultramicroscopy*, 100(1):105 – 114, 2004.

BIBLIOGRAPHY

- [125] DL Freimund, K Aflatooni, and H Batelaan. Observation of the kapitza-dirac effect. *Nature*, 413(6852):142–143, September 2001.
- [126] C. Patrignani et al (Particle Data Group). Review of particle physics. *Chinese Physics C*, 40(10):100001, oct 2016.

A. Constants

Fundamental physical constants and related quantities used in this work are adapted from [126] and listed in the following table.

constant	symbol	value
electron mass	m_e	9.1094×10^{-31} kg
proton mass	m_p	1.6726×10^{-19} kg
elementary charge	e	1.6022×10^{-19} C
Planck constants	\hbar	1.0546×10^{-34} J s
	h	$\hbar \cdot 2\pi$
speed of light	c	$299\,792\,458$ m s $^{-1}$
Boltzmann constant	k_B	1.3087×10^{-23} J K $^{-1}$
vacuum permittivity	ϵ_0	8.854×10^{-12} F m $^{-1}$

B. Publications

This appendix contains all publications to which the author of this work has made a contribution. The publications are divided into two groups. Firstly the publications are listed for which a significant and personal contribution was made. This includes all publications stemming from the work done in the Heidelberg AEGIS research group.

As a member of the AEGIS collaboration located at CERN, with the scientific goal to achieve a direct measurement of the Earth's gravitational acceleration on antihydrogen, an indirect participation has led to a set of further publications. The personal contribution to these publications was in form of taking part in experimental shifts during measurement runs and in discussions at the collaboration meetings.

Heidelberg

S. R. Müller, P. Nedelec and M. K. Oberthaler.

"From Classical Xenon Fringes to Hydrogen Interferometry".

Manuscript in Preparation for publishing in New Journal of Physics.

A. Demetrio, S. R. Müller, P. Lansonneur, and M. K. Oberthaler.

"Progress toward a large-scale ion Talbot-Lau interferometer".

Phys. Rev. A 96 (2017), p. 063604.

DOI: 10.1103/PhysRevA.96.063604.

P. Lansonneur, P. Bräunig, A. Demetrio, S. R. Müller, P. Nedelec, and M. K. Oberthaler

"Probing electric and magnetic fields with a moiré deflectometer".

Nucl. Instr. Meth. Phys. Res. A 862 (2017), pp. 49-53.

DOI: 10.1016/j.nima.2017.04.041

AEGIS Collaboration

Antonello, M., et al. (AEGIS Collaboration).

"Efficient 2^3S positronium production by stimulated decay from the 3^3P level."
arXiv, 1904.09004 (2019).

Amsler, C., et al. (AEGIS Collaboration).

"A $\sim 100 \mu\text{m}$ -resolution position-sensitive detector for slow positronium."
Nucl. Instrum. Methods Phys. Res., 457 (2019): 44-48.

Amsler, C., et al. (AEGIS Collaboration).

"Velocity-selected production of 2^3S metastable positronium."
Phys. Rev. A, 99 (2019): 033405.

Aghion, S., et al. (AEGIS Collaboration).

"Producing long-lived 2^3S positronium via 3^3P laser excitation in magnetic and electric field."
Phys. Rev. A., 98 (2018): 013402.

Aghion, S., et al. (AEGIS Collaboration).

"Compression of a mixed antiproton and electron non-neutral plasma to high densities."
Eur. Phys. J. D., 72.04 (2018).

Doser, M., et al. (AEGIS Collaboration).

"AEGIS at ELENA: outlook for physics with a pulsed cold antihydrogen beam."
Phil. Trans. R. Soc. A, 376.2116 (2018): 20170274.

Evans, C., et al. (AEGIS Collaboration).

"Towards the first measurement of matter-antimatter gravitational interaction".
INCNFP, 182 (2018): 02040.

Guatieri, F., et al. (AEGIS Collaboration).

"AEGIS latest results".
EPJ Web of Conferences, 181 (2018), 01037.

Aghion, S., et al. (AEGIS Collaboration).

"Antiproton tagging and vertex fitting in a Timepix3 detector."
J. Inst., 13.06 (2017): P06004.

Aghion, S., et al. (AEGIS Collaboration).

"Characterization of a transmission positron/positronium converter for antihydrogen production."
Nucl. Instr. Meth. Phys. Res., B 407 (2017): 55-66.

Aghion, S., et al. (AEgIS Collaboration).
"Measurement of antiproton annihilation on Cu, Ag and Au with emulsion films".
J. Inst., 12.04 (2017): P04021.

Consolati, G., et al. (AEgIS Collaboration).
"Positronium for Antihydrogen Production in the AEGIS Experiment".
Acta Phys. Pol. A, 132.5 (2017).

Prelz, F., et al. (AEgIS Collaboration).
"The DAQ system for the AEGIS experiment".
J. Phys.: Conference Series, 898, 3 (2017).

Evans, C., et al. (AEgIS Collaboration).
"Advances in Ps manipulation and laser studies in the AEGIS experiment".
Acta Phys. Pol. B, 48.10 (2017).

Lansonneur, P., et al. (AEgIS Collaboration).
"AEGIS experiment: status & outlook".
Recontres de Moriond on Gravitation, (2017), pp.87-92.

C. Note of Gratitude

At this point I would like to thank very much those without whom this work would not have been possible. I am deeply grateful to

- Prof. Dr. M. Oberthaler for supervising my work, and for being an enthusiastic and inspiring guide in the field of physics.
- Prof. Dr. T. Gasenzer for taking the time to review my work.
- Prof. Dr. M. Arndt for the discussions about interferometry and for offering his nanometric gratings to our group at Heidelberg.
- Prof. Dr. P. Nedelec for supplying the proton source for our work.
- my colleagues and friends Andrea Demetrio and Pierre Lansonneur who have shared their time with me in the laboratory in search for interference fringes.
- Alex and Zhongyi who have always lent me a helping hand in the lab if needed.
- the research group of Prof. Dr. R. Schröder, especially Anne Kast and Lisa Veith, for the help in coating the gratings and taking images with the SEM.
- James. F. Ziegler for the deeper insight into *SRIM*.
- Philippe, Fabian, Gerard, and Patrick for their help in the lab.
- the AEGIS Collaboration for the inspiring time together at CERN.
- D. Hufnagel and C. Jäger for their amazing job as team assistants.
- the whole KIP workshop and their incredible work in machining the interferometer. Special thanks to W. Lamade, M. Weißer, and S. Spiegel for the fruitful discussion about the design of the experiment and the introduction to the workshop.
- A. Dobler and J. Schölles for their support in electronics.
- all the members of the matterwave group for the support over the last years and the fun time together.

C. Note of Gratitude

- Martin and Christian for the deep and interesting discussions about various fields beyond physics.
- my parents, and siblings Johannes, Theresia together with her husband Steffen, Daniel, Fabian, and Niklas for being a part of my life.